INFORMATION TO USERS

This manuscript has been reproduced from the microfilm master. UMI films the text directly from the original or copy submitted. Thus, some thesis and dissertation copies are in typewriter face, while others may be from any type of computer printer.

The quality of this reproduction is dependent upon the quality of the copy submitted. Broken or indistinct print, colored or poor quality illustrations and photographs, print bleedthrough, substandard margins, and improper alignment can adversely affect reproduction.

In the unlikely event that the author did not send UMI a complete manuscript and there are missing pages, these will be noted. Also, if unauthorized copyright material had to be removed, a note will indicate the deletion.

Oversize materials (e.g., maps, drawings, charts) are reproduced by sectioning the original, beginning at the upper left-hand corner and continuing from left to right in equal sections with small overlaps.

Photographs included in the original manuscript have been reproduced xerographically in this copy. Higher quality 6" x 9" black and white photographic prints are available for any photographs or illustrations appearing in this copy for an additional charge. Contact UMI directly to order.

.

SOLID STATE NMR STUDIES OF SPIN PAIRS INVOLVING QUADRUPOLAR NUCLEI

by Scott C. Kroeker

Submitted in partial fulfillment of the requirements for the degree of

Doctor of Philosophy

at Dalhousie University

Halifax, Nova Scotia

January 1999

DALHOUSIE UNIVERSITY

FACULTY OF GRADUATE STUDIES

The undersigned hereby certify that they have read and recommend to the Faculty of

Graduate Studies for acceptance a thesis entitled "Solid State NMR Studies of Spin Pairs

Involving Quadrupolar Nuclei"

_____

 by   Scott Kroeker

in partial fulfillment of the requirements for the degree of Doctor of Philosophy.

Dated: _____ January 8, 1999 _____

External Examiner �_____ _____

Research Supervisor �_____ _____

Examining Committee �_____ _____

- _____ _____

- _____ _____

- _____ _____

ii
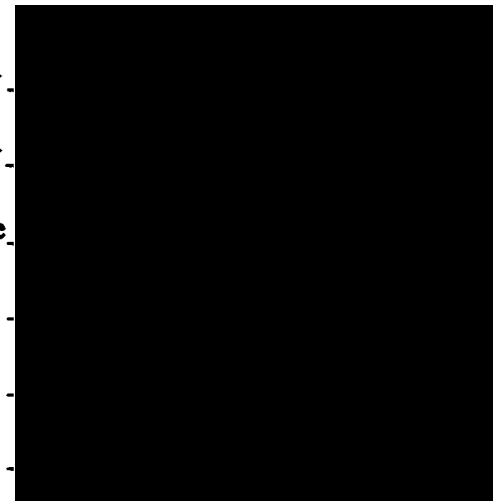
DALHOUSIE UNIVERSITY

DATE: _Jan. 8, 1999_

AUTHOR: _Scott C. Kroeker_

TITLE: _Solid State NMR Studies of Spin Pairs_
Involving Quadrupolar Nuclei

DEPARTMENT OR SCHOOL: _Chemistry_

DEGREE: _Ph.D_   CONVOCATION: _May_   YEAR: _1999_

iii

for Donna, of course

Table of Contents

List of Figures

List of Tables

Abstract

The use of NMR to characterize structure and dynamics in solids is becoming increasingly important. However, most spin-active nuclei are beset by anisotropic quadrupolar interactions which induce substantial broadening in NMR spectra of powders, leading to overlapping peaks which obscure c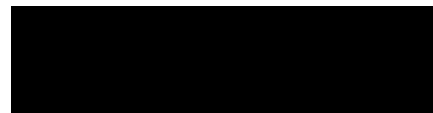rucial information such as quadrupole coupling constants, chemical shifts and J-couplings. Recent advances in this area have made it possible to obtain "isotropic" NMR spectra from which these data are available. The most powerful of these is multiple-quantum magic-angle spinning (MQMAS), a unique feature of which is that splittings due to J-coupling are, in some cases, *amplified*. This phenomenon is demonstrated by the direct observation of $^1J(^{63/65}Cu,^{13}C)$ in $K_3Cu(CN)_4$ and $^1J(^{11}B,^{31}P)$ in $(PhO)_3P-BH_3$ in NMR spectra of the quadrupolar nucleus. Theoretical considerations show that quadrupole-induced residual dipolar distortions do not influence MQMAS spectra, but may introduce differential dipolar splittings in single-quantum satellite transitions. In many situations, however, quadrupolar interactions are simply too large to be monitored directly by NMR. While their spectroscopic observation is the domain of nuclear quadrupole resonance, such nuclei can influence the appearance of NMR spectra of nearby, dipolar-coupled nuclei. For small to moderate quadrupolar interactions, first-order perturbation theory has been successful in describing these effects, but larger quadrupolar interactions demand a more rigorous treatment. The NMR lineshape of a spin-1/2 nucleus coupled to a spin-3/2 nuclide is analyzed by employing full-matrix diagonalization of the combined Zeeman-quadrupolar Hamiltonian operator for cases of axial symmetry. A highlight of this treatment is that the effective dipolar coupling constant may be obtained in favourable circumstances. In a bis(tribenzylphosphine)cuprate salt, its precise measurement facilitates an unambiguous determination of the anisotropic $^{63/65}Cu$, ^{31}P J tensor. A careful application of this theory to NMR spectra of solid copper(I) cyanide results in direct structural insight which has not been accessible by more conventional means.

List of Abbreviations and Symbols

3Q	three-quantum
5Q	five-quantum
7Q	seven-quantum
9Q	nine-quantum
bpy	4,4'-bipyridine
Bz	benzyl
CP	cross-polarization
CT	central transition
DACSY	dynamic-angle correlation spectroscopy
DAS	dynamic-angle spinning
DOR	double rotation
DW	dwell time
EFG	electric field gradient
FT	Fourier transform
GIAO	gauge-included atomic orbitals
HETCOR	heteronuclear correlation
LB	line broadening
MAS	magic-angle spinning
MQ	multiple-quantum
MQMAS	multiple-quantum magic-angle spinning
NMR	nuclear magnetic resonance
NQR	nuclear quadrupole resonance
PAS	principal axis system
Ph	phenyl
ppm	parts per million
REDOR	rotational-echo double resonance
rf	radiofrequency
SAS	switched-angle spinning

SATRAS	satellite transition spectroscopy
SQ	single-quantum
ssb	spinning sideband
ST	satellite transition
SW	spectral window
TMPP	trimethoxyphenylphosphine
TPPI	time-proportional phase incrementation
VACSY	variable-angle correlation spectroscopy
VADOR	variable-angle double rotation
VAS	variable-angle spinning

1	$[(PBz_3)_2Cu][CuBr_2]$
2	$[(PBz_3)_2Cu][PF_6]$
3	$[(TMPP)CuCl]$
4	$[(TMPP)CuBr]$
5	$[(TMPP)CuI]$
6	$[(TMPP)_2Cu][ClO_4]$

a_{ij}	eigenvector coefficients
$a(S,m_S)$	coefficients relating J to the splitting in MQMAS
$A_l(S,m_S)$	l^{th}-order coefficients of symmetric transition
A, B, C	orientation-dependent matrix elements
$\mathbf{B_0}, B_0$	applied magnetic field vector and magnitude
B_Q	frequency term in quadrupolar Hamiltonian
$B_Q^{(l)}$	l^{th}-order quadrupolar frequency contribution
C_Q	quadrupole coupling constant
$eq_{11}, eq_{22}, eq_{33}$	electric field gradient principal components
eq	electric field gradient tensor
eQ	nuclear quadrupole moment

E_i	Zeeman energy
F_i	components of an electric field
f_1, f_2	dimensions or projections in a 2D NMR spectrum
h	Planck's constant
$\hbar$	Planck's constant divided by 2π
$\mathcal{H}$	Hamiltonian operator
I	nuclear spin angular momentum number, typically 1/2
$\hat{I}_z$	z-component spin angular momentum
$\mathbf{J}$	indirect spin-spin coupling tensor
J_{11}, J_{22}, J_{33}	principal components of the indirect spin-spin coupling tensor
$J_\perp, J_\parallel$	perpendicular and parallel components of an axially symmetric indirect spin-spin coupling tensor
J_{iso}	isotropic indirect spin-spin coupling constant
J_{MQ}	splitting in MQMAS spectrum due to isotropic indirect spin-spin coupling constant
ΔJ	anisotropy of axially symmetric indirect spin-spin coupling tensor
k	ratio of multiple-quantum coefficients
k_i	phase-cycling experiment index
^1K	reduced indirect spin-spin coupling constant
m_S, m_I, m_1, m_2	magnetic quantum numbers
n	integer describing phase-cycling aliasing
N_i	total number of experiments in a given phase cycle
p	coherence
Δp	change in coherence
P_l	l^{th}-order Legendre polynomial
r_{IS}	internuclear separation between I and S
R_{DD}	dipolar coupling constant

R_{eff}	effective dipolar coupling constant
S	nuclear spin angular momentum quantum number
$\hat{S}_x$	x component spin angular momentum operator
$\hat{S}_z$	z component spin angular momentum operator
$\hat{S}_{\pm}$	raising/lowering spin angular momentum operators
t_1, t_2	multiple- and single-quantum evolution times
$\mathbf{T}$	transformation matrix
U	electric potential
$\mathbf{V}$	electric field gradient tensor
V_{ij}	electric field gradient tensor components
V_{11}, V_{22}, V_{33}	electric field gradient principal components
(x, y, z)	general principal axis system
(X, Y, Z)	general principal axis system
(α, β, γ)	Euler angles relating two principal axis systems
(α, β)	polar angles
β_1, β_2	"DAS-complementary" rotation angles
β_r	angle of sample rotation relative to magnetic field direction
γ	magnetogyric ratio
δ_{11}, δ_{22}, δ_{33}	chemical shift tensor principal components
δ_{iso}	isotropic chemical shift in ppm
δ^d, δ^p	diamagnetic and paramagnetic contributions to the chemical shift
$\delta_{\perp}$, $\delta_{\parallel}$	perpendicular and parallel components of an axially symmetric chemical shift tensor
δ_{MQ}	isotropic MQMAS peak position in ppm
η	asymmetry parameter of electric field gradient tensor
(ϕ, θ)	polar angles

φ	spin function
κ	skew of chemical shielding tensor
μ	nuclear magnetic moment
μ_0	permittivity constant
ν	resonance frequency
ν_0	carrier frequency
ν_L	Larmor frequency
ν_Q	quadrupole frequency
ν_r	sample rotation frequency
ν_{rf}	radiofrequency field frequency
ν_{iso}	isotropic chemical shift in Hz
ν_{MQ}	isotropic MQMAS peak position in Hz
$\Delta\nu$	frequency shift
$2\pi\nu_1$, $2\pi\nu_2$	multiple- and single-quantum precession frequency in rad s^{-1}
σ	chemical shielding tensor
σ_{11}, σ_{22}, σ_{33}	principal components of chemical shielding tensor
σ_{iso}	isotropic chemical shielding
σ^d, σ^p	diamagnetic and paramagnetic contributions to the chemical shielding
$\sigma_\perp$, $\sigma_\parallel$	perpendicular and parallel components of chemical shielding
ψ_1, ψ_2	multiple- and single-quantum evolution phases
Ω	span of a chemical shielding tensor
ϑ	rf phase in a phase-cycle

Acknowledgements

1. INTRODUCTION

1.1 Context

The interaction of a nuclear magnetic moment with an externally applied magnetic field was first identified in 1933 by Stern and Gerlach (*1*). Rapid developments ensued, leading eventually to the observation of *nuclear magnetic resonance* in bulk materials in 1945 (*2,3*). This phenomenon, initially thought to be of interest only to physicists,[1] has come to be exploited as a powerful tool for probing the detailed structure and dynamics of matter.

Chemical applications of nuclear magnetic resonance (NMR) became widespread after the discovery in 1950 (*4*) that local magnetic fields generated by surrounding atoms modify the net field "experienced" by a given nucleus to a measurable extent. This *chemical shielding* effect enabled chemists to observe separate resonance frequencies for nuclei in different chemical environments, thereby spawning a new era in structural elucidation of unknown compounds. As such, two driving forces – sometimes parallel, sometimes intertwining – have advanced a scientific understanding of NMR: interest in the basic physics of nuclear spin interactions, and an increasing urgency to derive techniques for solving particular chemical problems. In this utilitarian age, it is the latter which has fueled the most vigourous research, resulting in a remarkable array of tricks and techniques designed to coax "useful" information out of almost any type of matter.

In this context, it is interesting to note that the use of NMR to study quadrupolar nuclei in solids has received concerted attention only in the past decade or so. The impetus for this resurgence can be attributed at least in part to the culture's growing fascination with *materials science*, where powdered or disordered solids containing quadrupolar nuclei such as ^{11}B, ^{17}O and ^{27}Al are common. More generally, it is often pointed out that a truly multinuclear magnetic resonance

---

[1] Said E. M. Purcell in his Nobel lecture: "To see the world for a moment as something rich and strange is the private reward of many a discovery. But I'm afraid it has little bearing on the sober question we must, as physicists, ask ourselves: what can we learn from all this about the structure of matter?"

1

approach is likely to involve quadrupolar nuclei by virtue of the fact that nearly three-quarters of the elements in the periodic table have isotopes possessing quadrupole moments. Recent breakthroughs in this field have essentially focussed on methods to obtain fully resolved NMR signals from which isotropic chemical shifts and quadrupole coupling constants can be derived for each chemically distinct nuclear site in a solid.

The purpose of this thesis is to explore another fundamental nuclear spin interaction, namely that which arises between two spin-active nuclei by a direct dipolar interaction or by indirect electron-mediated processes. Although these couplings are well-understood for spin-1/2 species, some peculiar features arise when quadrupolar effects are considered. With the advent of peak-narrowing schemes used in the observation of quadrupolar nuclei, the time is ripe for a review of this theory and a presentation of new examples highlighting subtleties of such treatments. Underlying all aspects of this work is the premise that great care must be exercised in the interpretation of NMR spectra involving quadrupolar nuclei, where assumptions tacitly accepted in NMR of spin-1/2 systems may not be valid. With this heightened complexity, however, comes great richness which may be mined to gain valuable structural insight. It is hoped that the research presented herein exemplifies both the dangers and promise inherent in NMR of solids containing quadrupolar nuclei.

In the remainder of this chapter, some basic concepts necessary for this discussion are outlined, and a brief history of the progress and pitfalls associated with NMR of quadrupolar nuclei in solids is provided. Chapter 2 is devoted to the effects of direct dipolar and indirect spin-spin interactions in multiple-quantum magic-angle spinning NMR spectra of quadrupolar nuclei. The third chapter considers cases where the quadrupolar interaction is sufficiently prominent to preclude its direct observation by NMR, and details its influence on the NMR lineshapes of neighbouring spin-spin coupled spin-1/2 nuclei. In the final section, some directions for future research are suggested.

1.2 Spin Interactions in NMR

Zeeman. Although an NMR experiment can be described using "classical" concepts, the phenomenon of NMR originates in the quantum mechanical notion of *nuclear spin angular momentum*, S, by virtue of which a nucleus can be said to possess a *nuclear magnetic moment, μ*. To "observe" this property, it is necessary to introduce an external magnetic field with which μ can couple. In the presence of such a field, quantum theory tells us that $2S + 1$ discreet *energy levels*, designated by *spin states*, m_S, are available to the nucleus, the energies of which depend on the field strength, B_0. This interaction of μ with B_0 constitutes the essential axiom of nuclear magnetic resonance, and it is named for P. Zeeman, whose 1897 report of a broadening of the yellow sodium "D" line in the presence of a magnetic field was later identified as a splitting of the electronic energy levels (5). The *Zeeman splitting* was eventually generalized to include any energy level splitting due to the application of an external magnetic field.

The magnitude of the Zeeman interaction is governed by the magnetic moment and the strength of the applied field. In magnetic resonance, this is typically expressed in terms of the *magnetogyric ratio*, γ, for a given nuclide, which is the constant of proportionality relating the spin angular momentum and the magnetic dipole moment,

$$\mu = \gamma \, \mathbf{S} \, .\tag{1}$$

The transition energy for a given nucleus in a given field is commonly referred to as the *Larmor frequency*,

$$\nu_L = \frac{|\gamma| \, B_0}{2\pi}\tag{2}$$

harkening back to the turn-of-the-century theoretical work of Sir Joseph Larmor, explaining Zeeman's observations (6).

Chemical Shielding. In real systems, the exact transition frequency differs slightly from the pure Larmor frequency by virtue of electronic coupling with the applied field. This phenomenon modifies the net field experienced at the nucleus, and represents a *shielding*. Thus, the frequency of a given transition is typically written as

$$\nu = (1 - \sigma)\frac{|\gamma| B_0}{2\pi} \tag{3}$$

where σ is the shielding constant.

Naturally, the shielding due to the surrounding electronic structure depends on its positioning with respect to the external field. This orientation dependence is described by a tensor possessing, in principle, nine independent components:

$$\sigma = \begin{pmatrix} \sigma_{xx} & \sigma_{xy} & \sigma_{xz} \\ \sigma_{yx} & \sigma_{yy} & \sigma_{yz} \\ \sigma_{zx} & \sigma_{zy} & \sigma_{zz} \end{pmatrix}. \tag{4}$$

The antisymmetric portion of this tensor generally contributes negligibly to the observed shielding, and the symmetric tensor of interest comprises 6 independent elements:

$$\sigma = \begin{pmatrix} \sigma_{xx} & \sigma_{xy} & \sigma_{xz} \\ \sigma_{xy} & \sigma_{yy} & \sigma_{yz} \\ \sigma_{xz} & \sigma_{yz} & \sigma_{zz} \end{pmatrix}. \tag{5}$$

In its principal axis system (PAS), the shielding tensor is simply identified by three principal components:

$$\sigma = \begin{pmatrix} \sigma_{11} & 0 & 0 \\ 0 & \sigma_{22} & 0 \\ 0 & 0 & \sigma_{33} \end{pmatrix} \tag{6}$$

where the most shielded direction is along σ_{33} and the least shielded direction is along

σ_{11}. The net shielding along the direction of the applied field may be written in terms of the polar angles (ϕ,θ), (Figure 1):

$$\sigma = \sigma_{11}\sin^2\theta\cos^2\phi + \sigma_{22}\sin^2\theta\sin^2\phi + \sigma_{33}\cos^2\theta \ . \tag{7}$$

Experimentally, the effects of shielding are usually measured with respect to a particular *reference compound* as frequency shifts,

$$\delta_{sample} = 10^6 \left[\frac{\nu_{sample} - \nu_{ref}}{\nu_{ref}} \right] \ . \tag{8}$$

Thus, the *chemical shift* is a convenient, dimensionless measure of this quantity, calculated to be independent of B_0. Formally, the shift is related to the shielding by

$$\delta_{sample} = 10^6 \left[\frac{\sigma_{ref} - \sigma_{sample}}{1 - \sigma_{ref}} \right] \ . \tag{9}$$

The details of shielding are fully present in this nomenclature, provided universal conventions are rigorously maintained (7). Useful measures of the average shielding, the full range of shielding and the relative magnitudes of the components for a given nucleus in a specific environment are provided by the isotropic chemical shift, δ_{iso},
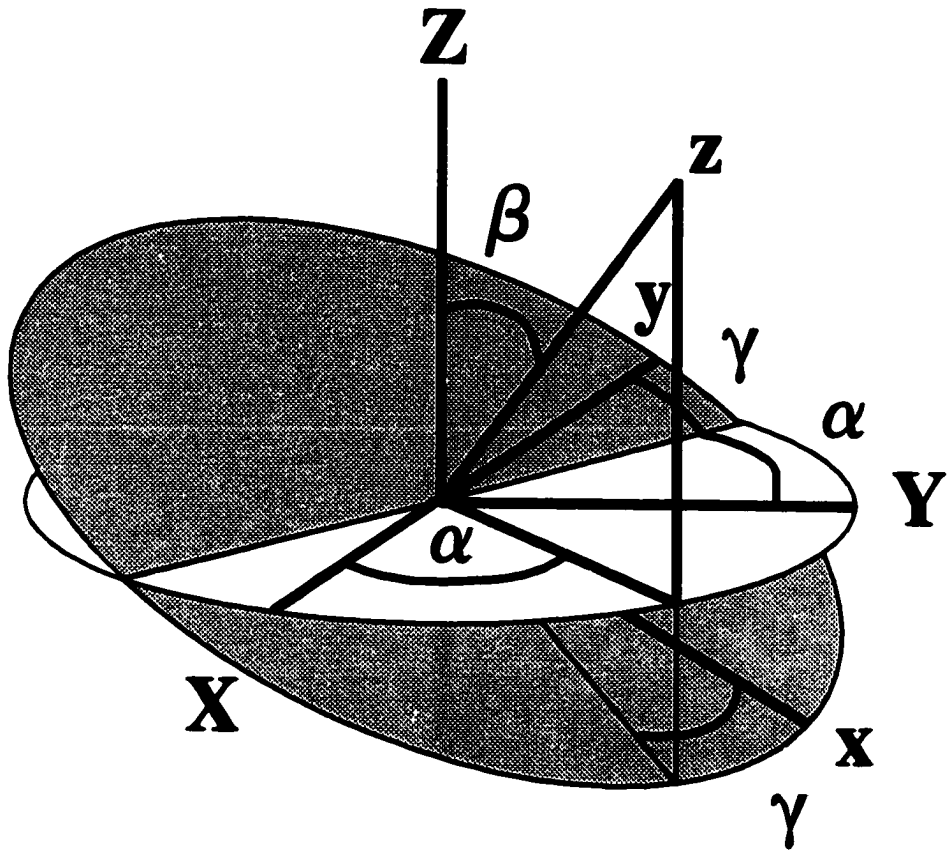
Figure 1   Depiction of the Euler angles relating the orientation of one principal axis system (x, y, z) with another (X, Y, Z). Under the "ZYZ" convention, a transformation is achieved by rotation by α about Z, followed by a rotation by β about the new Y, and finally a rotation about the new Z axis by γ. Note that for an axially symmetric tensor (x, x, z), rotation by γ has no influence on the relative tensor orientation, and (α,β) correspond to the polar angles, denoted also by (ϕ,θ).

the *span*, Ω, and the *skew*, κ:

$$\delta_{iso} = \frac{1}{3}(\delta_{11} + \delta_{22} + \delta_{33}) \qquad (10)$$

$$\Omega = \delta_{11} - \delta_{33}$$
$$= \sigma_{33} - \sigma_{11} \qquad (11)$$

$$\kappa = 3(\delta_{22} - \delta_{iso})/\Omega$$
$$= 3(\sigma_{iso} - \sigma_{22})/\Omega \ . \qquad (12)$$

Quadrupole. A second intrinsic property of some nuclei is known as the *electric quadrupole moment, eQ.* Possessed by all nuclei having a spin quantum number greater than 1/2, this characteristic is commonly described as a deviation from purely spherical nuclear charge distribution. This "charge anisotropy" couples with the *electric field gradient, eq* (or V), experienced by the nucleus, resulting in a series of energy levels.

The electric field gradient (EFG) itself is rather more interesting than the applied field that drives the Zeeman interaction, as it is intimately related to the environment in which the nucleus is situated. If U is considered to be the electrostatic potential at the nucleus due to the surrounding charges, the electric field, F, a vector quantity, generated by U is the *gradient*,

$$F_i = -\nabla U = \frac{-\partial U}{\partial x_i} \quad (x_i = x, y, z) \ . \qquad (13)$$

Likewise, the gradient of the electric field, a second-rank tensor quantity, is given by

$$V_{ij} = -\nabla^2 U = \frac{-\partial^2 U}{\partial x_i \partial x_j} \quad (x_i, x_j = x, y, z) \ . \qquad (14)$$

The EFG tensor is symmetric and traceless. Therefore, if represented in its principal

axis system, it can be specified by its largest component ($|V_{33}| \geq |V_{22}| \geq |V_{11}|$) and by an *asymmetry parameter*, $\eta = (V_{11} - V_{22})/V_{33}$. The magnitude of this interaction is conventionally indicated by the *quadrupole coupling constant*,

$$C_Q = eQV_{33}/h \qquad (15)$$

or by the *quadrupole frequency*, commonly (though not universally) written as,

$$\nu_Q = \frac{3\,C_Q}{2S(2S - 1)} \cdot \qquad (16)$$

The quadrupolar interaction lifts the degeneracy of the nuclear spin states, resulting in energy levels of

$$E(m_S) = \frac{h\,C_Q\,[3m_S^2 - S(S + 1)]}{4S(2S - 1)} \qquad (17)$$

for an axially symmetric EFG tensor. Invariant to the sign of m_S, equation (17) implies that for a spin-3/2 nucleus, a single transition of frequency ν_Q will be observed in a typical *nuclear quadrupole resonance* (NQR) experiment. Likewise, a spin-5/2 nucleus will exhibit two transitions with frequencies ν_Q and $2\nu_Q$, for ($\pm 3/2$, $\pm 1/2$) and ($\pm 5/2$, $\pm 3/2$), respectively. Beyond the limits of axial symmetry, exact expressions may be developed only for $S = 3/2$:

$$E(\pm 3/2) = + h\,(\nu_Q/2)\,(1 + \eta^2/3)^{1/2} \qquad (18)$$

$$E(\pm 1/2) = - h\,(\nu_Q/2)\,(1 + \eta^2/3)^{1/2} \qquad (19)$$

where the presence of a non-zero asymmetry parameter influences the measured transition frequency, but does not lift the degeneracy of the spin states, $|m_S|$. The theory for higher spin quantum numbers with non-axially symmetric EFG tensors is more complicated and not directly pertinent to the present purposes (8).

Zeeman-Quadrupole. Having introduced these nuclear spin interactions in isolation, no real problem is apparent: in the absence of an externally applied magnetic field, the nuclear spin states are quantized by the local electric field gradient with well-defined energy levels. However, upon the introduction of a magnetic field, the energy levels will be influenced by the interaction of the magnetic moment with B_0, and will depend on the orientation of the EFG tensor with respect to B_0. Consequently, the transitions observed in spectroscopic techniques will depend on the relative magnitudes of the Zeeman and quadrupolar interactions for a given orientation. If the Zeeman interaction can be considered a perturbation to the quadrupolar interaction, the associated spectroscopic experiment is called Zeeman-perturbed NQR (8). If the quadrupolar interaction is small compared to the Zeeman interaction, the spectroscopic technique is nuclear magnetic resonance (9). More troublesome in terms of categorization is the intermediate regime in which the two interactions are comparable in magnitude. In this case, perturbation theory is not valid and the full Zeeman-quadrupolar Hamiltonian must be considered in the calculation of energy level transitions. Many practical situations fall in this intermediate regime, where the current state of magnet technology is limited to fields insufficient to overwhelm the quadrupolar interaction, and orientation-dependent transition frequencies produce a wide range of resonances in a given sample.

For a "perfect" single crystal, the direct observation of quadrupolar transition frequencies is hampered only by the limited excitation bandwidth in Fourier-transform (FT) based nuclear resonance methods, forcing the experimentalist to the tedious task of locating, identifying and following a given peak as the crystal is reoriented with respect to B_0. With powder samples, however, the experimental implications of conflicting quadrupolar and Zeeman interactions are more critical. First, the signal intensity will be distributed over a wide frequency range, causing sensitivity problems. Second, significant technical difficulties are associated with the detection of very broad resonances by FT-based methods. Homogeneous radiofrequency (rf) excitation, for example, is generally restricted to a megahertz bandwidth, even for very strong pulses of short duration. Moreover, since the rf coil in an NMR probe

acts as both transmitter and receiver, acoustic ringing following a pulse prevents acquisition from commencing immediately after excitation, and the rapidly decaying time-domain signals associated with broad resonances are lost in this "ringdown" delay.

Fortunately, progress is being made with regard to these latter difficulties: noise-excitation schemes (10), improved echo sequences (11), and stepped-frequency (12,13) and field-swept methods (14), for example. However, even if it became possible to record by NMR faithful spectral representations of quadrupolar powder patterns many MHz wide, it would prove extremely difficult to distinguish overlapping contributions from nuclei in different chemical environments. For this reason, research efforts have generally sought methods to eliminate or reduce effects due to quadrupolar interactions in powdered solids, thereby improving spectral resolution.

One of the first contributions in this area described the effect of magic-angle spinning (MAS) on NMR lineshapes of half-integer quadrupolar nuclei (15,16). The details of the analysis are deferred to Chapter 2, but these groups showed that MAS is capable of reducing the width of the central (+1/2, -1/2) transition (CT) to about one-third its non-spinning value. The residual linewidth can be understood in terms of the mathematical expression describing transition frequencies under the influence of MAS as originating in an orientation-dependent term which is only partially scaled by rapid rotation at the magic angle. A natural extension of this work was the discovery that spinning sideband (ssb) peaks arising from certain single-quantum satellite transitions (STs) (m_S, m_S-1; m_S ≠ 1/2) under MAS exhibit even higher resolution than the CT, and that frequency shifts in their centre of gravity depend on the quadrupole coupling constant (17). The detection of ST ssbs under MAS can serve as a means to resolving individual sites, or alternatively, comprehensive lineshape simulations can be used to determine more detailed information about EFG and shielding tensors (18). Applicability is limited to species with fairly small quadrupole coupling constants since the whole spinning sideband manifold originating from all

single-quantum transitions must be acquired, and the experimental demands include fast, very stable spinning rates (*19*). While this represented an important step, there remained many applications for which better resolution was required to achieve adequate site differentiation.

A related suggestion was to spin the sample at an angle other than the "magic" angle. Presented initially in a trial-and-error fashion (*20*), subsequent theoretical studies of *variable-angle spinning* (VAS) showed that the optimal angle for resolution differed from one sample to the next, depending on the relative contributions of the various spin interactions (*21*).

In spite of these modest gains, substantial advances were only realized in the late 1980s, by a brilliant combination of spin physics and probe engineering wizardry. Two techniques were developed – essentially simultaneously – which produced purely isotropic peaks for half-integer quadrupolar nuclei. *Dynamic-angle spinning* (DAS) (*22,23*) and *double rotation* (DOR) (*24*) utilized probeheads designed to rotate the powder sample at two angles, sequentially or simultaneously, respectively. In this way, anisotropic quadrupolar contributions to central transition lineshapes are eliminated, and individual, chemically distinct sites can be resolved.

The development of these new probe technologies spawned a number of related multidimensional methods – variable-angle correlation spectroscopy (VACSY) (*25*), variable-angle double rotation (VADOR) (*26*), dynamic-angle correlation spectroscopy (DACSY) (*27*) and switched-angle spinning (SAS) (*28*) – each of which accomplish the desired correlation or separation by including the angle of macroscopic sample rotation as a new variable. Ironically, the very genius that was heralded as initiating this breakthrough in NMR of half-integer quadrupolar nuclei soon became its principal drawback: these probeheads were not commercially available, and their construction was tedious and expensive. Perhaps it was this frustration that prepared the stage for a new method, which would render high-resolution NMR of half-integer quadrupoles in solid materials more accessible.

In 1995, a novel approach to this problem was presented which accomplished

the elimination of anisotropic quadrupolar effects without resorting to specially designed probeheads. *Multiple-quantum magic-angle spinning* (MQMAS) (29) is a two-dimensional NMR technique based on the observation that anisotropic broadening for certain multiple-quantum transitions in half-integer quadrupolar nuclei is relatively minor. A judicious choice of transitions in combination with standard MAS can be processed to yield a spectrum containing isotropic peaks, the positions of which reflect the chemical shift and quadrupole coupling tensors. This innovation rendered accessible to NMR spectroscopists high-resolution NMR of half-integer quadrupolar nuclei in solids, previously the exclusive domain of those few having DAS or DOR probes. Moreover, MQMAS is more effective and versatile in many situations than its multi-angle counterparts. Of course, some drawbacks remain, and vigourous basic research has been motivated by the advent of MQMAS. However, many significant obstacles have been overcome by this method, and it promises to become a routine analytical tool in materials chemistry.

Indirect Spin-Spin Coupling. With the increased resolution available by MQMAS, it is becoming easier to measure *indirect spin-spin interactions*, *J*-couplings, by directly observing the quadrupolar nucleus itself (30). This goal is aided not only by the elimination of inhomogeneous broadening due to second-order quadrupolar effects, but by an *amplification* of the splitting due to *J*-coupling in some cases, as shall be shown in Chapter 2.

Indirect spin-spin coupling is an important NMR interaction which arises from the coupling of nuclear spins via the intervening electronic structure. As such, *J*-coupling can provide fundamental information about molecular structure and chemical bonding (31,32,33). The magnitude of *J* depends on the orientation of a spin pair in the magnetic field; thus, it is described by a second-rank tensor

$$J = \begin{bmatrix} J_{xx} & J_{xy} & J_{xz} \\ J_{yx} & J_{yy} & J_{yz} \\ J_{zx} & J_{zy} & J_{zz} \end{bmatrix} . \tag{20}$$

As a first approximation, it is assumed that J tensors involving directly bonded nuclei are axially symmetric. In this case, the interaction is conventionally represented in its PAS by separation into isotropic and anisotropic components:

$$J = \begin{bmatrix} J_{\perp} & 0 & 0 \\ 0 & J_{\perp} & 0 \\ 0 & 0 & J_{\parallel} \end{bmatrix} \tag{21}$$

$$J_{iso} = (2J_{\perp} + J_{\parallel})/3 \tag{22}$$

$$\Delta J = J_{\parallel} - J_{\perp} . \tag{23}$$

The anisotropic character of J is often ignored, as it does not influence the splittings in NMR spectra of isotropic media, and its effect on NMR spectra of ordered phases is masked by its similarity to the direct dipolar interaction (see below). Variations in J due to orientational effects are indeed small for many systems, and may justifiably be neglected in many cases. However, other cases exist for which ΔJ may *not* be ignored without introducing significant errors into the analytical results.

For a given heteronuclear spin pair (I, S), the observed I resonance will be split into $2S + 1$ peaks separated by the isotropic J-coupling, provided the spin states of both nuclei are quantized by the Zeeman interaction with lifetimes which are long with respect to $1/J(I,S)$. In solution, rapid molecular tumbling may create a fluctuating electric field gradient at a quadrupolar S nucleus, resulting in efficient spin-lattice relaxation (*34*). Consequently, multiplets in the I spectrum due to J-coupling to S are broadened, and in extreme cases, completely "self-decoupled" (*35,36*). By contrast, restricted motion in solids results in relatively long relaxation

times, enabling the observation of spin-spin coupling to quadrupolar nuclei subject to very large quadrupolar interactions. Under such circumstances, the spin I lineshape may be distorted with respect to the symmetric multiplet, the extent of this distortion depending on the ratio, ν_Q/ν_L. Thus, it is often advantageous to measure J-couplings involving quadrupolar nuclei by solid-state NMR. In fact, a large number of recent solid-state NMR studies of $I=1/2$ nuclei have demonstrated the feasibility of measuring J-couplings between spin-1/2 and quadrupolar spins (see, for example: *37,38*).

On the other hand, there are few reports concerning J-couplings in solid-state NMR spectra of quadrupolar nuclei (*39,40*) primarily because of the failure of MAS to completely suppress the anisotropy due to second-order quadrupolar effects. In spite of the capacity of both DOR and DAS for achieving isotropic peaks, J-couplings do not appear to have been reported. The examples presented in this thesis represent some of the first direct measurements of J from high-resolution NMR spectra of half-integer quadrupolar nuclei.

Direct Dipole-Dipole Coupling. Accompanying indirect spin-spin coupling is the *direct dipole-dipole interaction*, typically characterized by the dipolar coupling constant,

$$R_{DD}(I, S) = \left(\frac{\mu_0}{4\pi}\right)\left(\frac{\hbar}{2\pi}\right)\gamma(I)\,\gamma(S)\,\langle r_{I,S}^{-3}\rangle \ . \tag{24}$$

The distance-dependence in the denominator makes R_{DD} an attractive parameter for structural determinations. However, in the presence of dipolar-coupled neighbours, the implications of combined Zeeman-quadrupole nuclear spin interactions extend beyond the identification of the appropriate eigenstates. In contrast to coupled spin-1/2 nuclei where the pure Zeeman states, $m_I = \pm 1/2$, are assumed to be directed parallel or anti-parallel to the field (the Zeeman interaction is generally far greater than the dipolar interaction: $\nu_L \gg R_{DD}$), it is also necessary to employ the appropriate treatment reflecting the fact that the S spin angular momentum may contain non-negligible contributions "perpendicular" to the applied magnetic field. Thus, these

transverse components must be evaluated and considered in the dipolar Hamiltonian operator. Upon performing this exercise, it becomes apparent that these subtleties may manifest themselves prominently in NMR spectra of either S or I.

The application of first-order perturbation theory relating to the observation of a spin-1/2 nucleus coupled to a quadrupolar spin was first presented by Casabella in 1964 to account for "unusual asymmetric structure" in the ^{19}F NMR lineshape of polycrystalline BF_3 (*41*). This treatment was later reviewed to explain ^{13}C MAS lineshapes in the presence of a neighbouring ^{14}N nucleus (*42*), and generalized by Olivieri and coworkers to simple analytical expressions for the dipolar frequency shifts exhibited by any I, S ($I = 1/2$; $S > 1/2$) pair (*43,44,45*). These equations have found widespread use in recent years (*37*), but are limited to cases where the quadrupolar eigenstates are accurately described as perturbations of the Zeeman states. Beyond this limit, it is necessary to include a second-order correction (*46*), or to diagonalize the full Zeeman-quadupolar Hamiltonian operator (*47*). Early examples of the latter include ^{13}C NMR of a single crystal of $K_2Pt(CN)_4Br_{0.3}\cdot 3H_2O$ (*48*) and ^{31}P powder MAS lineshapes of bis(triphenylphosphine)copper(I) nitrate (*49*). The stated purpose of much of this research has been a desire to gain insight into the neighbouring quadrupole. It shall be shown, however, that only in favourable cases can reliable information about S be determined.

What have not been examined until recently (*50,51*), are the corresponding effects in spectra of the quadrupolar nucleus. In particular, MQMAS has forced a reconsideration of these matters, as "residual dipolar couplings" may, in principle, be resolved under peak-narrowed conditions.

These studies are especially timely because of the growing interest in quadrupolar nuclei, aided by breakthroughs like MQMAS. Nuclear magnetic resonance is becoming a powerful and routine tool in the characterization of solid organometallic compounds. Ligands containing spin-1/2 nuclei such as carbon-13, nitrogen-15, phosphorus-31, silicon-29 and tin-119 bonded to metallic centres such as copper-63/65, aluminum-27, cobalt-59, manganese-55 abound in the chemical

literature. It is important that the valuable information embedded in NMR spectra be recognized for what it is, and not ignored or misinterpreted. The following chapters are intended to represent careful applications of NMR to solid compounds in which these concepts can be more fully explored.

2. MULTIPLE-QUANTUM MAGIC-ANGLE SPINNING

The enthusiasm generated by multiple-quantum magic-angle spinning (MQMAS) is evidenced by the spate of research reports in the scientific literature. Since the 1995 publication of Frydman and Harwood's communication in the *Journal of the American Chemical Society* (*29a*), at least 80 papers have appeared, describing applications of MQMAS to a wide variety of solids. By far, the most-studied nuclei are ^{23}Na and ^{27}Al, owing, at least in part, to their favourable NMR properties and technological relevance. Other nuclides which have been examined by MQMAS include ^{11}B, ^{17}O, ^{55}Mn, ^{59}Co, ^{87}Rb and ^{93}Nb. The resolving power of this method has been applied to the study of clay minerals (*52*), cements (*53*), oxide glasses (*54*), and zeolite framework (*55*) and adsorbates (*56*), to select just a few examples. Properties such as phase transitions (*57*), crystallinity (*58,59*), impurity phases (*60*) and surface structure (*61*) have been probed with the aid of MQMAS. Furthermore, creative combinations of MQMAS with DOR (*62*), VAS (*63*), heteronuclear correlation (HETCOR) (*64,65*), cross-polarization (CP) (*66*) and rotational-echo double resonance (REDOR) (*67*) bespeak the versatility of this technique, and hint at its tremendous potential for structural elucidation. These successful applications, along with the intense research energies that have been, and continue to be, invested in MQMAS, mark a modest revolution in solid-state NMR of half-integer quadrupolar nuclei.

2.1 Why It Works

The Hamiltonian energy operator describing a single half-integer quadrupolar spin in the presence of a static magnetic field contains terms arising from the Zeeman, quadrupolar and chemical shielding interactions:

$$\mathcal{H}_{total} = \mathcal{H}_Z + \mathcal{H}_{Q(1)} + \mathcal{H}_{Q(2)} + \mathcal{H}_{CS} . \tag{25}$$

The quadrupolar Hamiltonian may be separated into two terms representing first- and second-order perturbation corrections to the Zeeman Hamiltonian. In the ensuing discussion, it shall be assumed that the Zeeman term is much larger than the other terms, and that the quadrupolar interaction is much larger than the chemical shielding. This assumption is valid in most cases to which MQMAS is applicable, and validates treating the quadrupolar interaction as a perturbation to the Zeeman eigenstates (*21*). In the Zeeman rotating frame, the effective Hamiltonian can be written as the sum of three secular terms which commute with the z component of the spin angular momentum, $\hat{S}_z$:

$$\mathcal{H}_{eff} = \mathcal{H}_{Q(1)} + \mathcal{H}_{Q(2)} + \mathcal{H}_{CS} . \tag{26}$$

Considering only the isotropic chemical shift, ν_{CS}, the Hamiltonian describing chemical shielding is of the form

$$\mathcal{H}_{CS} = \nu_{CS} \hat{S}_z . \tag{27}$$

The separation of the quadrupolar Hamiltonian into first- and second-order terms derives from the use of perturbation theory to describe its effect on nuclear spin states subject to a dominant Zeeman field. In the "laboratory frame", defined by rotation at the Larmor frequency about the z axis of the applied magnetic field, $\mathcal{H}_Q$ is rendered time-dependent. Average Hamiltonian theory (*68*) may be used to remove this dependence, employing the Magnus expansion to approximate the average value of the Hamiltonian operator over a single Larmor period. The details of this procedure are tedious and lengthy, and have been presented elsewhere (*69*). If only terms which

commute with $\hat{S}_z$ are retained, the resulting expressions reduce to those obtained by standard perturbation theory carried to second order. The first-order quadrupolar Hamiltonian contains a frequency term, $B_Q(\phi,\theta)$, which depends on the crystallite orientation in the applied magnetic field,

$$\mathcal{H}_{Q(1)} = B_Q(\phi,\theta)[\hat{S}_z^2 - S(S+1)/3] \tag{28}$$

where

$$B_Q(\phi,\theta) = \frac{\nu_Q}{2}(3\cos^2\theta - 1 + \eta\sin^2\theta\cos 2\phi) . \tag{29}$$

The dependence of $\mathcal{H}_{Q(1)}$ on $\hat{S}_z^2$ implies that for single-quantum transitions where spin states $|m_1|$ and $|m_2|$ differ, the resulting peaks will have a characteristic lineshape due to the orientation-dependence associated with $B_Q(\phi,\theta)$. By the same token, symmetric transitions $(+m_S, -m_S)$ are independent of the EFG orientation with respect to $\mathbf{B}_0$. This relationship is responsible for the well-known independence of the central $(+1/2, -1/2)$ transition to first-order quadrupolar effects. The second-order component of $\mathcal{H}_Q$ is more complicated, and is presented in full elsewhere (70). Proportional to the ratio of the square of the quadrupole frequency to the Larmor frequency, ν_Q^2/ν_L, this term introduces anisotropy into all transitions. As such, the presence of second-order quadrupolar effects can preclude the resolution of individual, crystallographically distinct sites in solid-state NMR experiments, obscuring information about chemical shifts and site populations.

Magic-angle spinning has been employed in studies of half-integer quadrupolar nuclei with some success (15,16). A theoretical analysis of the time-averaged precession frequencies using Wigner rotation matrices (71) leads to the following expression for symmetric transitions, rotating about an angle, β_r, relative to the applied magnetic field direction:

$$\nu(S, m_S, \beta_r) = 2m_S \nu_{CS} + A_0(S, m_S) B_Q^{(0)}$$

$$+ A_2(S, m_S) B_Q^{(2)}(\phi, \theta) P_2(\cos\beta_r) \tag{30}$$

$$+ A_4(S, m_S) B_Q^{(4)}(\phi, \theta) P_4(\cos\beta_r) .$$

The coefficients, $A_i(S, m_S)$, are functions of the spin quantum number, S, and the symmetric transition, m_S (see Table 1):

$$A_0(S, m_S) = 2m_S[S(S+1) - 3m_S^2]$$

$$A_2(S, m_S) = 2m_S[8S(S+1) - 12m_S^2 - 3] \tag{31}$$

$$A_4(S, m_S) = 2m_S[18S(S+1) - 34m_S^2 - 5] .$$

The isotropic second-order quadrupolar shift is

$$B_Q^{(0)} = \frac{-\nu_Q^2(1 + \eta^2/3)}{30\nu_L} \tag{32}$$

whereas anisotropic contributions to the lineshape arise from the presence of terms containing $B_Q^{(2)}(\phi,\theta)$ and $B_Q^{(4)}(\phi,\theta)$.

Magic-angle spinning alone is capable of scaling the second-rank term to zero due to the angular dependence of the second-order Legendre polynomial,

$$P_2(\cos\beta_r) = \frac{1}{2}(3\cos^2\beta_r - 1) . \tag{33}$$

However, no single angle, β_r, will simultaneously zero both $P_2(\cos\beta_r)$ and the fourth-order Legendre polynomial,

$$P_4(\cos\beta_r) = \frac{1}{8}(35\cos^4\beta_r - 30\cos^2\beta_r + 3) . \tag{34}$$

Under conditions of MAS, $P_4(\cos\beta_r) \approx -0.4$ and serves as a scaling factor for the

Table 1   The coefficients $A_l(S, m_S)$, calculated from equations (31)

S	m_S	$A_0(S, m_S)$	$A_2(S, m_S)$	$A_4(S, m_S)$
3/2	1/2	3	24	54
	3/2	-9	0	-42
5/2	1/2	8	64	144
	3/2	6	120	228
	5/2	-50	-40	-300
7/2	1/2	15	120	270
	3/2	27	288	606
	5/2	-15	240	330
	7/2	-147	-168	-966

$B_Q^{(4)}$ anisotropic lineshape contribution. This phenomenon is responsible for the characteristic central transition lineshapes in MAS spectra of half-integer nuclei, thus limiting the resolution available from conventional one-dimensional MAS spectra.

One approach to the resolution of this conundrum is to spin the sample *simultaneously* at the roots of both the second- and fourth-order Legendre polynomials, thus eliminating both anisotropic terms in equation (30) (*24*). The success of this double rotation experiment has been limited by the mechanical difficulties associated with simultaneous and rapid rotation of the inner and outer rotors. Another clever way to effectively eliminate the quadrupolar broadening terms is to spin the sample *sequentially* at carefully chosen angles, β_1 and β_2, allowing the system to evolve during the corresponding times, t_1 and t_2. In this manner, dynamic-angle spinning (*22,23*) achieves the refocussing of the anisotropic terms in the form of an echo observed at times determined by the so-called "DAS condition":

$$P_2(\cos\beta_1)t_1 = -P_2(\cos\beta_2)t_2 ,$$

$$P_4(\cos\beta_1)t_1 = -P_4(\cos\beta_2)t_2 . \qquad (35)$$

A third technique for the complete removal of quadrupolar broadening avoids the tricky mechanical manipulations required by DOR and DAS, opting instead to perform the averaging in spin space through the correlation of multiple- and single-quantum coherences. The basic principle of multiple-quantum magic-angle spinning (*29*) is twofold. First, by spinning the sample at the magic angle, anisotropy due to the second-rank quadrupolar frequency, $B_Q^{(2)}(\phi,\theta)$, is eliminated by the usual scaling of $P_2(\cos\beta_r)$. Second, the remaining fourth-rank anisotropic term is refocussed at a time which depends on the evolution of multiple-quantum coherences.

The basic pulse sequence used to accomplish this is simple (Figure 2). An initial pulse (or series of pulses) creates multiple-quantum coherence which is allowed to evolve for a time, t_1. A second pulse transfers this coherence into the single-quantum, central transition for detection. An echo is observed at a time, t_2, following the transfer. The experiment is performed in the standard two-dimensional
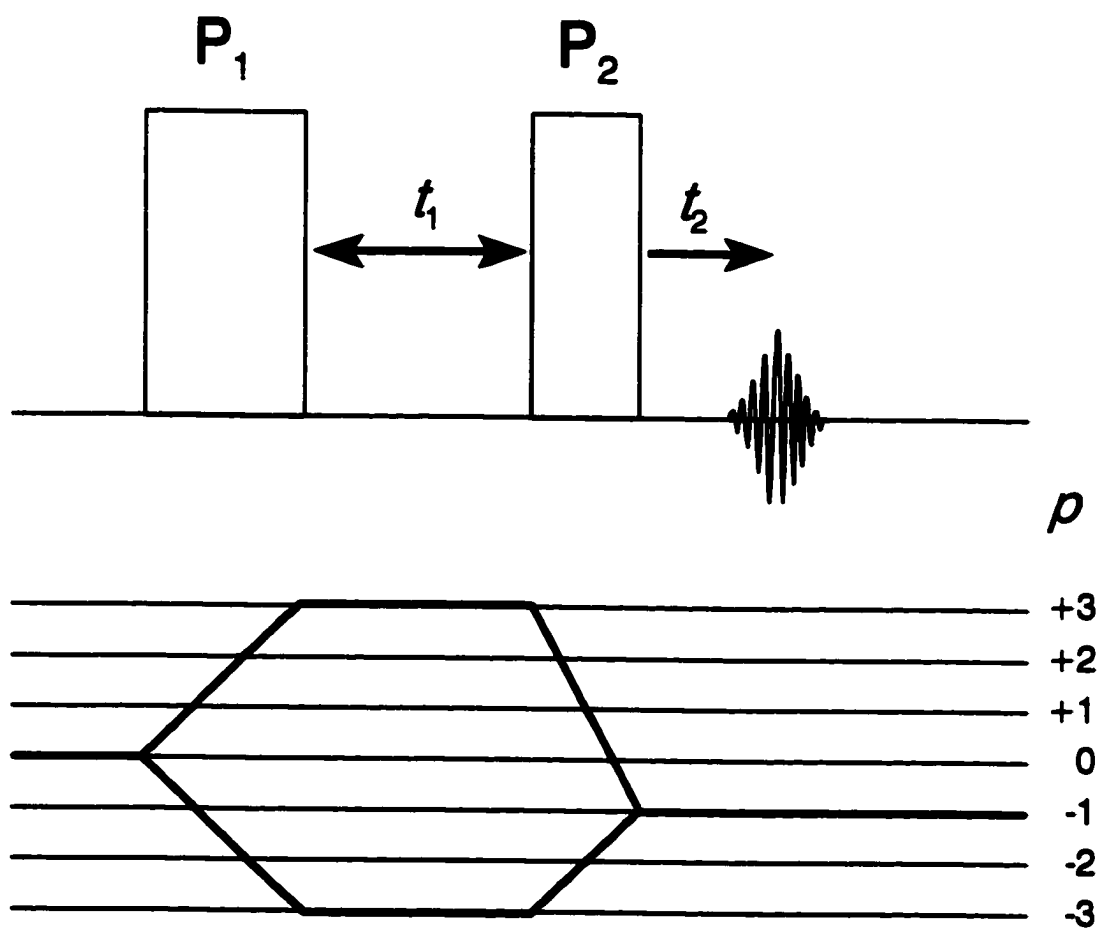
Figure 2   General pulse sequence for an MQMAS experiment. The lower portion of the diagram illustrates coherence pathways corresponding to echo ($p = -3$) and anti-echo ($p = +3$) acquisition for triple-quantum (3Q) MAS of a spin-3/2 nuclide.

manner, with increments in the interpulse delay, t_1, and phase cycling to select a particular coherence pathway. A plot of the echo maxima as a function of the total evolution time, $t_1 + t_2$, results in a free induction decay representing an isotropic spectrum in which all quadrupolar anisotropic terms have vanished.

The appearance of an echo at t_2 is based on the duration of t_1, as well as on the nuclear spin and the symmetric MQ transition selected. The evolution phases during t_1 and t_2 can be expressed as the products of the precession frequencies, $2\pi\nu_1$ and $2\pi\nu_2$, and the time they are allowed to evolve. Utilizing equation (30) under MAS, the second-rank broadening contribution disappears, and the equations reduce to:

$$\psi_1 = 2\pi\nu_1 t_1$$
$$= [2m_S\nu_{CS} + A_0(S,m_S)B_Q^{(0)} + A_4(S,m_S)B_Q^{(4)}(\phi,\theta)P_4(\cos\beta_r)]t_1 \tag{36}$$

$$\psi_2 = 2\pi\nu_2 t_2$$
$$= [-\nu_{CS} + A_0(S,-1/2)B_Q^{(0)} + A_4(S,-1/2)B_Q^{(4)}(\phi,\theta)P_4(\cos\beta_r)]t_2 \quad . \tag{37}$$

In order to refocus the anisotropy inherent in the last term, the evolution times must satisfy

$$A_4(S,m_S)t_1 + A_4(S,-1/2)t_2 = 0 \tag{38}$$

and the echo maximum will occur at

$$t_2 = \frac{-A_4(S,m_S)}{A_4(S,-1/2)}t_1 = kt_1 \quad . \tag{39}$$

The signal collected in this manner will contain contributions from the *isotropic* chemical and quadrupolar shifts, but none from the *orientation-dependent* terms involving $B_Q(\phi,\theta)$. Hence, inhomogeneous broadening quenched, the spectrum consists of narrow resonances, despite the powder nature of the sample.

Unless signal acquisition commences at the echo maximum, simple f_1 and f_2 projections will not yield the desired isotropic and anisotropic peaks. Some groups (58) elect to juxtapose axes representing "anisotropic", "quadrupole-induced shift" and "isotropic chemical shift" projections with the spectrum as visual guides for the estimation of certain NMR parameters. In order to avoid these sometimes-confusing skew projections, a common approach is to *shear* the spectrum (29b,72). Essentially a t_1-dependent first-order phase correction, the shearing transformation tilts the resonances according to k such that anisotropic lineshapes are parallel to f_2 and the isotropic spectrum is simply the f_1 projection.

It is clear, on the basis of equations (36) and (37), that peak positions in the isotropic f_1 dimension will depend on both the isotropic chemical shift *and* the isotropic second-order quadrupole shift. In addition, the spin- and transition-dependence of the coefficients introduces an (S, m_S)-dependence into the observed peak positions, ν_{MQ}. The actual relation of ν_{MQ} to ν_{CS} and $B_Q^{(0)}$ can be worked out by a careful consideration of the evolution phases (72).

Here it is necessary to note that two conventions have been propagated in the literature for scaling in the f_1 dimension. Conceptually, the difference depends on whether one considers the evolution time as beginning with the initial multiple-quantum excitation, or with conversion to the observable single-quantum coherence. This is not a fundamental problem, but the determination of chemical shifts and quadrupolar parameters depends critically on the method of processing the raw data, and the latter appears to be favoured from the standpoint of comparing linewidths. In this work, the total evolution of the spin system is understood to commence at the excitation pulse, thus introducing a frequency scaling factor of $(1 + k)$ in the spectral width. A comprehensive discussion of these two methods is presented in reference (73).

A general expression for peak positions in the isotropic dimension may be developed. In Hz, calculated as an offset from the carrier frequency,

$$\nu_{MQ} = \left[\frac{k - 2m_S}{1 + k}\right] \nu_{iso} + \left[\frac{k + \dfrac{A_0(S, m_S)}{A_0(S, -1/2)}}{1 + k}\right] B_Q^{(0)} \qquad (40)$$

where NMR detection of the $p = -1$ coherence (i.e., $m_S = -1/2$) is assumed, and the sign of m_S chosen will depend on the sign of the fourth-rank coefficient to be averaged. From this equation, it is apparent that in addition to narrowing individual resonances by the elimination of anisotropic broadening terms, MQMAS has the potential to provide increased site resolution by the prefactors in parentheses. However, it turns out that these two factors are of opposite sign, with the consequence that whether greater or lesser resolution is realized will depend on the particular chemical shift and quadrupole parameters of the system, as well as on the applied magnetic field strength.

2.2 How It Works

Not surprisingly, a number of factors contribute to the success of MQMAS experiments. Spinning speed, pulse lengths, rf field strength and phase-cycling, for example, are all crucial to the effective implementation of MQMAS. Moreover, the particularities of the sample, the nucleus under investigation and the information desired from the experiment will influence the MQMAS variation to be employed. In the following sections, some of these experimental considerations are highlighted.

Pulse optimization. Key to the success of MQMAS is the efficient excitation of multiple-quantum (MQ) coherences and their transfer to the observable single-quantum (SQ) central transition. Accordingly, pulse optimization of the experiment has attracted much attention (*29b,58,74,75,76*). In the initial report of this technique, the excitation of MQ coherence was effected using a multi-pulse sequence analogous to that used in solution-state experiments (*29a*). Subsequently, several groups realized that for solid-state systems, a single pulse of appropriate duration can improve the excitation efficiency by up to an order of magnitude (*29b,74,75*). This one-pulse excitation scheme, in combination with a single transfer pulse, composes the two-pulse sequence that has become standard in applications of MQMAS (Figure 2). Other related proposals for maximizing efficiency are shaped pulses (*77*) and *xy* composite pulses (*78*).

Not unexpectedly, efficient excitation of MQ coherences depends crucially on a variety of factors. An important aspect is the ratio of the quadrupole frequency to the rf field strength, ν_Q/ν_{rf}. Numerical simulations of a spin-3/2 system (*76*), for example, suggest that the generation of 3Q coherence for $\nu_Q/\nu_{rf} = 1.25$ is about twice that for a ratio of 2.5, and about four times that for $\nu_Q/\nu_{rf} = 5$. Similar relationships are observed for other spin quantum numbers. For small ratios of ν_Q/ν_{rf}, well-defined maxima are observed in the coherence build-up curves, implying that there is an optimal pulse width. Interestingly, no clear maxima are present for higher ratios, where MQ excitation efficiency is very low to begin with. Table 2 lists theoretical maxima for the generation of 3Q coherence based on values of ν_Q/ν_{rf} less than two.

Table 2   Theoretically optimized pulse angles for the generation (θ_1) and transfer (θ_2) of triple-quantum coherences (76)

S	$\theta_1(°)$	$\theta_2(°)$
3/2	240	55
5/2	180	60
7/2	120	45
9/2	90	35

Similar calculations have been carried out for the second pulse to estimate the optimal transfer efficiency of the 3Q coherence into 1Q (76). Once again, the greatest efficiency is observed for small ratios ν_Q/ν_{rf}. In this case, maxima in the transfer curves are observed for all ratios, coinciding about particular pulse angles, listed in Table 2.

A number of conclusions may be drawn from these studies. First, within the range of currently available radiofrequency amplifiers, the greatest overall signal will be realized by using the highest possible rf field strength. Simulations of the total theoretical signal intensity suggest that the largest observable signal in 3QMAS is obtained when ν_{rf} is about twice ν_Q (76). This condition is not generally attainable, at present, since ν_{rf} is usually smaller than 200 kHz, and values of ν_Q less than 100 kHz, on modern high-field spectrometers, usually have negligible second-order quadrupolar effects. Second, even in optimal cases, the largest observable signal from the two-pulse experiment is predicted to be but a fraction of that obtainable for the central transition using single-pulse excitation. For a spin-3/2 nucleus, this fraction is 55%, and decreases rapidly to 35% for spin-5/2 (76). A third implication of these computations is that excitation and transfer will depend critically on the magnitude of the quadrupole coupling. This characteristic of the basic MQMAS experiment is addressed in the next section.

Site Quantification. As evidenced by the strong dependence of MQ excitation and transfer on the magnitude of the quadrupole coupling, equally populated crystallographic sites differing in ν_Q will not have the same signal amplitude in the final spectrum, thereby circumscribing the general utility of MQMAS for determining the relative abundance of different sites. This limitation has motivated different approaches to the quantification of sites in MQMAS. Perhaps the most intuitive is to use the NMR parameters for individual sites as determined from subspectral slices and the isotropic spectrum to fit the total MAS lineshape through variations in the peak amplitudes (*29b*). However, when the crystallinity of the sample is imperfect, distributions in quadrupole couplings and chemical shifts may result in poorly defined singularities in the MAS lineshape, weakening its sensitivity to relative site intensities. In such cases, it may be necessary to compute a calibration curve relating the signal intensity to the quadrupolar interaction for a given rf field strength (*79*).

A more elegant approach is to use a pulse sequence which is less sensitive to the quadrupolar interaction. Such a sequence, utilizing a spin-locking field rather than a simple nutation pulse, has been recently reported to efficiently interconvert single- and triple-quantum coherences in spin-3/2 systems, with only a weak dependence on the quadrupole coupling constant (*80*). Hence, *rotation-induced adiabatic coherence transfer* (RIACT) can replace the second nutation pulse in the original MQMAS sequence, converting 3Q coherence to observable 1Q coherence. Moreover, generation of the initial 3Q coherence can be effected by beginning the sequence with a selective pulse on the central transition and transferring this 1Q to 3Q *via* RIACT. The superior performance of this conversion may be illustrated by comparing simulations of the 3Q excitation of RIACT to that of the nutation pulse as a function of the quadrupolar coupling constant: increasing C_Q from 1.0 to 3.6 MHz results in a reduction of total 3Q coherence of about 20% by RIACT, whereas the same variation produces a four-fold attenuation using a nutation pulse. In terms of absolute sensitivity, RIACT is observed to provide a significant improvement over the nutation method for coherence transfer, but is somewhat less efficient in its ability to

generate the initial 3Q coherence. Thus, maximization of signal-to-noise can be achieved by using a simple nutation pulse for excitation, and RIACT for transferring 3Q to 1Q. If signal sensitivity is not critical, better quantitation can be obtained with RIACT for both excitation and transfer.

Spinning Sidebands. In general, spinning sidebands separated by the spinning frequency, ν_r, are observed in MAS spectra when ν_r is less than the spectral width of an inhomogeneously broadened stationary powder pattern. This can complicate spectral analyses by overlapping with other resonances, degrading the peak intensity and by modifying the lineshapes of individual peaks. In MQMAS this problem is exacerbated, since sidebands arising from large quadrupole coupling are no longer separated by the spinning frequency, but by some fraction thereof (74,81). The effective Hamiltonian for the full evolution period, $t_1 + t_2$, constructed using fictitious spin-1/2 operator formalism, contains a time-dependent term responsible for the appearance of spinning sidebands (74). This term is scaled by $(1 + k)^{-1}$. In 3QMAS of spin-3/2 nuclei, $k = 7/9$ and the sidebands are separated by $0.56\nu_r$. More severe is the scaling in 3Q and 5QMAS for spin-5/2 nuclei of $0.39\nu_r$ and $0.32\nu_r$, respectively. Clearly, in order to minimize spectral overlap, lineshape distortions and degraded signal-to-noise in MQMAS, it is desirable to spin the sample at the highest possible frequency.

The elimination of spinning sidebands in MQMAS spectra can also be achieved, in certain cases, by employing *rotor-synchronization*. Massiot has demonstrated that by setting the dwell time in the t_1 dimension equal to the inverse of the (scaled) spinning rate, sideband intensity and lineshape will be concentrated in the central peak (82). Three advantages of this variation can be identified. First, potential overlap between spinning sidebands and resonances from other sites is avoided. Second, better signal-to-noise is realized for each t_1 increment. Finally, the anisotropic subspectra obtained in the f_2 dimension will represent the "infinite spinning speed" lineshapes. The author illustrates these advantages with ^{27}Al 3QMAS of sillimanite (82). Without rotor-synchronized data acquisition, the 21-hour

experiment yielded 2D spectra littered with spinning sidebands, and subspectral slices poorly represented by the infinite spinning speed approximation. By contrast, spectra acquired with rotor-sychronization were obtained in 8 hours, and exhibit comparable signal-to-noise, sideband-free resonances and lineshapes that can be easily simulated. A notable limitation of this approach is that at currently attainable spinning frequencies, the sweep width, SW, in the f_1 dimension is constrained to be fairly small, due to its dependence on the dwell time, DW:

$$SW = \frac{1}{(1 + k)DW} .$$ (41)

This restriction may not accommodate the range of chemical shifts present in some samples.

Phase-Cycling. Crucial to any NMR experiment involving MQ coherences is some way of selecting particular pathways of interest to the exclusion of others. This is generally accomplished in MQMAS by phase-cycling, although pulsed field gradients have been shown to provide another means of coherence pathway selection (*83*). General descriptions of the underlying theory of phase-cycling are available (*84*) and its implementation in MQMAS is discussed by Massiot et al. (*72*). Here, it is sufficient to state that since each p-quantum coherence ($p = 2m_S$) has a characteristic transformation behaviour under rf phase shifts, carefully chosen phases of the consituent pulses will propagate into the observed $p = -1$ coherence and can be selected by an appropriate receiver phase.

A specific strategy involves the perfomance of N_i experiments with systematic phase increments, ϑ_i, to pulse i of

$$\vartheta_i = \frac{k_i(2\pi)}{N_i} \qquad k_i = 0, 1, \cdots, N_i - 1 .$$ (42)

Each of the N_i signals consists of a superposition of coherence orders which can be disentangled by a discrete Fourier analysis with respect to ϑ_i. The resulting weighted linear combination retains only contributions which have undergone a change in

coherence of Δp. This weighting can be achieved by phase-shifting all subsequent pulses in the sequence by

$$\vartheta = \Delta p_i \, \vartheta_i \qquad (43)$$

or by phase-shifting the receiver reference channel:

$$\vartheta^{\text{ref}} = -\Delta p_i \, \vartheta_i . \qquad (44)$$

Therefore, the phase of each pulse must be incremented in a manner appropriate to select the desired *change* in coherence order. The cyclic nature of the applied phases implies that an *aliasing* effect will be observed, demanding a sufficiently large number of experiments be carried out to eliminate all undesired pathways containing appreciable coherence:

$$\Delta p^{\text{(selected)}} = \Delta p^{\text{(desired)}} \pm n N_i . \qquad (45)$$

Accordingly, the original pulse sequence proposed by Frydman's group utilized a 12-phase cycle intended to select only the $0 \rightarrow -3 \rightarrow -1$ pathway (*29a*).

While this approach is adequate for obtaining 1D isotropic spectra, the corresponding 2D peaks will, in general, contain appreciable phase distortions arising from dispersion-mode lineshapes. Since a realization of the full potential of MQMAS involves the analysis of individual site subspectra in the anisotropic dimension of a 2D spectrum, it is advantageous to acquire pure-absorption phase spectra, free of dispersive character. Indeed, one of the first reported variations of the two-pulse sequence for MQMAS was a phase-cycling scheme designed do this (*75*). In fact, a variety of approaches have been developed to achieve this purpose, all of which require the selection of both echo and anti-echo pathways, $\pm$MQ, during the t_1 evolution period, such that the time-domain signal is *amplitude-modulated* rather than *phase-modulated* (*84*). These terms refer to the type of changes observed in the time-domain signal as a function of variations in t_1. Phase-modulated signals will be obtained in all cases where a single coherence pathway is chosen, and will invariably

lead to mixed-phase peaks upon Fourier transformation. Amplitude-modulated signals are created by the acquisition of two mirror-image pathways, which can be transformed in such a way as to produce pure-phase peaks (84).

The most straightforward way to obtain pure-phase 2D peaks in 3QMAS is to exploit the aliasing effect. If a six-phase cycle is used to select a triple-quantum pathway, the mirror image will also be selected, according to equation (45). Dispersive components are *completely* eliminated only when the coherence transferred into the observable $p = -1$ is equally intense from both MQ pathways. This is, in general, not the case, as Δp differs for $-p \rightarrow -1$ and $+p \rightarrow -1$. For spin-3/2 nuclei, however, it is possible to optimize the transfer pulse such that this condition is satisfied (76). Interestingly, simulations have shown that the pulse length needed to equalize the transfer from both pathways is approximately the "solution 90°", somewhat longer than that predicted to give the best signal-to-noise, 55° (76). Recombination and processing of the signals can be accomplished using time-proportional phase increments (TPPI) (75) or the hypercomplex method (72), for example.

The most general method for obtaining pure absorption-phase 2D MQMAS spectra appears to be the inclusion of a *z-filter* just prior to acquisition (85). Also first adapted for DAS, this technique is designed to symmetrize mirror image coherences by modifying the coherence pathways to pass through $p = 0$ before detection in $p = -1$. The first application of this method employed a two-pulse z-filter in combination with a delayed acquisition pulse sequence, in which no pulses were optimized (85). Moreover, the demonstration focussed on the spin-3/2 ^{23}Na, for which pure absorption-phase spectra can be obtained *without* a z-filter. Consequently, it is difficult to clearly see the advantages of this technique on the basis of this presentation.

Subsequently, a second report appeared, advocating the z-filter as a means of eliminating dispersion-mode lineshape contributions (86). Amoureux et al. offer a modified z-filter alleged to provide a better overall filtering function. They cite

(unpublished) computations which suggest the overall efficiency is comparable to the original unfiltered sequence, but that dispersive components are greatly reduced. The spectral improvements realized by this technique are exhibited using [27]Al 3QMAS of AlPO-14, in combination with rotor-synchronization. A comparison with the first publication of this spectrum (79) depicts dramatic lineshape improvements (86). Use of the z-filter promises to be of particular utility in MQMAS experiments of $S > 3/2$ nuclides, since no single transfer pulse is capable of equalizing the contributions of both coherence pathways for all crystallite orientations in the magnetic field (76).

Higher-Order Correlations. The foregoing discussion has concentrated on 3QMAS experiments because of their general utility for half-integer quadrupolar nuclei; however better resolution can be obtained by using the highest coherence order possible (87), due to the m_S-dependence of the isotropic chemical shift and $A_4(S,m_S)$ (equation (30)). The group of Amoureux and Fernandez has provided numerous examples of the improved site resolution realized via [27]Al 5QMAS of aluminophosphate molecular sieves (58,79,88). Experimentally, 5QMAS requires careful optimization of the pulse widths. Theoretical simulations suggest excitation and transfer maxima are observed at flip angles of 170° and 70°, respectively, for a reasonably realistic range of ν_Q/ν_{rf} (76). A ten-phase cycle can be used to simultaneously select the $\pm 5Q$ coherences during the t_1 evolution period (88) and presumably, the addition of a z-filter prior to acquisition will improve anisotropic lineshapes.

The price to be paid for the greater resolving power of higher-order MQMAS experiments is drastically diminished signal-to-noise. Calculations on the spin-5/2 system suggest that even under optimized conditions, signal intensities in 5QMAS will be less than 20% of that in an optimized 3QMAS experiment (76). RIACT may be able to improve this (80), but no report of its ability to interconvert 1Q and 5Q coherence has yet appeared.

Another complication in higher-order MQMAS is the aforementioned spinning sideband scaling problem. With the increase in k which results in improved

resolution also comes a more severe scaling of spinning sidebands (*vide supra*). In particular, on going from 3Q- to 5QMAS in a spin-5/2 system, k increases from 1.58 to 2.08 (equations (31) and (39)). Rotor-synchronization can probably be used to circumvent this problem, but the sweep-width restriction will be even more exacting (see equation (41)).

2.3 Coupling Phenomena

2.3.1 Direct Dipole-Dipole Interaction

That quadrupolar effects may influence the NMR lineshapes of dipolar-coupled spin-1/2 nuclei in solids is a well-known phenomenon (*37,89*). A natural question is whether similar effects will be incumbent upon the MQMAS peak positions of half-integer quadrupolar nuclei dipolar-coupled to spin-1/2 nuclei. The following demonstrates that in the regime for which MQMAS is effective – currently, for small ν_Q/ν_L – spectra will be free of distortions arising from incompletely averaged dipolar couplings.

Since the current success of MQMAS is limited to "moderate" quadrupolar interactions (i.e., $\nu_Q < 2$ MHz), first-order perturbation theory sufficiently describes its influence on the pure Zeeman states. The general approach will be to develop expressions for the quadrupole-perturbed Zeeman eigenstates, $|\varphi_i'\rangle$, from the pure Zeeman states $|\varphi_i\rangle$, where the indices, i, denote spin functions, (e.g., $|\varphi_1\rangle = |+5/2\rangle$, $|\varphi_2\rangle = |+3/2\rangle$, etc.). The transformation matrix, T,

$$
\begin{bmatrix}
|+5/2'\rangle \\
|+3/2'\rangle \\
|+1/2'\rangle \\
|-1/2'\rangle \\
|-3/2'\rangle \\
|-5/2'\rangle
\end{bmatrix}
= T
\begin{bmatrix}
|+5/2\rangle \\
|+3/2\rangle \\
|+1/2\rangle \\
|-1/2\rangle \\
|-3/2\rangle \\
|-5/2\rangle
\end{bmatrix}
\tag{46}
$$

$$
T = \sum_{i=1}^{2S+1} \sum_{j=1}^{2S+1} a_{ij}
\tag{47}
$$

which will accomplish this is generated by evaluating the coefficients,

$$a_{ij} = \frac{\langle \varphi_j | \mathcal{H}_Q | \varphi_i \rangle}{E_j - E_i} \tag{48}$$

where E_j are the unperturbed Zeeman energies,

$$E_j = \langle \varphi_j | \mathcal{H}_Z | \varphi_j \rangle . \tag{49}$$

In this context, the quadrupolar Hamiltonian can be understood as the sum of its secular and non-secular contributions, influencing only the diagonal and non-diagonal elements, respectively. Under the condition of axial symmetry ($\eta = 0$):

$$\mathcal{H}_Q = \frac{e^2 qQ}{4S(2S - 1)} \{ \tfrac{1}{2}(3\cos^2\theta - 1)[3\hat{S}_z^2 - \hat{S}^2]$$

$$+ \tfrac{3}{2}\sin\theta\cos\theta[\hat{S}_z(\hat{S}_+ + \hat{S}_-) + (\hat{S}_+ + \hat{S}_-)\hat{S}_z] \tag{50}$$

$$+ \tfrac{3}{4}\sin^2\theta(\hat{S}_+^2 + \hat{S}_-^2)\} .$$

The unperturbed Zeeman transitions are evaluated by differences between energy levels:

$$\mathcal{H}_Z = -\nu_L \hat{S}_z , \tag{51}$$

Employing these relations, T becomes:

$$T = \begin{bmatrix} 1 & -A\sqrt{5} & -B\sqrt{10} & 0 & 0 & 0 \\ +A\sqrt{5} & 1 & -A\sqrt{2} & -3B\sqrt{2} & 0 & 0 \\ +B\sqrt{10} & +A\sqrt{2} & 1 & 0 & -3B\sqrt{2} & 0 \\ 0 & +3B\sqrt{2} & 0 & 1 & +A\sqrt{2} & -B\sqrt{10} \\ 0 & 0 & +3B\sqrt{2} & -A\sqrt{2} & 1 & +A\sqrt{5} \\ 0 & 0 & 0 & +B\sqrt{10} & -A\sqrt{5} & 1 \end{bmatrix} \tag{52}$$

where

$$A = \left[\frac{3}{20}\right] \frac{C_Q}{\nu_L} \sin\theta \cos\theta \tag{53}$$

$$B = \left[\frac{3}{160}\right] \frac{C_Q}{\nu_L} \sin^2\theta \quad . \tag{54}$$

Applying T to the Zeeman eigenstates according to equation (46) gives the perturbed eigenstates:

$$|+5/2'\rangle = |+5/2\rangle - A\sqrt{5}\,|+3/2\rangle - B\sqrt{10}\,|+1/2\rangle$$

$$|+3/2'\rangle = A\sqrt{5}\,|+5/2\rangle + |+3/2\rangle - A\sqrt{2}\,|+1/2\rangle - 3B\sqrt{2}\,|-1/2\rangle$$

$$|+1/2'\rangle = B\sqrt{10}\,|+5/2\rangle + A\sqrt{2}\,|+3/2\rangle + |+1/2\rangle - 3B\sqrt{2}\,|-3/2\rangle$$

$$|-1/2'\rangle = 3B\sqrt{2}\,|+3/2\rangle + |-1/2\rangle + A\sqrt{2}\,|-3/2\rangle - B\sqrt{10}\,|-5/2\rangle \tag{55}$$

$$|-3/2'\rangle = 3B\sqrt{2}\,|+1/2\rangle - A\sqrt{2}\,|-1/2\rangle + |-3/2\rangle - A\sqrt{5}\,|-5/2\rangle$$

$$|-5/2'\rangle = B\sqrt{10}\,|-1/2\rangle - A\sqrt{5}\,|-3/2\rangle + |-5/2\rangle \quad .$$

Assuming the dipolar interaction is much smaller than the Zeeman-quadrupolar interaction (valid for high-field NMR), the dipolar energy shifts can now be determined as the diagonal elements, $\langle\varphi_i'|\mathcal{H}_D|\varphi_i'\rangle$, where

$$\mathcal{H}_D = -hR_{DD}[(3\cos^2\beta - 1)\hat{S}_z + \tfrac{3}{2}(\hat{S}_+ e^{-i\alpha} + \hat{S}_- e^{i\alpha})\sin\beta\cos\beta]\,\hat{I}_z \tag{56}$$

and (α, β) identify the orientation of r_{IS} in the laboratory frame of reference (Figure 1) and R_{DD} is defined in equation (24). The *raising* and *lowering operators* are related to the transverse components of the spin angular momentum:

$$\hat{S}_\pm = \hat{S}_x \pm i\hat{S}_y \quad . \tag{57}$$

The introduction of $\hat{S}_x$ and $\hat{S}_y$ with respect to the usual spin-1/2 dipolar Hamiltonian stems from the non-zero transverse component of S spin angular momentum. Again, the regime for which MQMAS is practicable renders second-order terms involving

C_Q^2/ν_L^2 negligibly small, and these are simply dropped in the expansion of the dipolar matrix.

This treatment results in a series of energy terms with a general form, for example:

$$\langle \pm 5/2' \,|\, h^{-1}\mathcal{H}_D \,|\, \pm 5/2' \rangle = -R_{DD} m_I [\tfrac{5}{2}(3\cos^2\beta - 1)$$

$$+ \tfrac{9}{4}\frac{C_Q}{\nu_L}(\cos\beta \,\sin\beta \,\cos\theta \,\sin\theta \,\cos\alpha)] \tag{58}$$

$$\langle \pm 3/2' \,|\, h^{-1}\mathcal{H}_D \,|\, \pm 3/2' \rangle = -R_{DD} m_I [\tfrac{3}{2}(3\cos^2\beta - 1)$$

$$- \tfrac{9}{20}\frac{C_Q}{\nu_L}(\cos\beta \,\sin\beta \,\cos\theta \,\sin\theta \,\cos\alpha)] \tag{59}$$

$$\langle \pm 1/2' \,|\, h^{-1}\mathcal{H}_D \,|\, \pm 1/2' \rangle = -R_{DD} m_I [\tfrac{1}{2}(3\cos^2\beta - 1)$$

$$- \tfrac{9}{5}\frac{C_Q}{\nu_L}(\cos\beta \,\sin\beta \,\cos\theta \,\sin\theta \,\cos\alpha)] \; . \tag{60}$$

Transition energies are easily obtained as differences between the appropriate energy levels, yielding the result that the symmetric $(m_S, -m_S)$ transitions involved in MQMAS are unaffected by terms involving the quadrupole coupling constant. In general, a symmetric transition will be split by

$$\Delta\nu(m_S, -m_S) = 2m_S R_{DD}(3\cos^2\beta - 1) \; . \tag{61}$$

Since this term possesses only the second-order Legendre polynomial, magic-angle spinning effectively averages its orientation dependence. Although higher-order corrections are expected to influence symmetric transitions other than the central transition (51), the extent of their influence is vanishingly small for the values of ν_Q for which MQMAS signals may be observed by current methodology. Therefore, it

can safely be concluded that MQMAS spectra will be free from "residual dipolar coupling" distortions.

A secondary conclusion of this exercise is that single-quantum satellite transitions *will*, in general, be affected by dipolar shifts due to quadrupolar effects. With reference to equations (58) – (60), the quadrupolar distortion terms for a given orientation will be of opposite sign for opposing transitions. For example,

$$
\Delta\nu(+3/2, +1/2) = R_{DD}(3\cos^2\beta - 1)
$$
$$
- \frac{27}{20} \frac{R_{DD} \, C_Q}{\nu_L} (\cos\beta \sin\beta \cos\theta \sin\theta \cos\alpha)
$$

(62)

$$
\Delta\nu(-1/2, -3/2) = R_{DD}(3\cos^2\beta - 1)
$$
$$
+ \frac{27}{20} \frac{R_{DD} \, C_Q}{\nu_L} (\cos\beta \sin\beta \cos\theta \sin\theta \cos\alpha)
$$

(63)

Thus, the zeroth-order dipolar splitting will be diminished for one satellite, and augmented for the other. The orientation dependence of this term dictates that it is zero for orientations with r_{IS} and/or V_{33} aligned parallel or perpendicular to the applied field. Because of this orientation dependence, these effects will be difficult to observe in MAS studies of powders, although they may result in asymmetric spinning sideband lineshapes for satellite transitions. The experimental observation of this phenomenon is more likely in single crystal samples, where opposing satellite transitions will be "squeezed" or "stretched" for certain orientations in the field. Such effects have been identified in ^{14}N NMR spectra of a single crystal of N-acetyl-D,L-valine (*50,90*). In fact, it is likely that asymmetric splittings have been observed in single-crystal NMR experiments of half-integer nuclei, although they may not have been recognized. For example, an oxygen-17 NMR study of an α-glycine crystal is reported to exhibit dipolar splittings to a neighbouring proton. A schematic diagram of a spectrum presented in the article possessed splittings which differed from one transition to the next. However, the authors give insufficient information to analyze this spectrum, and report that a full analysis will be "published elsewhere" (*91*).

2.3.2 Indirect Spin-Spin Interaction

Since the total evolution process of the echo consists of contributions from both MQ and 1Q coherences, the splittings in isotropic MQMAS spectra due to indirect spin-spin coupling are not simply the value of the heteronuclear J-coupling. With reference to equation (40), it is clear that for multiple peaks arising from J-coupling, the splitting will be the frequency difference between two "sites", the quadrupolar parameters of which are identical. Hence, the observed splitting, J_{MQ}, in isotropic MQMAS spectra is related to the heteronuclear J-coupling by the following equation (*30*):

$$J_{MQ} = a(S, m_S) J$$

$$= \left[\frac{k - 2m_S}{1 + k} \right] J \qquad (64)$$

Selected values of $a(S, m_S)$ are given in Table 3. It is interesting to note that J_{MQ} can be more than two times as large as J. For instance, the presence of a heteronuclear J will cause a splitting of $2.125J$ in isotropic 3QMAS spectra for $S = 3/2$ nuclei. This unique property of the MQMAS method, in addition to the removal of second-order quadrupolar broadening, further enhances the detection of relatively small J-couplings in solid materials. It can be seen in Table 3 that the scaling factor depends upon the MQ coherence chosen for the MQMAS experiment. More specifically, the largest splitting is found for the highest-order MQ coherence, $2S$, whereas for lower-order MQ coherences, J_{MQ} is smaller than J, except for the 7Q coherence in $S = 9/2$ systems. By implication, the most easily accessed MQMAS experiment for $S > 3/2$ will yield *reduced* splittings in the isotropic dimension due to J-coupling. On paper, the answer is to employ the highest-order MQ coherence to average quadrupolar anisotropy; however, it should be noted that these experiments are difficult to perform due to low sensitivity and sharp optimal pulse conditions. For example, 5QMAS has been reported only for the 100% naturally abundant [27]Al ($S = 5/2$) (*57,58,79,87,88,92*). Other authors report an inability to observe 5QMAS in [59]Co

$(S = 7/2)$ (93) which is also naturally present in 100% abundance. Finally, even working at the highest magnetic fields $(B_0 = 17.6$ T$)$, highest available rf fields, and fastest spinning rates $(\nu_r > 30$ kHz$)$, signals from 7Q and 9Q MAS of ^{93}Nb $(S = 9/2)$ remain elusive (94).

Table 3   Selected values of $a(S, m_S)$, calculated from equation (64)

S	$2m_S$			
	3Q	5Q	7Q	9Q
3/2	+17/8	—	—	—
5/2	-17/31	+85/37	—	—
7/2	-17/73	-85/50	+238/103	—
9/2	-17/127	-85/131	-238/50	+85/37

2.4 Experimental Examples

2.4.1 Borane-Triphenylphosphite

As a preliminary test of the foregoing predictions, a 1:1 borane-triphenylphosphite adduct was examined by ^{11}B 3QMAS (30). This sample was selected because it is commerically available, and because values of $^1J(^{31}P,^{11}B)$ are known from solution NMR of related compounds to be relatively large, ranging from 80 to 100 Hz (95). Moreover, typical values of $C_Q(^{11}B)$ lie between 1.0 and 3.5 MHz (96), directly in the region for which MQMAS is well-suited.

Experimental

Solid-state NMR spectra were recorded on NMR spectrometers operating at 7.4 and 9.4 T. (Spectra at 7.4 T were acquired by Dr. Gang Wu at the Francis Bitter Magnet Laboratory, Massachusetts Institute of Technology.) The rf field strength at the ^{11}B frequency was between 80 and 119 kHz. Borane-triphenylphosphite, $(PhO)_3P\text{-}BH_3$, was obtained from Aldrich Chemical Company, Inc. and used without further recrystallization (melting range: 49-50°C). The reported ^{11}B chemical shift is referenced to solid $NaBH_4$. A single excitation pulse of 6.0 to 8.0 μs and a 2.0 to 3.0 μs coherence transfer pulse were used in obtaining ^{11}B isotropic 3QMAS spectra. Phase cycling was used to select the $0 \rightarrow -3 \rightarrow -1$ coherence pathway. Proton decoupling was employed during both evolution and detection periods with a typical decoupling power of 70-90 kHz.

Results and Discussion

The experimental ^{11}B MAS spectrum of $(PhO)_3P\text{-}BH_3$ obtained at 7.4 T is shown in Figure 3. The major features of the lineshape are due to the second-order quadrupole interaction, with more subtle steps and shoulders suggesting the presence of $^1J(^{11}B,^{31}P)$. Clearly, the second-order quadrupolar lineshape in the ^{11}B MAS spectrum makes the observation of $^1J(^{11}B,^{31}P)$ difficult, while J-coupling to ^{31}P interferes with a lineshape calculation to obtain the ^{11}B quadrupole parameters. In

contrast, the ^{11}B isotropic 3QMAS spectrum of $(PhO)_3P\text{-}BH_3$ observed at 7.4 T (Figure 4) exhibits a doublet with a splitting of 180 ± 10 Hz. According to equation (64), this separation corresponds to $^1J(^{11}B,^{31}P)$ = 85 ± 5 Hz. The linewidth of the peaks in the isotropic ^{11}B 3QMAS spectrum is 150 Hz, much smaller than that found in the MAS spectrum, 800 Hz. In principle, the observed doublet could also arise from the presence of two crystallographically distinct ^{11}B sites exhibiting identical quadrupole couplings, but different chemical shifts. Since the crystal structure of this complex does not appear to be available in the literature, this ambiguity was resolved by performing ^{11}B 3QMAS at a second field. Isotropic ^{11}B 3QMAS spectra obtained at 9.4 T exhibit a doublet with the same splitting as observed at 7.4 T, confirming that the doublet does indeed arise from indirect spin-spin coupling to ^{31}P. Knowing $^1J(^{11}B,^{31}P)$, the ^{11}B MAS spectra obtained at both fields may be analysed, confirming the presence of $^1J(^{11}B,^{31}P)$ and yielding the following parameters: $|C_Q|$ = 1.22 ± 0.02 MHz, η = 0.10 ± 0.05, δ_{iso} = 3.0 ± 0.1 ppm, and $|^1J(^{11}B,^{31}P)|$ = 85 ±5 Hz. (Figure 3). The ^{11}B quadrupole parameters obtained for $(PhO)_3P\text{-}BH_3$ are very similar to those of borane-triphenylphosphine complex, $Ph_3P\text{-}BH_3$ (97). The value of $^1J(^{11}B,^{31}P)$ is also consistent with results from previous solution NMR studies of related compounds (98). On the basis of these experiments, it may be safely concluded that the splitting in ^{11}B 3QMAS spectra of solid borane-triphenylphosphite can be accounted for only by $^1J(^{11}B,^{31}P)$.

In spite of satisfactory ^{11}B NMR results for $(PhO)_3P\text{-}BH_3$, this complex may not have been the best choice for testing the theory presented above. For example, ignorance of the crystal structure introduces uncertainty which, while not critical when NMR can be performed at multiple fields, may appear to undermine claims about the origin of observed 3QMAS peaks. More importantly, the sample purity, as received from Aldrich, may have been compromised, appearing as an orange-yellow solid. Attempts to recrystallize the material resulted in white solids that were not easily dried. Related to this, the compound melts over the range 49 – 50°C, (Aldrich cites a melting range of 49 – 51°C) suggestive of impurities. Whereas this low

melting point influences the ease with which the compound may be recrystallized, it also has implications for the sample integrity at the elevated temperatures of rapid magic-angle spinning experiments. Finally, the presence of nearly 20% naturally abundant ^{10}B nuclei represents additional complications in the ^{31}P NMR spectra. A spin-3 nuclide, boron-10 has a nuclear quadrupole moment greater than twice that of ^{11}B, and its magnetogyric ratio is about one-third $\gamma(^{11}B)$, thereby producing very different coupling effects than boron-11. A better candidate for testing this theory would be structurally well-characterized, crystalline and pure. Ideally, the value of J obtained from MQMAS should be independently assessed from the MAS spectrum of its coupling partner. The following section is devoted to such a system.

(a)

(b)

(c)

0.8   0.4   0.0   -0.4   -0.8

kHz
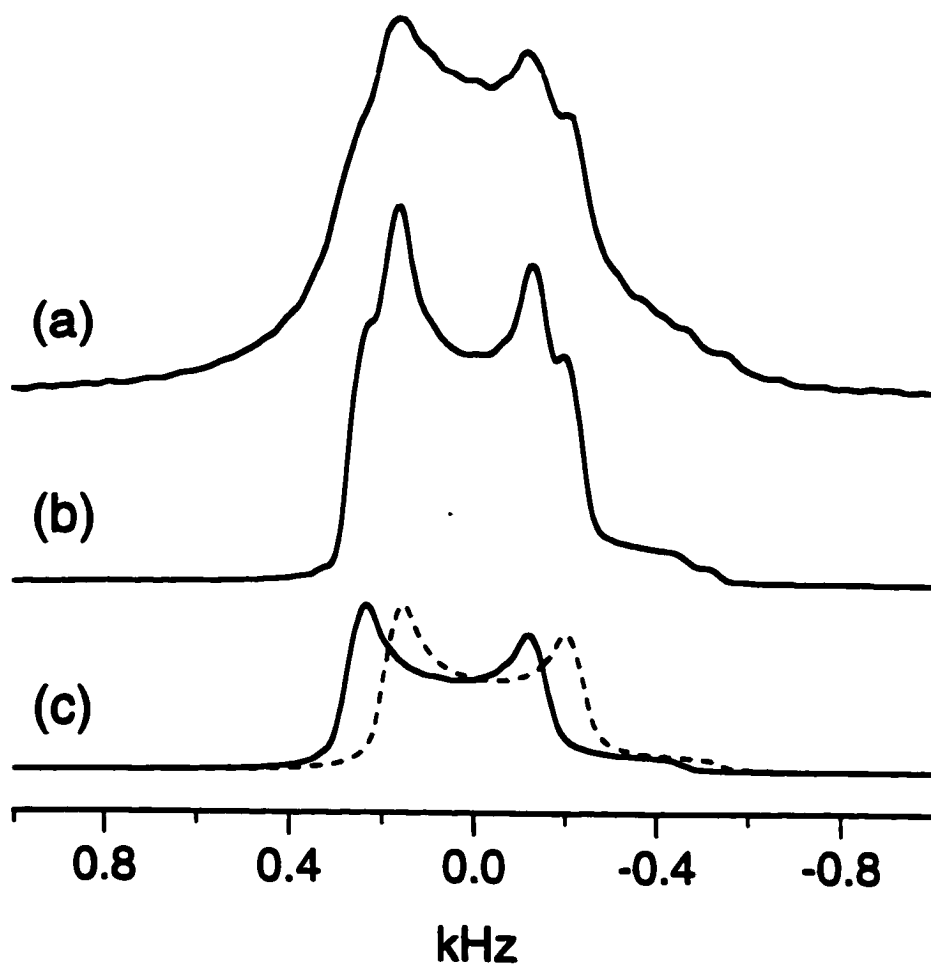
Figure 3   Boron-11 MAS spectra of $(PhO)_3P-BH_3$ obtained at 7.4 T; (a)
experimental, (b) simulated and (c) simulated subspectra. See text for
the parameters used in the simulation.

2.125J

(a)

(b)

2.0   1.0   0.0   -1.0   -2.0

kHz
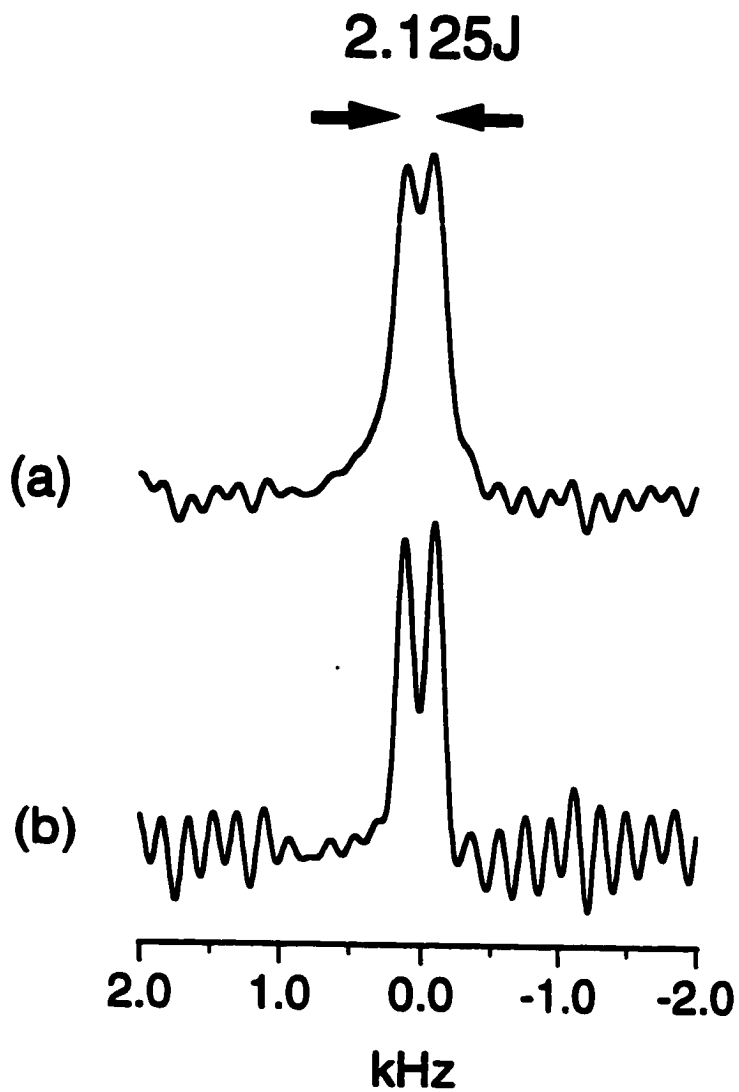
Figure 4   Boron-11 3QMAS spectra of $(PhO)_3P-BH_3$ obtained at 7.4 T; (a) without and (b) with resolution enhancement. A total of 128 t_1 increments were collected with 144 transients for each. The recycle delay was 2 s and the sample spinning speed, 8.20 kHz.

2.4.2 Tripotassium Tetracyanocuprate

Simple inorganic salts containing cyanide ligands complexed to copper(I) are known to combine in a variety of ratios, displaying diverse structural characteristics. Potassium dicyanocuprate, for example, comprises spiralling polymer chains of composition $[Cu(CN)_2^-]_\infty$ (99) and $KCu_2(CN)_3 \cdot H_2O$ forms two-dimensional sheets involving $[Cu_2(CN)_3^-]_\infty$ (100). By contrast, $K_3Cu(CN)_4$ consists of discrete $Cu(CN)_4^{3-}$ tetrahedra (101). In terms of copper coordination, the one-to-one complex, CuCN, contains two-coordinate copper atoms (see section 3.2.2), whereas both $KCu(CN)_2$ and $KCu_2(CN)_3 \cdot H_2O$ possess copper centres bound to three cyanide ligands in a nearly trigonal-planar arrangement, and $K_3Cu(CN)_4$ includes four copper-carbon linkages. Given this diversity, these systems serve as excellent model compounds for studying geometric effects on the ^{13}C and ^{15}N NMR parameters.

In addition to their attractiveness as well-characterized model compounds, the chemistry of cyanometallates, in general, is becoming a popular means of constructing supramolecular assemblies (102). The particular utility of tetracyanocuprate tetrahedra as building blocks has been highlighted in a recent review (103). Since then, at least two related reports have appeared. The reaction of $K_3Cu(CN)_4$ with Me_3SnCl and 4,4'-bipyridine (bpy) produces a porous structure of $[Cu_2(\mu-CN)_2(CN)_2]$ sheets bridged by bpy "pillars" (104). One- and two-dimensional materials result from hydrothermal reactions of CuCN and $Cu(NO_3)_2 \cdot 2.5H_2O$ with organonitrogen ligands (105).

Toward the development of a more systematic understanding of NMR parameters in cyanocuprates, a comprehensive investigation of tripotassium tetracyanocuprate, $K_3Cu(CN)_4$ has been undertaken. The crystal structure of this compound consists of distorted tetrahedral $Cu(CN)_4^{3-}$ units, with a C_3 rotation axis along the distinct Cu-C-N bonds (101). This structural arrangement constrains the $^{63/65}Cu$ electric field gradient to be axially symmetric, with the largest component directed along the rotation axis. With this knowledge, lineshape calculations of the NMR spectra are simplified. Moreover, relatively high symmetry at the copper

centre makes it possible to directly probe the metal using copper-63/65 NMR.

Both naturally abundant copper isotopes, ^{63}Cu and ^{65}Cu, are spin-3/2 nuclei. They have sizeable quadrupole moments, and consequently their powder NMR spectra are observed only when the nucleus is situated in a symmetrical environment where the EFG is small. There are a number of reports of copper NMR in solutions (106), but fewer in solid samples. In spite of the inherent challenges of copper NMR, interesting experiments have been successfully performed on systems ranging from simple cubic ionic solids (107) to high-T_c cuprate superconductors (108). Of particular relevance to the present work, copper-63/65 NMR has been used to probe cyanide ordering in the host/guest framework compounds "N(CH$_3$)$_4$CuM(CN)$_4 \cdot$G", where M = Zn, Cd, Pt and G = CCl$_4$, CHCl$_3$, CH$_3$CCl$_3$ and CHBr$_3$ (109). A principal objective of that study was to unambiguously identify Cu–C–N–Zn connectivities in N(CH$_3$)$_4$CuZn(CN)$_4$ by NMR of both copper-63/65 and carbon-13 (109a). For that compound, copper atoms exist in perfectly tetrahedral environments, rendering the EFG at that site zero, and its lineshape isotropic. Less definitive were copper-63 NMR studies of some of the other compounds, where second-order quadrupolar lineshapes compromised site distinction (109b). The work presented in this thesis concerns a cyanocuprate of *known* structure, which may be used to assess the sensitivity of C_Q to deviations from cubic symmetry. Moreover, K$_3$Cu(CN)$_4$ is an ideal model for evaluating the feasibility of 3QMAS investigations involving nearly tetrahedral copper centres.

Experimental

Materials. Tripotassium tetracyanocuprate was prepared by addition of CuCN to an aqueous solution containing a stoichiometric excess of KCN. Small crystals formed as the water evaporated. Isotopically enriched samples were prepared using an appropriate ratio of ^{13}C-, ^{15}N- or ^{13}C^{15}N-enriched and natural abundance KCN. The resulting solids were characterized by Raman spectroscopy, using the well-documented cyanide stretching frequency as a means to establish chemical identity and purity (*110*). Some difficulties were encountered in obtaining K$_3$Cu(CN)$_4$ crystals free from KCu(CN)$_2$ and KCu$_2$(CN)$_3 \cdot$H$_2$O. Repeated recrystallization resulted in a mixture of K$_3$Cu(CN)$_4$ and KCu(CN)$_2$ estimated to be 4:1. Although the copper quadrupole coupling constant in the latter compound is too large to be observed in the copper-63/65 NMR spectra (*111,112*), its presence interfered with the carbon-13 and nitrogen-15 NMR spectra. This problem was eventually resolved by subtracting the MAS NMR spectra of nearly pure KCu(CN)$_2$ from those of impure K$_3$Cu(CN)$_4$.

NMR Spectroscopy. Spectra were acquired using Bruker spectrometers and probes: an MSL-200 operating at 4.7 T with a 7 mm double-bearing MAS probe and an AMX-400 at 9.4 T with a 4 mm double-bearing triple-resonance MAS probe. Carbon-13 and nitrogen-15 NMR spectra were acquired using single pulse excitation, with 60° pulses and recycle delays of 90 seconds or longer, due to long spin-lattice relaxation times. Carbon-13 chemical shifts are referenced with respect to TMS using solid adamantane as a secondary reference. Nitrogen-15 chemical shifts are reported with respect to liquid ammonia, referenced using solid ^{15}NH$_4$NO$_3$, which has a shift of +23.80 ppm relative to liquid ammonia at 20°C. In order to establish meaningful comparisons between experimental and calculated MAS lineshapes, it is necessary to construct an "isotropic MAS powder spectrum" by adding the spinning sidebands (ssbs) to the centreband (*113*).

Copper-63/65 single pulse MAS spectra were collected using "solid 90°" pulses for the central transition and very short pulses for the satellite transitions. Triple-quantum MAS spectra utilized a 167 kHz rf field, a multiple-quantum excitation pulse of 4 μs and a coherence transfer pulse of 1.2 μs. A 24-phase cycle

designed to simultaneously select the echo and anti-echo coherence pathways was employed. Copper-63/65 chemical shifts are referenced to an aqueous solution containing KCN/NaCN/CuCN corresponding to a CN:Cu molar ratio of about six, as described in reference (*114*). The copper chemical shift of this system is reported to be -494 ppm with respect to 1.0 M $[Cu(NCCH_3)_4][BF_4]$ in acetonitrile (*115*).

Lineshape Simulations. Spectral calculations were carried out using programs developed in this laboratory over many years. WSolids features a user-friendly Windows interface designed to compute frequency-domain NMR lineshapes resulting from the influence of a variety of spin interactions. Although some of the elements have been in the lab for many years, the packaging and testing has been done by Dr. Klaus Eichele. Of particular relevance to this work, modules exist to calculate: (a) central transition MAS spectra of quadrupolar nuclei spin-spin coupled to another nucleus; (b) stationary spectra of quadrupolar nuclei subject to anisotropic quadrupolar and chemical shielding tensors with a general orientation; (c) MAS spectra of spin-1/2 nuclei coupled to a quadrupolar nucleus, including residual dipolar effects calculated by first-order perturbation theory (any η) or by full-matrix diagonalization ($\eta = 0$); (d) stationary spin-1/2 NMR spectra dipolar-coupled to a second nucleus, neglecting quadrupolar perturbations. All MAS routines calculate the "infinite spinning speed" lineshape. QUADSPIN possesses all of the above in a decidedly user-*unfriendly* form. Programmed mainly by me (with invaluable assistance from Dr. Eichele), QUADSPIN also includes extensions of the models described above, notably: (a) the inclusion of spin-3/2 quadrupolar effects in stationary spin-1/2 spectra by first-order perturbation theory (any η) or by full-matrix diagonalization ($\eta = 0$); (b) a time-domain calculation of an isolated quadrupolar nucleus evolving under the influence of both anisotropic shielding and first-order quadrupolar effects, subject to sample rotation at any speed and any angle with respect to B_0. Essential to both programs is the POWDER algorithm of Alderman, Solum and Grant (*116*), which provides an efficient means to simulating a *powder pattern* for which all possible crystallite orientations must be considered.

Results and Discussion

  Copper NMR. Copper-63/65 MAS NMR spectra of the central transition of $K_3Cu(CN)_4$ in natural elemental abundance are shown in Figure 5 and Figure 6, along with the best-fit calculations. A single copper site with an isotropic chemical shift of -49 ppm (corrected for second-order quadrupolar effects) is observed by NMR, consistent with the crystal structure (*101*). Also in agreement with the crystal structure is the presence of an axially symmetric electric field gradient at the copper nucleus, manifesting in a lineshape which is characteristic of second-order quadrupolar anisotropy. The space group determined for this compound includes a C_3 axis along one of the Cu–CN bonds, with slight structural differences between this and the other bound cyanides amounting to only 2 pm in the Cu–C length, and 0.5° in the C–Cu–C angles, for example (*101*). This minor distortion from tetrahedral symmetry, however, is sufficient to induce a substantial quadrupole coupling constant of magnitude 1.125 ± 0.010 MHz for ^{63}Cu and 1.040 ± 0.010 MHz for ^{65}Cu, a testimony to the extreme sensitivity of copper C_Qs to molecular symmetry. This deviation from pure tetrahedral symmetry is also evident from its significant piezoelectric (*117*) and pyroelectric effects (*118*). In fact, the copper EFG tensor in this compound was first determined in 1951 by Becker (*119*), who analyzed the orientation-dependence of a 3.5 cm long by 1.4 cm diameter cylindrical crystal in a 1.1 T magnetic field. The author reports quadrupole coupling constants of 1.113 ± 0.003 MHz and 1.030 ± 0.003 MHz for the two isotopes. The difference between values obtained in the present study and those of the previous study is not *statistically significant*; however, if it does suggest a true difference, it may reside in Becker's failure to account for anisotropic chemical shielding. These effects would be very small at such a low applied field (~500 kHz), but could skew the analysis subtly. The ratio of the quadrupole coupling constants in both studies agrees with that anticipated on the basis of the quadrupole moments: $Q(^{63}Cu)/Q(^{65}Cu) = 1.081$.

  Copper-63/65 NMR spectra of the central transition in a non-spinning sample of $K_3Cu(CN)_4$ were also acquired at 4.7 and 9.4 T. Figure 7 and Figure 8 contain
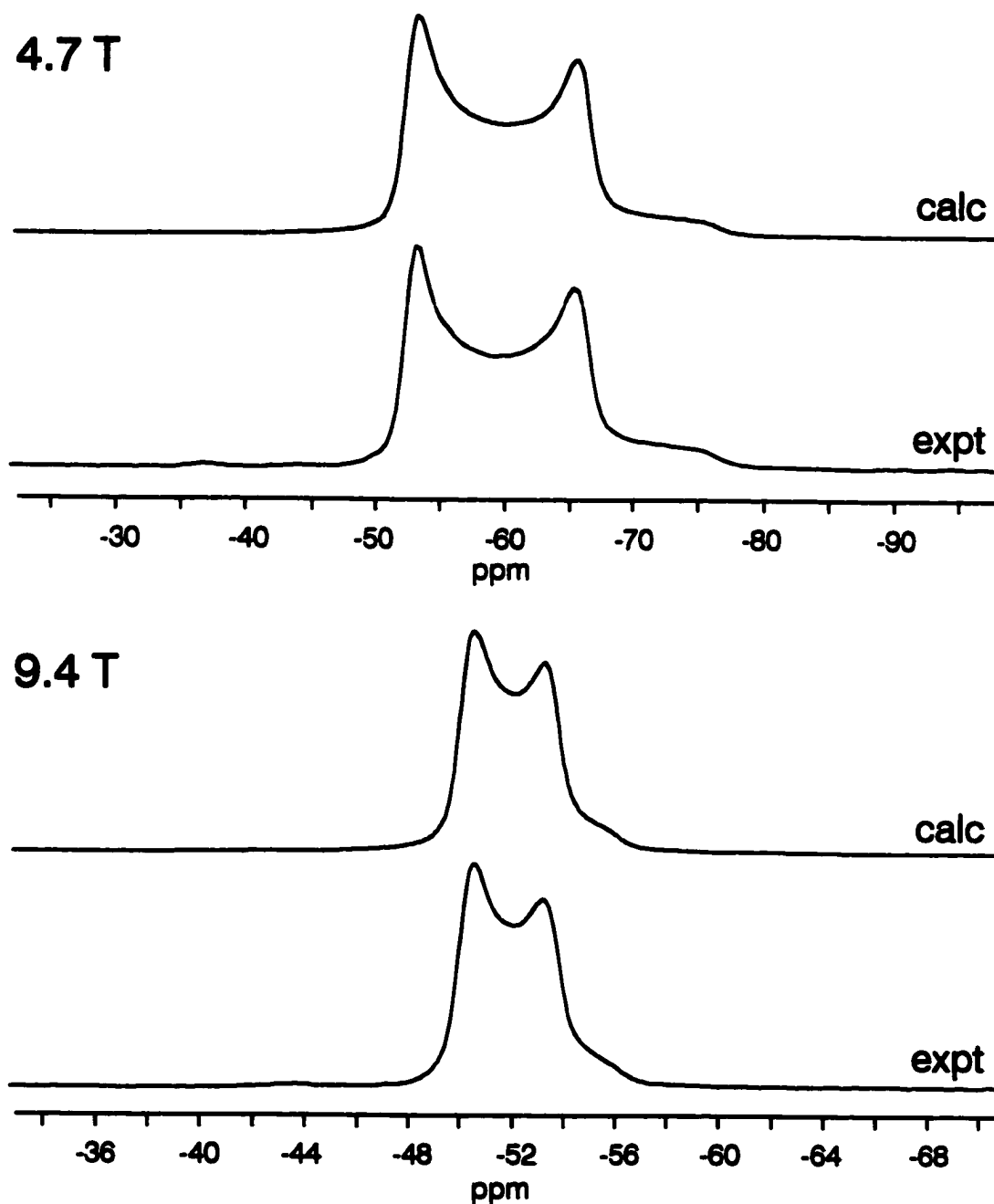
Figure 5   Copper-63 MAS NMR spectra of $K_3Cu(CN)_4$ in natural abundance at
4.7 and 9.4 T. Experimental spectra are the result of 1000 transients at
a sample spinning frequency of 6.45 kHz (4.7 T) and 128 transients at
8.00 kHz (9.4 T). Displayed regions at both fields span 4 kHz.
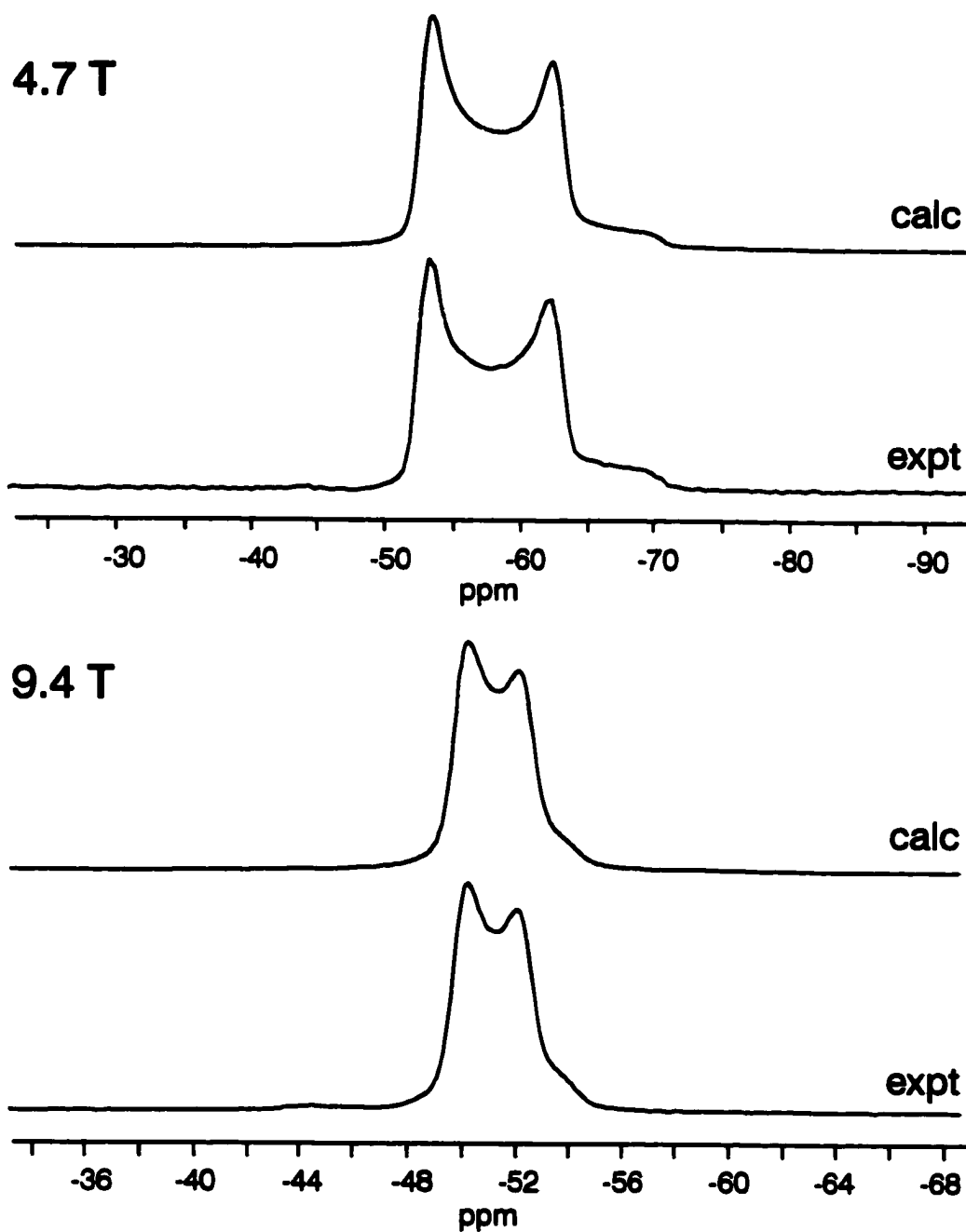
Figure 6   Copper-65 MAS NMR spectra of $K_3Cu(CN)_4$ in natural abundance at 4.7 and 9.4 T. Experimental spectra are the result of 1000 transients at a sample spinning frequency of 6.50 kHz (4.7 T) and 256 transients at 10.00 kHz (9.4 T). Displayed regions at both fields span 4 kHz.
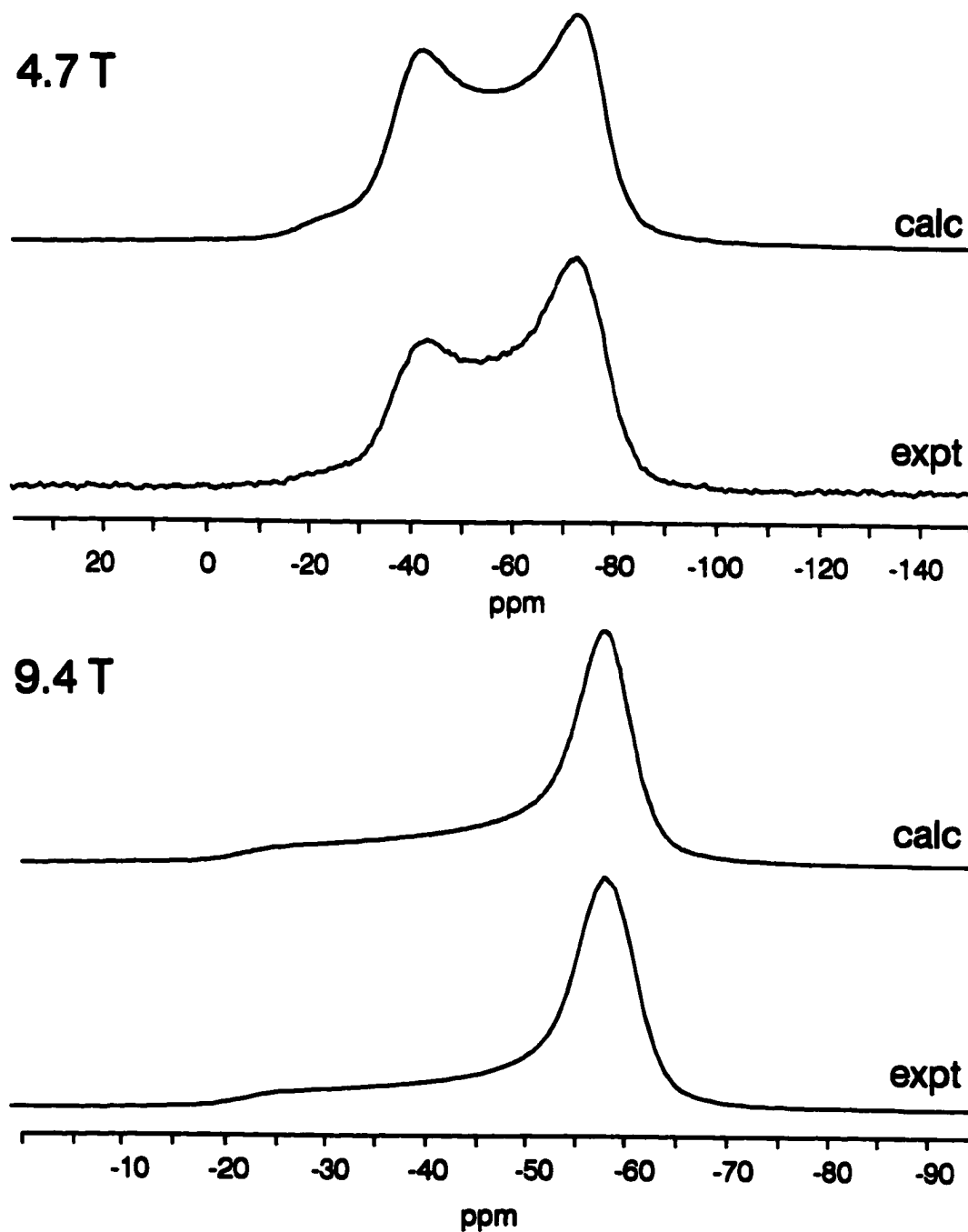
Figure 7   Copper-63 NMR spectra of non-spinning $K_3Cu(CN)_4$ powder in natural elemental abundance. The experimental spectrum at 4.7 T represents the coaddition of 500 transients, whereas at 9.4 T, 15787 transients were acquired. Displayed regions in all spectra span 10 kHz.
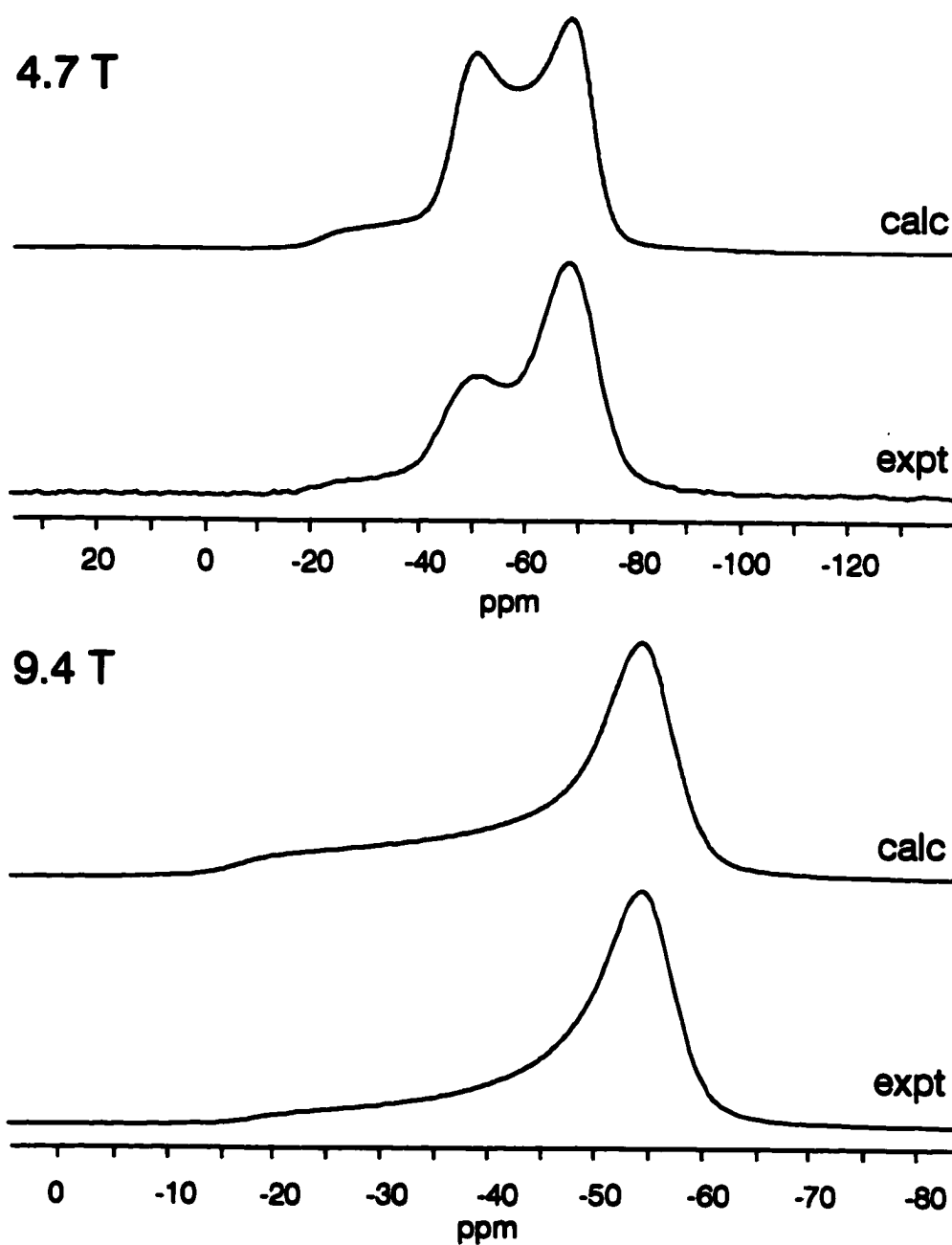
Figure 8   Copper-65 NMR spectra of non-spinning $K_3Cu(CN)_4$ powder in natural elemental abundance. The experimental spectra represent 1300 and 1659 transients for 4.7 and 9.4 T, respectively. Displayed regions in all spectra span 10 kHz.

the experimental spectra along with the best-fit calculations, incorporating, in addition to the quadrupolar interaction as determined by MAS NMR, effects due to anisotropic chemical shielding (Table 4). In these analyses, full advantage is taken of the molecular three-fold rotational symmetry in identifying the mutual EFG and shielding tensor orientation. The presence of a C_3 axis demands that the unique component of the axially symmetric interaction tensors be aligned with the rotation axis. Because the EFG tensor is traceless, the largest component is unique; its orientation in the molecular frame is fixed. For the shielding, however, the unique component may be the most- or least-shielded element, corresponding to $\kappa = +1$ or -1, respectively (see equation (12)). If $\kappa = +1$, the EFG and shielding tensors are coincident, whereas if $\kappa = -1$, V_{33} and δ_{11} are aligned with the rotation axis. The choice between these possibilities is straightforward based on the observed lineshapes (120). It is found that the copper shielding tensor spans 42(1) ppm, the least shielded component lying parallel to V_{33}. This is depicted in Figure 9 and Figure 10, along with a schematic of the two interactions under consideration. Also apparent from these diagrams is the opposite field dependence of the quadrupolar and chemical shielding interactions. At 4.7 T, quadrupolar effects are marginally more prominent, whereas at 9.4 T, anisotropic shielding clearly dominates the lineshape. This differing field dependence implies that reliable characterizations of shielding and EFG tensors are aided by collecting and analyzing spectra at multiple magnetic fields – especially when tensor orientations are not fixed by crystal symmetry. Moreover, it is likely that shielding tensors of quadrupolar nuclei will be more frequently reported in the literature, as the field strength available for NMR continues to increase.

In spite of generally good agreement between the calculated and experimental spectra, an obvious discrepancy is observed in the intensities of the 4.7 T spectra. A likely explanation involves consideration of weak dipolar interactions between copper nuclei and surrounding ^{14}N nuclei. Two-bond J-couplings are 14 Hz (vide infra), and dipolar couplings are calculated from the internuclear separation to be about 75 Hz. Although these constants are small in comparison with the quadrupolar and shielding
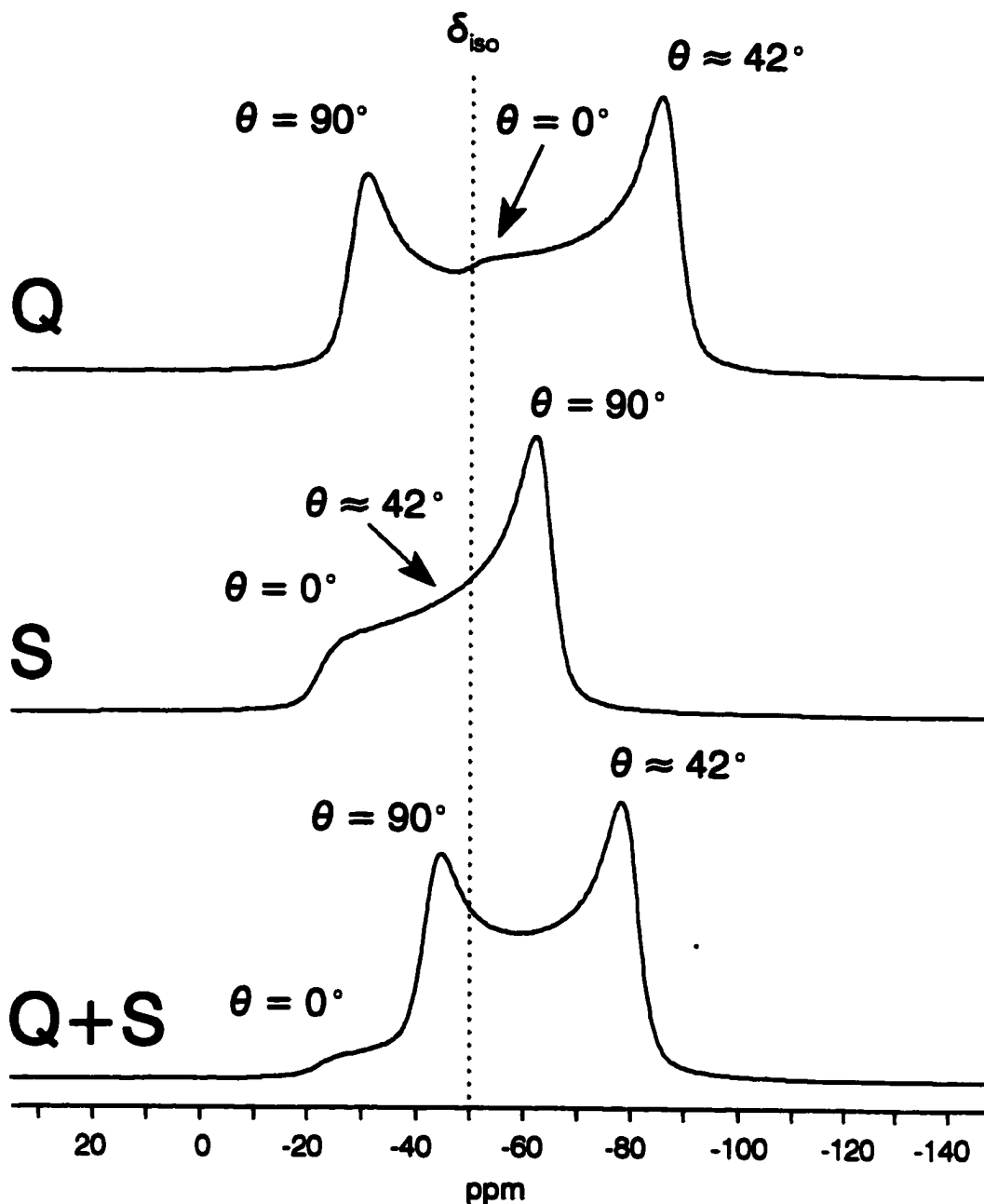
Figure 9 NMR lineshape simulations for "copper-63 at 4.7 T" in non-spinning $K_3Cu(CN)_4$, depicting the orientation dependence of the two dominant internal interactions: quadrupolar (Q), shielding (S) and their combined effect (Q + S). The Larmor frequency is 53.10 MHz, corresponding to ^{63}Cu at 4.7 T (see Figure 5). The orientation of the unique tensor component with respect to the applied magnetic field direction is indicated by θ for selected spectral features. The isotropic chemical shift is denoted by the dotted vertical line.
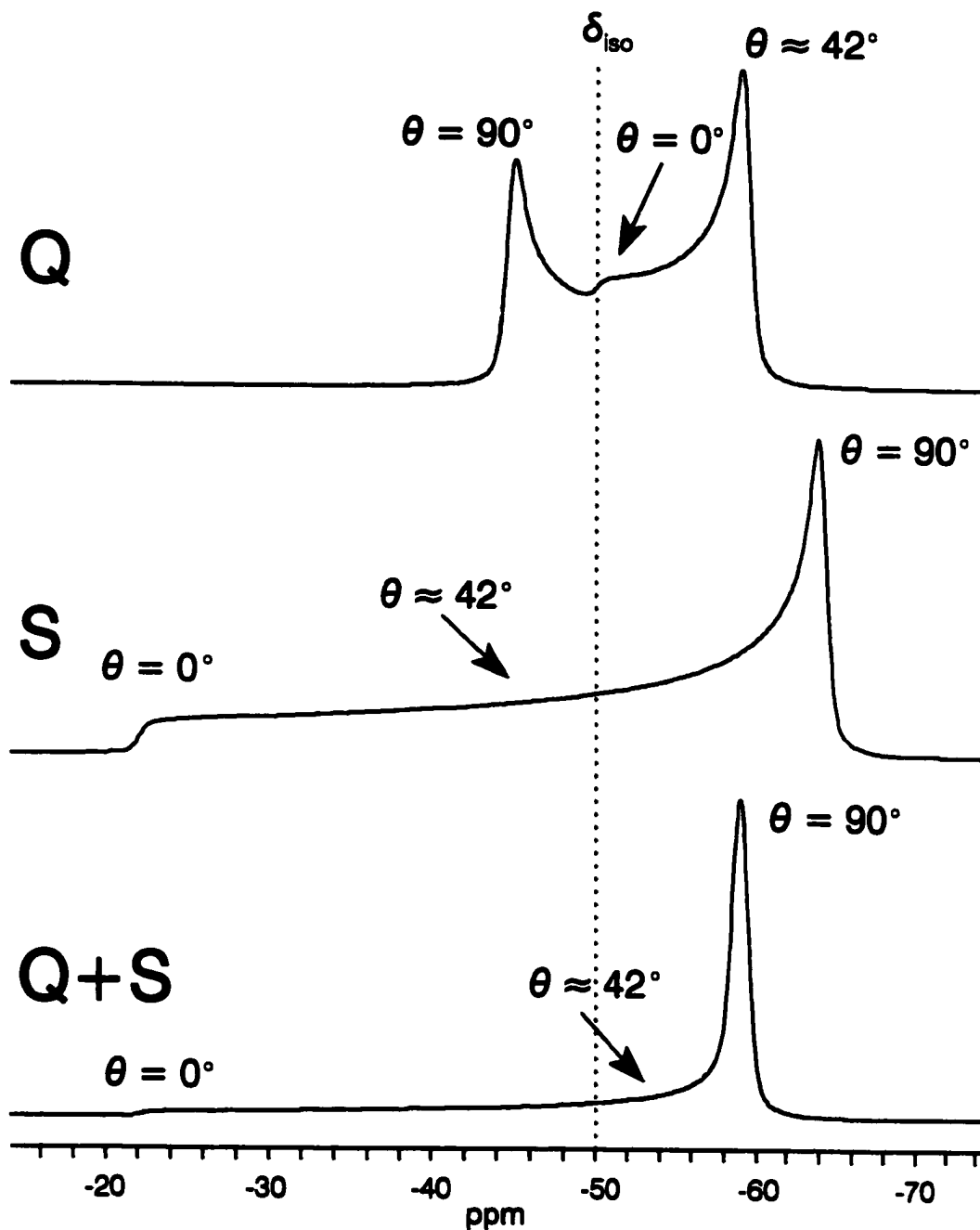
Figure 10   NMR lineshape simulations for "copper-63 at 9.4 T" in non-spinning $K_3Cu(CN)_4$ depicting the orientation dependence of the two dominant internal interactions: quadrupolar (Q), shielding (S) and their combined effect (Q + S). The Larmor frequency is 106.05 MHz, corresponding to ^{63}Cu at 9.4 T (see Figure 5). The orientation of the unique tensor component with respect to the field direction is indicated by θ for selected spectral features. The isotropic chemical shift is denoted by the dotted vertical line.

Table 4 Nuclear magnetic resonance data for $K_3Cu(CN)_4$

		δ_{iso}/ppm[a]	$\delta_\perp$/ppm[b]	$\delta_\parallel$/ppm[b]	$J(^{63}Cu,X)$/Hz[e]	C_Q/MHz[f]
^{13}C	1	161.4	275[c]	-65[d]	300 ± 2	—
	2	162.4			298 ± 2	—
^{15}N	1	282.5	450[c]	-45[d]	19 ± 1	—
	2	288.5			20 ± 1	—
^{63}Cu		-49 ± 1	-63 ± 1	-21 ± 1	—	-1.125
^{65}Cu		-49 ± 1	-63 ± 1	-21 ± 1	—	-1.040

[a] from MAS NMR spectra, estimated uncertainty ± 0.2 ppm, except where noted

[b] from NMR spectra of non-spinning samples, estimated uncertainty ± 5 ppm, except where noted

[c] individual sites not resolved

[d] not observed; value calculated from δ_{iso} and $\delta_\perp$

[e] from MAS NMR spectra of spin-1/2 nuclei

[f] magnitude from $^{63/65}Cu$ MAS NMR, sign from ^{13}C MAS NMR spectra, estimated uncertainty ± 0.010 MHz

interactions, their effects will be magnified by two factors. First, ^{14}N has a spin angular momentum quantum number of 1, so the copper signal will be split into three subspectra. Second, the high natural abundance of ^{14}N (99.63%) implies that each copper centre will be coupled to four nitrogen-14 nuclei. As a first approximation, these effects may result in nearly one kHz of additional broadening. More importantly, however, the splitting due to dipolar coupling depends on the orientation of $r_{Cu,N}$ with respect to the applied magnetic field. Ignoring the quadrupolar nature of ^{14}N, the magnitude of the dipolar splitting varies as $(1/2)R_{DD}(3cos\theta^2 - 1)$. Thus, for crystallite orientations where the rotation axis is parallel to the field direction ($\theta = 0$), three chemically equivalent ^{14}N nuclei will be situated with $\beta \approx 70°$, and the dipolar splitting will be scaled by -0.3. By contrast, for $\theta = 90°$, the three ^{14}N nuclei will be nearly aligned with the field, $\beta \approx 20°$, and the scaling of R_{DD} will be minimal, 0.85. The low frequency feature represents orientations with V_{33} and δ_{11} at 42°, for which the other three ^{14}N nuclei will have β ranging from 30 to 70°, bracketing the magic angle, where R_{DD} is scaled to zero. Of course, these "splittings" are too small to be observed, but their net effect is a broadening which will be more effective for some orientations than others. With reference to Figure 7 and Figure 8, greater broadening at the singularity corresponding to $\theta = 90°$ may manifest as an *apparent loss* of signal intensity with respect to the singularity at $\theta = 42°$, where less dipolar "broadening" will result in an apparent augmentation of the intensity.

Another approach to the characterization of EFG and chemical shielding tensors in solids is satellite transition spectroscopy (SATRAS). Originally proposed as a more precise measurement of C_Q and η than central transition lineshape modelling (121), this technique has developed into a valuable means for obtaining detailed information about the magnitudes *and* relative orientation of shielding and EFG tensors (18). Figure 11 and Figure 12 depict the spinning sideband manifold for the copper-63 and copper-65 satellite transitions, along with simulations based on the parameters given in Table 4. A number of considerations, both experimental and
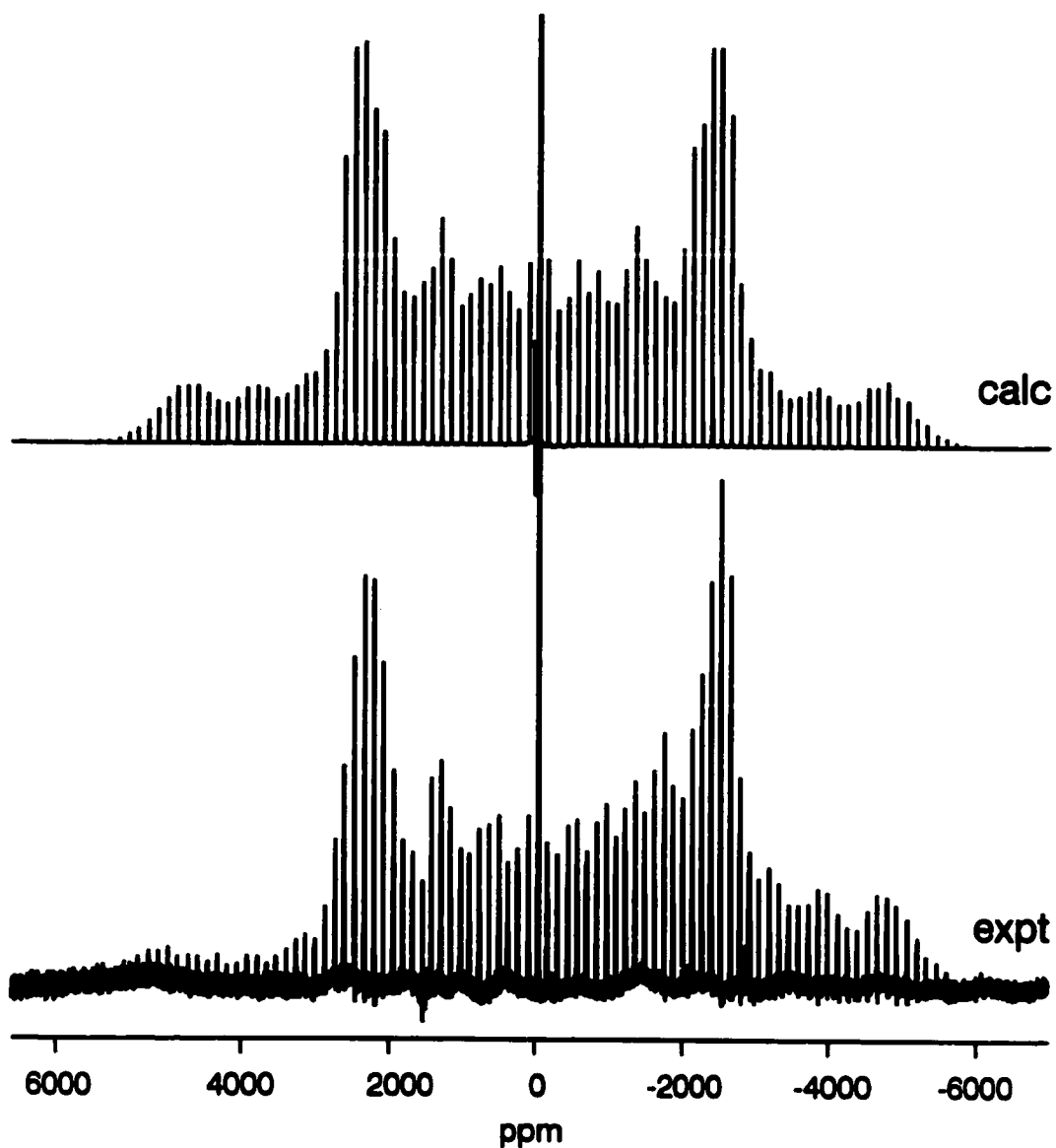
Figure 11   Copper-63 MAS NMR spectrum of the central and satellite transitions
in $K_3Cu(CN)_4$ at 9.4 T. (Spinning rate: 14.00 kHz; number of
transients: 3600) The calculated spectrum is based on a time-domain
calculation involving anisotropic shielding and the first-order
quadrupolar interaction, according to the tensors determined from
non-spinning samples. The central transition in both traces is truncated
to exhibit the spinning sideband envelope of the satellite transitions.
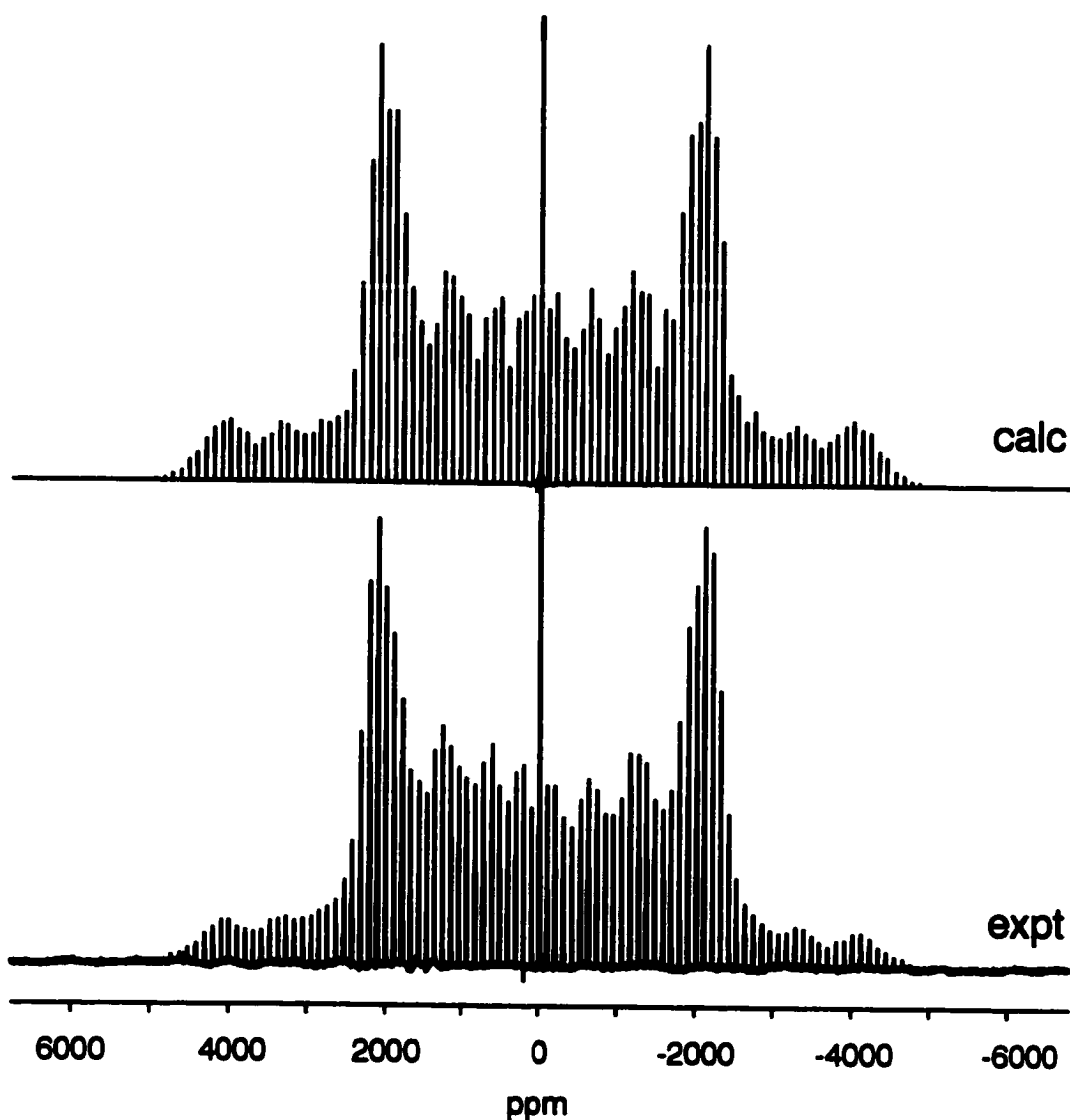
Figure 12   Copper-65 MAS NMR spectrum of the central and satellite transitions in $K_3Cu(CN)_4$ at 9.4 T. (Spinning rate: 12.00 kHz; number of transients: 2560) The calculated spectrum is based on a time-domain calculation involving anisotropic shielding and the first-order quadrupolar interaction, according to the tensors determined from non-spinning samples. The central transition in both traces is truncated to exhibit the spinning sideband envelope of the satellite transitions.

theoretical, limit the usefulness of this method in the present case. For example, spinning rates must be high and very stable, and rf pulses must be strong and homogeneous over the entire detection range. In this case, a strong, broad signal due to copper in the probe is observed 1500 ppm to high frequency of aqueous $Cu(CN)_4^{3-}$. While this interference has been artificially "removed" in the processing stage, spinning sideband intensities in the region of overlap may be unreliable. From the programming point of view, only first-order effects were considered in the simulation, with the consequence that no lineshapes or second-order quadrupolar shifts are calculated. This approximation substantially reduces the required computation time, while still yielding a useful simulation of the data (*18b*). Even with this simplification, time-domain calculations take over an hour for sufficient orientational sampling, thus precluding iterative techniques or extensive visual trial-and-error comparisons. Fundamentally, however, the chemical shielding interaction is simply too small relative to the quadrupolar interaction for the spectral calculations to be sensitive to modifications of its magnitude or orientation. In spite of these limitations, Figure 11 and Figure 12 illustrate that high-quality MAS spectra of the satellite transitions in copper-63/65 NMR may be obtained. The utility of this method for gaining precise information from calculations of the spinning sidebands may be profitably applied in select cases where the quadrupolar and shielding interactions are of comparable magnitude, or where the shielding can be neglected altogether.

Finally, the high sensitivity and moderate quadrupole coupling constant in $K_3Cu(CN)_4$ make it an excellent candidate for testing multiple-quantum magic-angle spinning experiments. The isotropic reconstruction of the 2D data set for the natural abundance sample (Figure 13) consists of a single, featureless peak, flanked by first-order spinning sidebands at ± 5.60 kHz. This observation conforms to the theoretically predicted frequency scaling of spinning sideband positions under conditions of 3QMAS rotating at 10.00 kHz.

Given the relative ease with which one may observe copper-63/65 NMR signals in this sample, how easy is it to measure *J*-couplings by directly probing the copper nucleus? A sample of $K_3Cu(CN)_4$, enriched to about 30% in ^{13}C, was
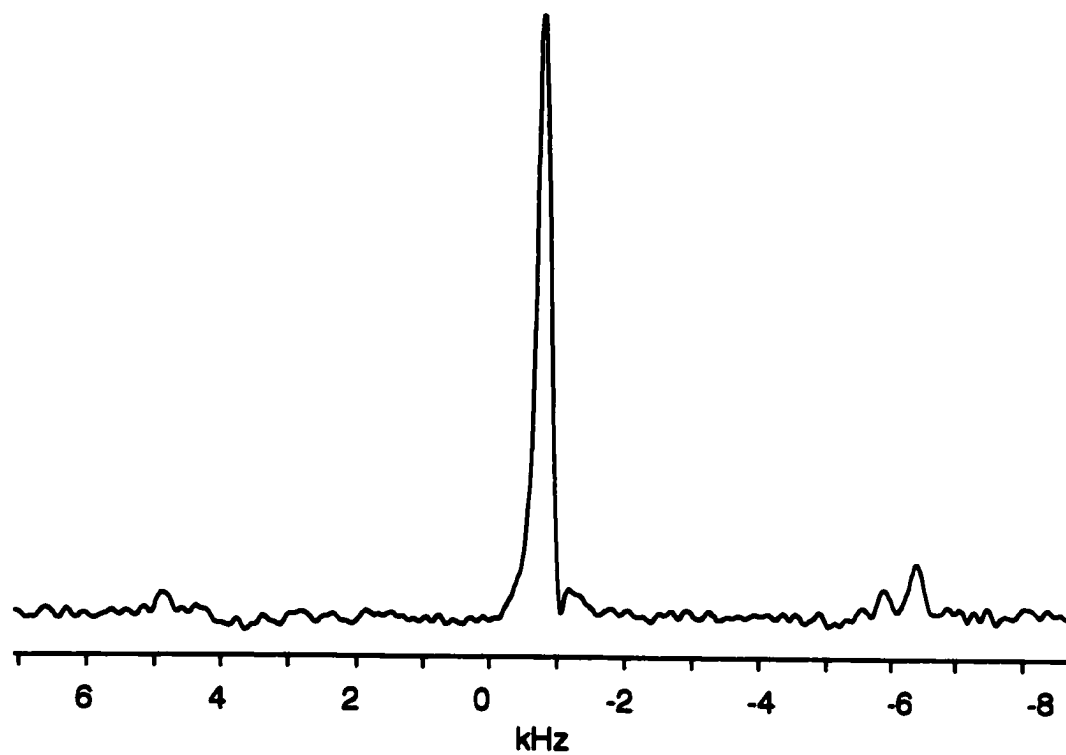
Figure 13   Isotropic reconstruction of ^{63}Cu triple-quantum MAS NMR data in
natural abundance $K_3Cu(CN)_4$. Twenty-four transients were collected
for each of the 128 t_1 slices. The interpulse delay was incremented by
25.7 μs.

analyzed by MAS NMR at 4.7 and 9.4 T. From the spectra in Figure 14 and Figure 15, it is apparent that the lineshape loses its characteristic definition, becoming a series of humps and shoulders about 800 Hz wide. These spectra represent the superposition of multiple copper sites weighted by the statistical abundances of copper nuclei coupled to zero, one, two and three carbon-13 nuclei. With the knowledge of C_Q, η and δ_{iso} gained from NMR analyses of the unlabelled compound, these lineshapes may be simulated to obtain estimates of J, assuming that coupling to zero and one ^{13}C nucleus dominate the observed peaks at this level of isotopic enrichment. However, because of the lack of definition in the lineshape, reasonable fits can be obtained for a large range of subspectral amplitudes and positions; this approach is rather insensitive to J-coupling.

The application of ^{63}Cu 3QMAS to the isotopically enriched sample provides an alternate direct approach to the determination of $^1J(^{13}C,^{63}Cu)$. In Figure 16, the ^{63}Cu 3QMAS spectrum exhibits a central peak representing uncoupled copper-63, flanked by a doublet with a splitting of 650 Hz. Since splittings due to indirect spin-spin coupling are larger than the actual value of J (30), $^1J(^{13}C,^{63}Cu)$ can be computed from this splitting to be about 305 Hz. Also observed in this spectrum are smaller peaks separated by 1260 Hz, which can be attributed to copper-63 coupled to *two* carbon-13 nuclei.

Carbon-13 NMR. Carbon-13 MAS NMR spectra of a $K_3Cu(CN)_4$ sample enriched to 30% in $^{13}C^{15}N$ were acquired at both 4.7 and 9.4 T (Figure 17). To a first approximation, the observed lineshapes represent two sites, each coupled to a spin-3/2 nucleus with isotropic J-couplings given by the separation between peaks. The isotropic chemical shifts are the average value of the four peaks, amounting to a one part-per-million difference between the sites. The intensities of the interleaved quartets clearly identify the sites as arising from the cyanide ligand lying along the rotation axis ("site 1"), and the three remaining chemically equivalent cyanides ("site 2"). A more detailed analysis reveals that the splittings between adjacent peaks for a given site are unequal. These subtleties may be understood in terms of first-order
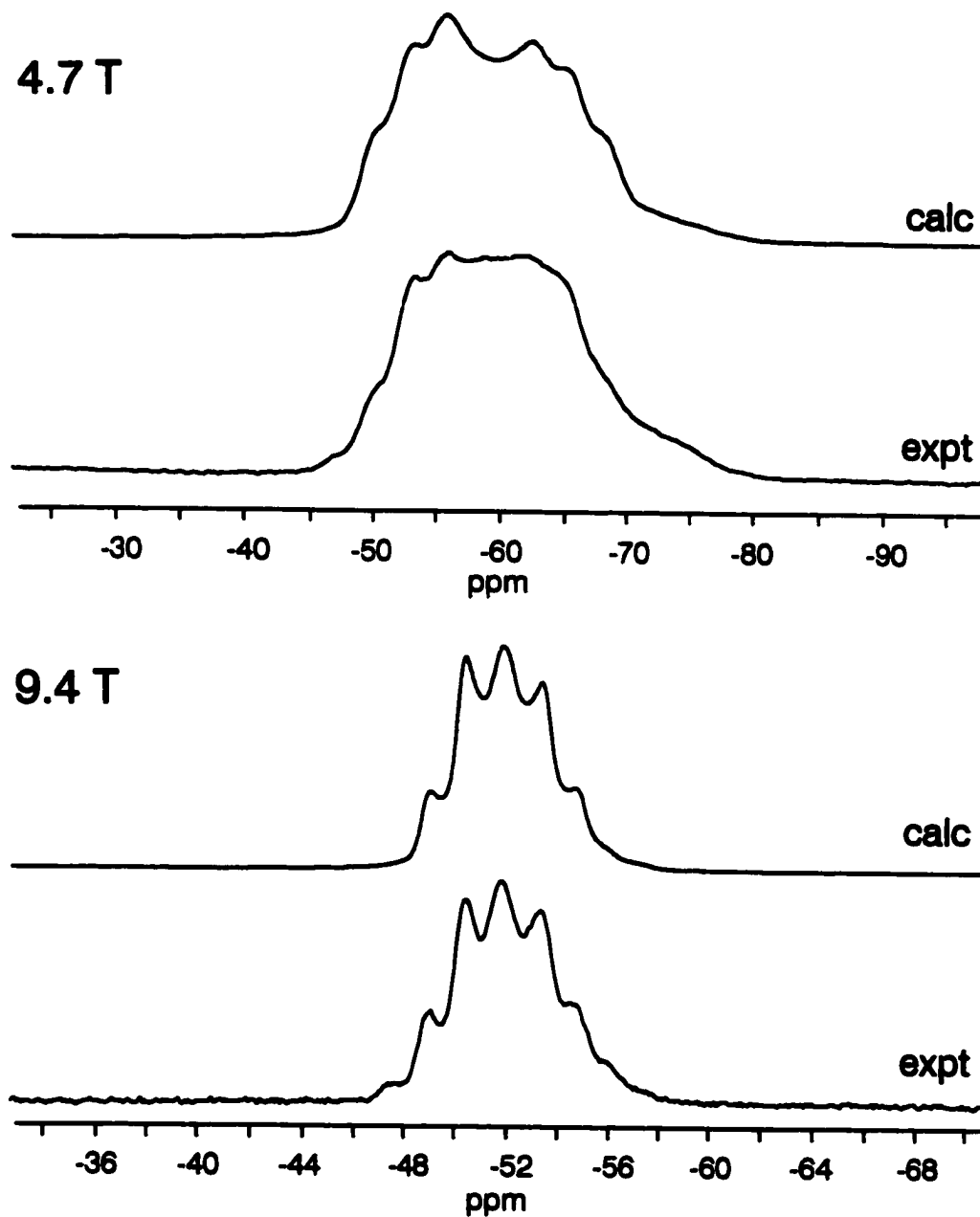
Figure 14   Copper-63 MAS NMR spectrum of the central transition in 30%
^{13}C-enriched K$_3$Cu(CN)$_4$ at 4.7 and 9.4 T. At 4.7 T, 1200 transients
were collected with a 3.00 kHz spinning speed; 32 transients were
acquired at 9.4 T, with a spinning frequency of 6.40 kHz. The
depicted regions each span 4 kHz.

4.7 T

calc

expt

-30 -40 -50 -60 -70 -80 -90
ppm

9.4 T

calc

expt

-36 -40 -44 -48 -52 -56 -60 -64 -68
ppm
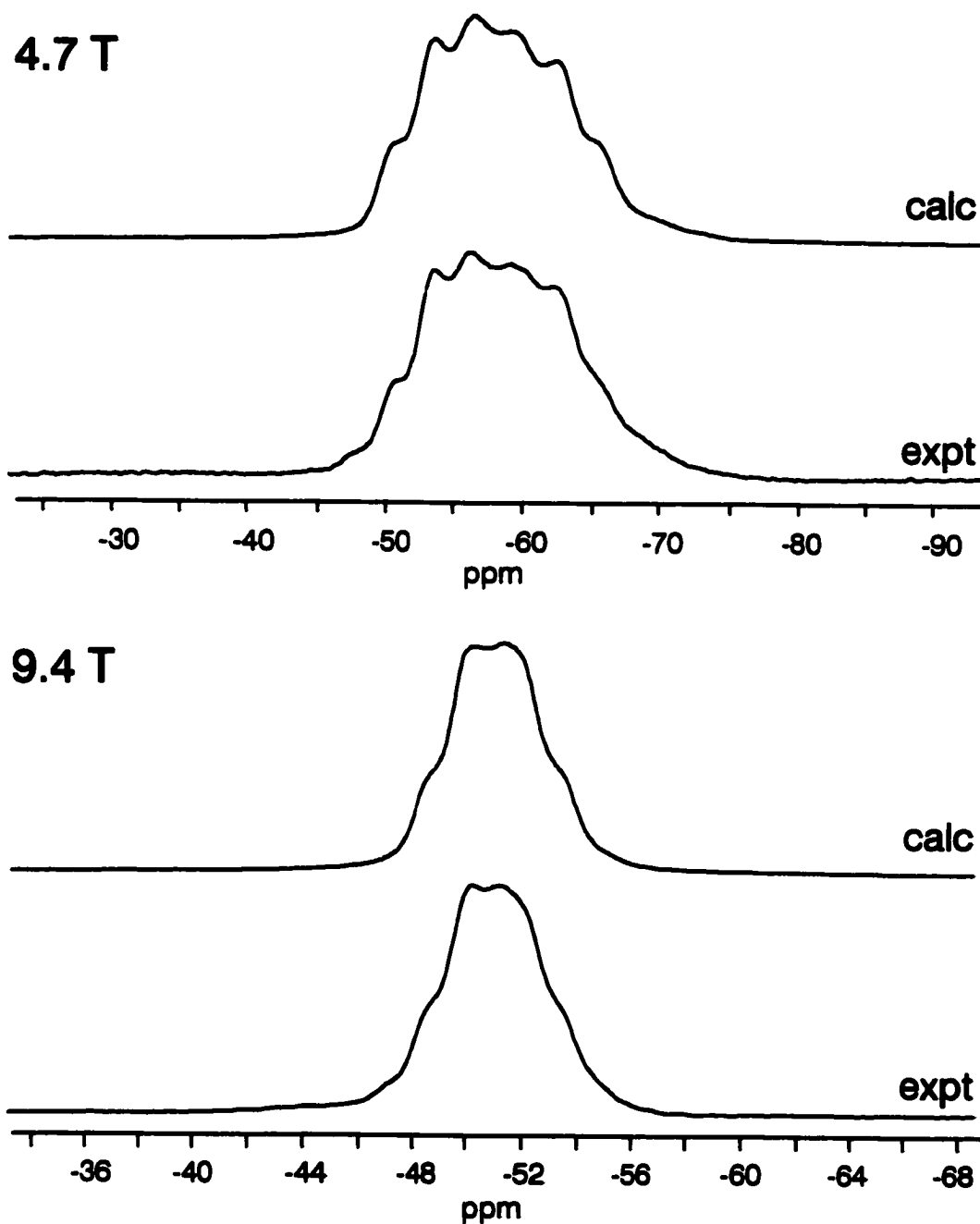
Figure 15   Copper-65 MAS NMR spectrum of the central transition in 30%
^{13}C-enriched $K_3Cu(CN)_4$ at 4.7 and 9.4 T. 1400 transients were
collected at 4.7 T with a 3.40 kHz spinning speed; At 9.4 T, 256
transients were acquired, with a spinning rate of 10.00 kHz. The
depicted regions each span 4 kHz.
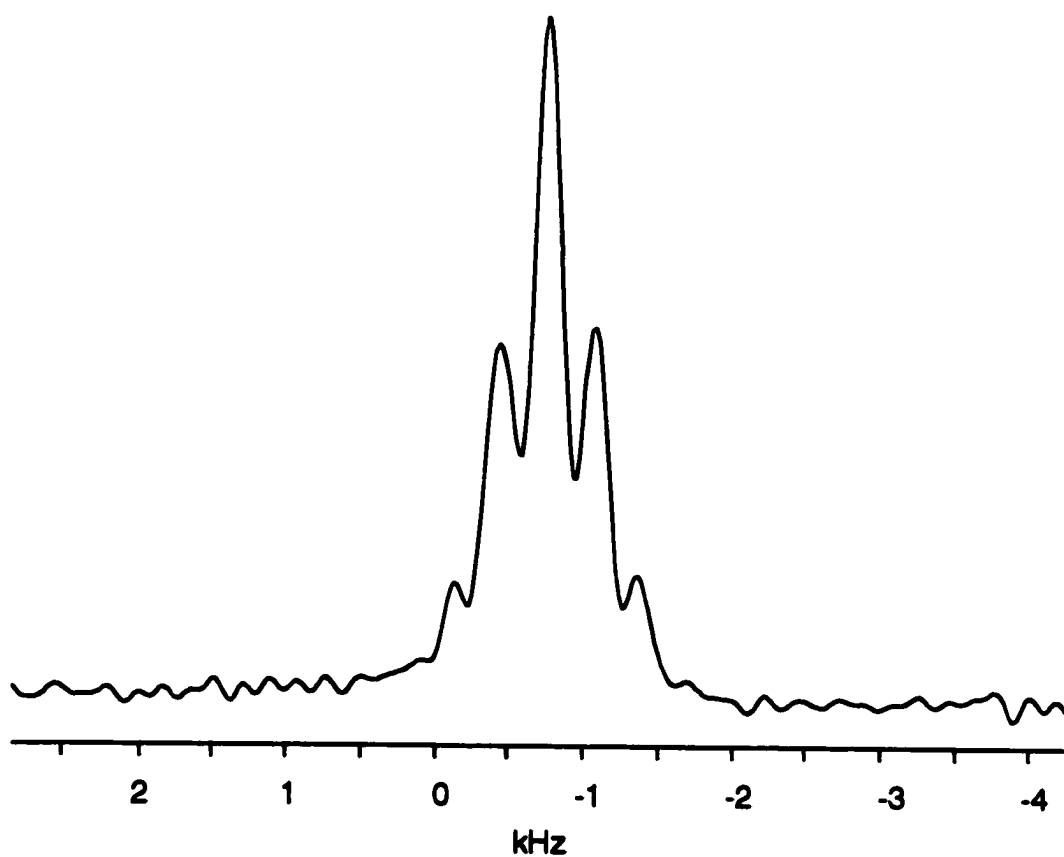
Figure 16   Isotropic reconstruction of ^{63}Cu triple-quantum MAS NMR data in 30% ^{13}C-enriched $K_3Cu(CN)_4$. Two-hundred forty transients were collected for each of the 128 t_1 slices. The interpulse delay was incremented by 25.7 μs.

4.7 T

calc

expt

180   170   160   150

ppm

9.4 T

calc

expt

170   165   160   155   150

ppm
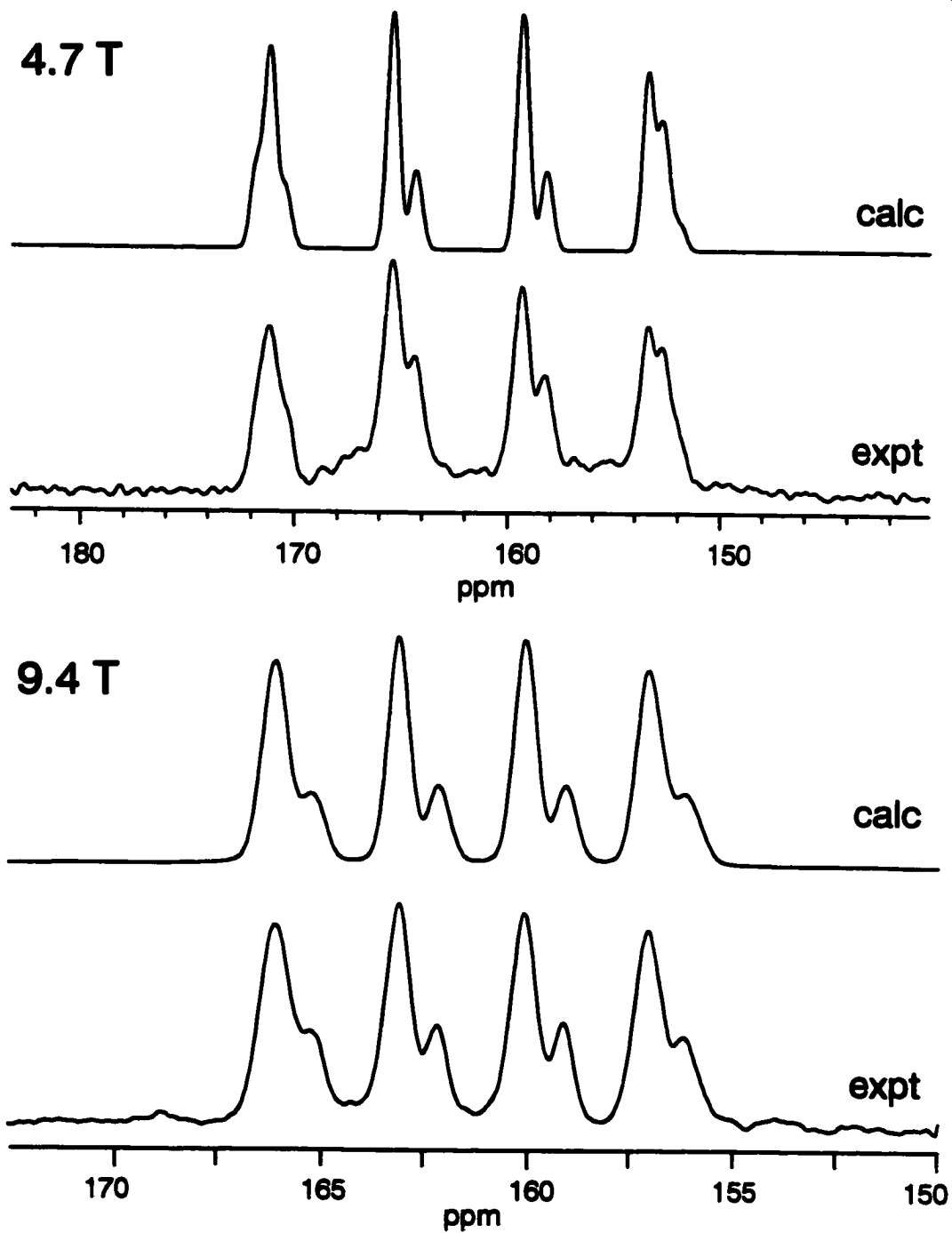
Figure 17   Carbon-13 MAS NMR spectra of 30% $^{13}C^{15}N$-enriched $K_3Cu(CN)_4$ at 4.7 and 9.4 T. For the experimental spectrum at 4.7 T, 208 transients were acquired at a 3.50 kHz rotation rate. For the 9.4 T spectrum, 608 transients were collected at a rotation rate of 8.00 kHz.

perturbation theory as residual dipolar shifts originating in the quadrupolar nature of the coupled copper nuclei:

$$\Delta \nu_{m_S} = \left[\frac{3 R_{eff} C_Q}{20 \nu_L} \right] \left[\frac{S(S+1) - 3 m_S^2}{S(2S-1)} \right] (3 \cos^2 \beta_D - 1 + \eta \sin^2 \beta_D \cos 2 \alpha_D) \tag{65}$$

where (α_D, β_D) are polar angles defining the orientation of r_{IS} relative to the EFG PAS. Employing the approach of Olivieri and coworkers (*43,44,45*), these lineshape distortions may be precisely simulated, yielding the values listed in Table 4.

It is important to emphasize that successful calculations rely on a great deal of prior information. In this case, the copper-63/65 NMR results supplied the magnitudes of C_Q. The crystal structure was critical: dipole-dipole coupling constants, R_{DD}, were calculated from internuclear separations to be 983 and 1015 Hz to copper-63 for sites 1 and 2, respectively. Foreknowledge of the molecular symmetry fixed the relative orientations of the internal interactions, and the orientation of $r_{Cu,C}$ relative to V_{33} is determined from the bond angles. Although coupling to both spin-active copper nuclei was included, parameters were varied according to the ratio of their magnetogyric ratios. No evidence of anisotropic spin-spin coupling was detected.

In addition to J_{iso} and δ_{iso}, these simulations yield the sign of C_Q. For this particular case, axial symmetry, isotropic J-coupling and the spin factors may be introduced to simplify expression (65):

$$\Delta \nu_{\pm 1/2} = + \left[\frac{3 R_{DD} C_Q}{20 \nu_L} \right] (3 \cos^2 \beta_D - 1) \tag{66}$$

$$\Delta \nu_{\pm 3/2} = - \left[\frac{3 R_{DD} C_Q}{20 \nu_L} \right] (3\cos^2 \beta_D - 1) \qquad (67)$$

The dipolar coupling constant being positive by virtue of like signs for $\gamma(^{63/65}Cu)$ and $\gamma(^{13}C)$ (equation (24)), and the orientational term depending in a predictable fashion on the structure, the sign of C_Q governs the direction of the line shifts. Since the high frequency peak splitting for site one is stretched, and the low frequency splitting squeezed, C_Q must be negative. For site two, the sign of the orientational term is negative ($\beta_D = 70°$), justifying the observation that the high frequency splitting is squeezed, leading again to a negative quadrupole coupling constant.

A ^{13}C NMR spectrum of a non-spinning sample of 30% ^{13}C-labelled was also acquired at 4.7 T (Figure 18). Although the low frequency end is poorly defined, the powder pattern is indicative of an axially symmetric shielding tensor, with the chemical shift for perpendicular orientations easily discernable. Contrasting with the MAS spectra, dipolar interactions with neighbouring ^{14}N nuclei will be present in these "static" spectra along with copper-63/65 couplings, thus producing additional splittings. Given the complexity of the spin system, no attempt was made to calculate the spectrum; however $\delta_\perp$ was estimated from the average value of the singularities in Figure 18. Individual carbon-13 sites are not resolved, suggesting that the *local* molecular symmetry of site two is sufficient to produce essentially axial symmetry in the shielding tensor. From the measured values of δ_{iso} and $\delta_\perp$, $\delta_\parallel$ may be calculated to yield a span for the cyano ^{13}C shielding tensors of 340 ± 5 ppm.

The carbon shielding in $K_3Cu(CN)_4$ may be compared with other cyanide-containing compounds. First, the isotropic chemical shifts of 161 and 162 ppm agree with the value obtained in aqueous solution, $\delta_{iso} = 161.6$ ppm (*122*). They appear to be more deshielded than any other organic or inorganic cyanide compound investigated in the solid phase by NMR (*123*), and more *shielded* than the "free" CN anion in solution (166.2 ppm) (*122*). Whereas organic nitriles tend to appear around 120 ppm, the tetrahedral group 12 tetracyanometallates possess δ_{iso} between 148 and
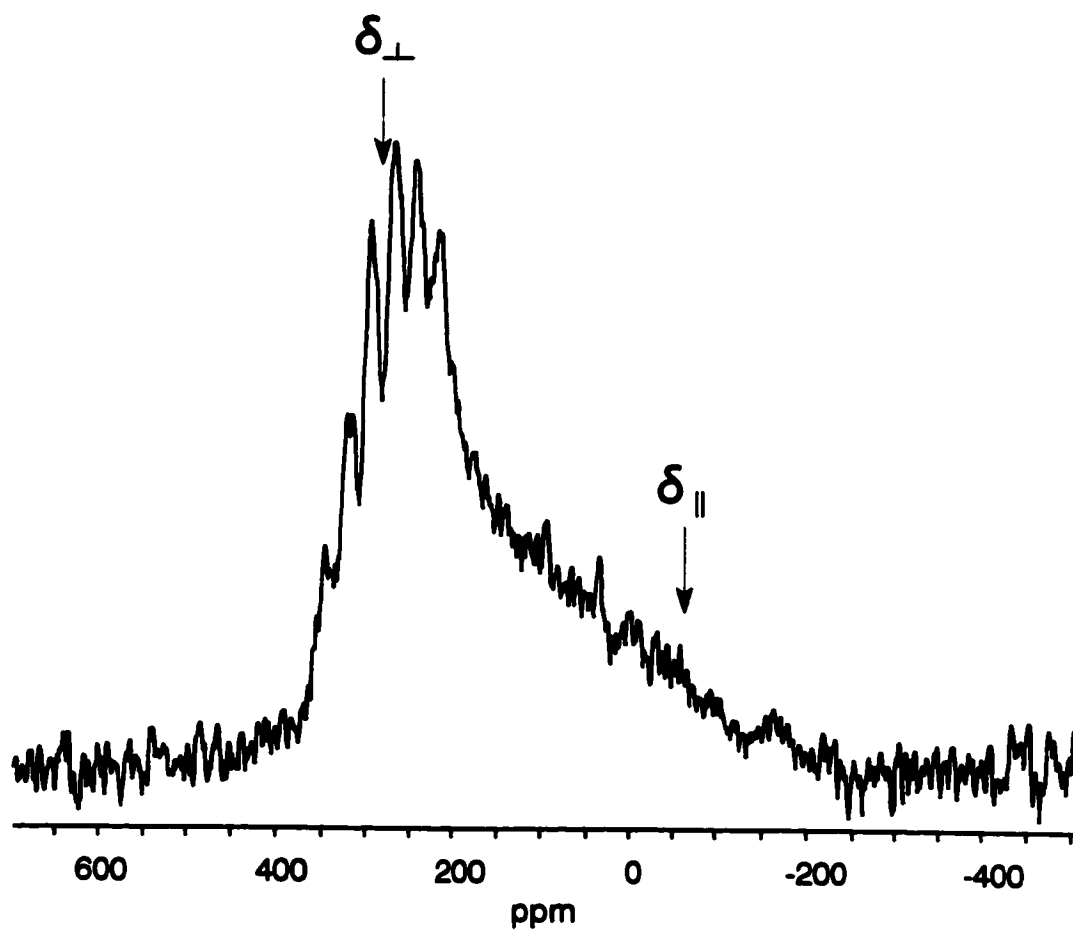
Figure 18 Carbon-13 NMR spectrum of stationary 30% ^{13}C-enriched $K_3Cu(CN)_4$ at 4.7 T (439 transients). Principal components of the axially symmetric shielding tensor are labelled with arrows.

153 ppm *(40)*. The remarkably similar species, $N(CH_3)_4CuZn(CN)_4$, exhibits an isotropic shift of 157 ppm *(109)*. Even more shielded are the square-planar group 10 tetracyanometallates, having δ_{iso} ranging from 128 to 139 ppm *(124)*. The spans of the related tensors exhibit less variability and correspondingly less obvious trends, with organic nitriles generally having $\Omega \approx 320$ ppm and the tetracyanometallates displaying spans of approximately 330 ppm (group 12 tetrahedra) and 350 ppm (group 10 square-planars). For $Cu(CN)_4$ tetrahedra in $N(CH_3)_4CuZn(CN)_4$ and $K_3Cu(CN)_4$, the spans fall between these values. By implication, these generalities suggest that all carbon-13 shielding tensor elements are modified on moving from organic- to metal-bound cyanides.

Nitrogen-15 NMR. A 75% ^{15}N-enriched sample of $K_3Cu(CN)_4$ was prepared and analyzed by ^{15}N NMR. Figure 19 depicts the isotropic powder lineshapes under conditions of magic-angle spinning at 4.7 and 9.4 T. The two types of chemically equivalent cyanide ligands are clearly evident from the intensity ratio of 1:3, the more shielded lying along the symmetry axis. The difference in the isotropic ^{15}N chemical shifts is larger than the ^{13}C shift difference by a factor of six. Indeed, nitrogen shifts are generally more sensitive to structural differences than carbon shifts, manifesting in a larger overall range of nitrogen-15 chemical shifts *(123)*. In constrast to the ^{13}C NMR results, the isotropic chemical shifts of 282.5 and 288.5 ppm are less shielded than the "free" cyanide ligand in water, 274.2 ppm *(125)*.

Fine structure is observed in the individual lineshapes corresponding to the two sites. Since 98.9% of the carbon in the sample is the spin-inactive isotope carbon-12, these features must be due to two-bond *J*-coupling to copper-63/65. Following the same protocol as for the carbon-13 MAS spectra, simulations yield $^2J(^{63}Cu,^{15}N) = 19.0 \pm 0.2$ and 20.0 ± 0.2 Hz for sites 1 and 2, respectively. Dipolar coupling constants, $R_{DD}(^{63}Cu,^{15}N)$, calculated from structural data are -107 and -104 Hz, according to equation (24).

Spectra of the non-spinning sample were also acquired, with results similar to the carbon-13 spectra (Figure 20). The low frequency end of the axially symmetric
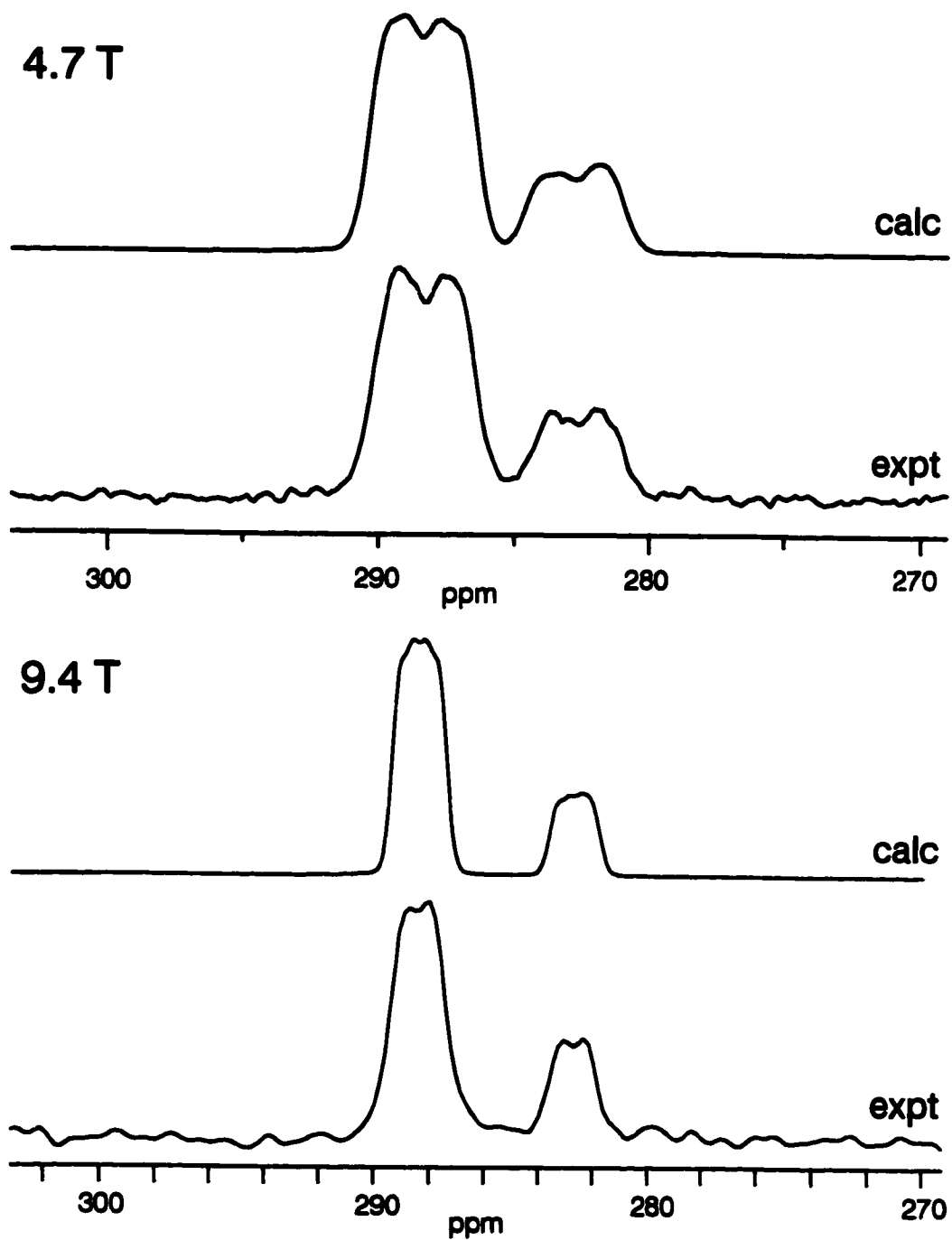
Figure 19   Nitrogen-15 MAS NMR spectra of 75% ^{15}N-enriched K$_3$Cu(CN)$_4$ at
4.7 and 9.4 T. Forty-six and 16 transients were coadded for the 4.7
and 9.4 T spectra, respectively. The spinning rates were 2.91 and
10.00 kHz.
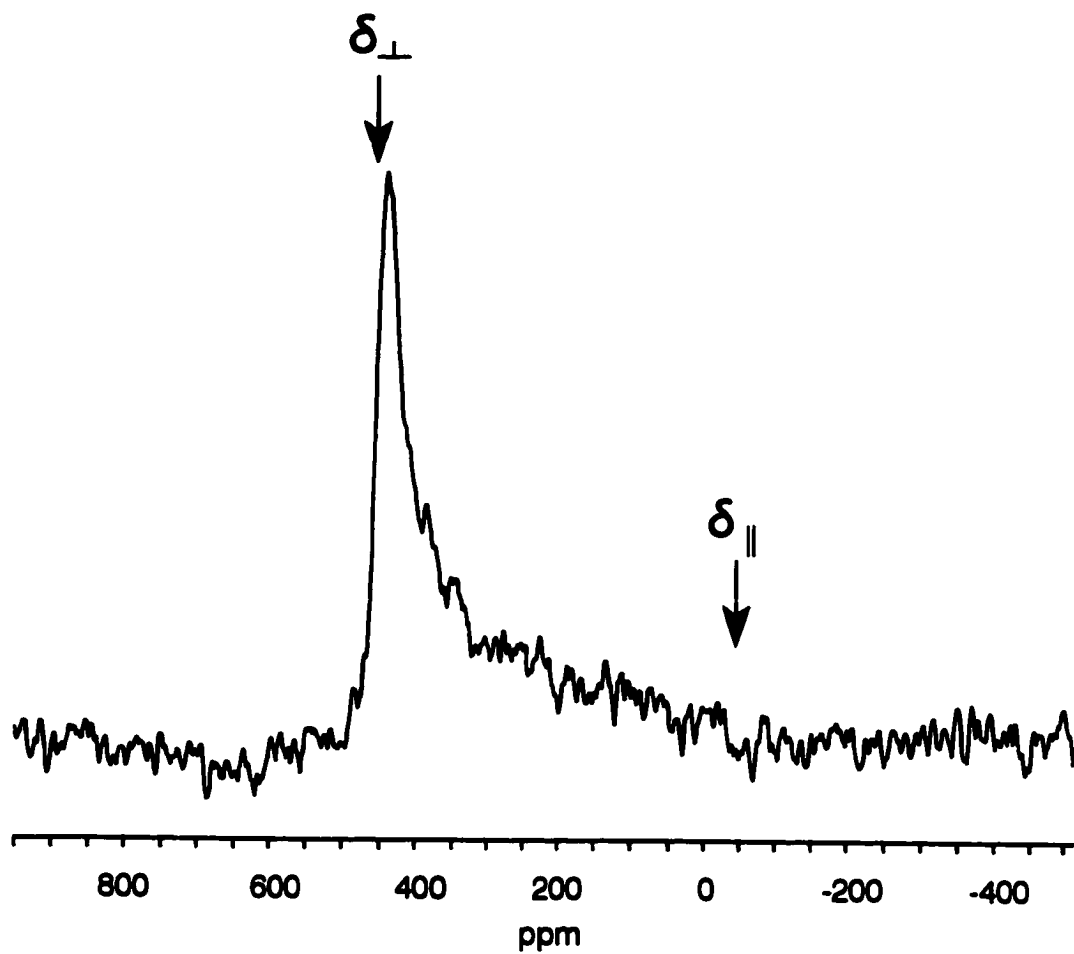
Figure 20   Nitrogen-15 NMR spectrum of non-spinning 75% ^{15}N-enriched
$K_3Cu(CN)_4$ at 4.7 T. One-hundred twelve transients were collected.
Principal components of the axially symmetric ^{15}N shielding tensor are
indicated by arrows.

powder pattern lacks definition, and the two chemically distinct sites are unresolved, but $\delta_\perp$ may be easily extracted. Calculating $\delta_\parallel$ as above, the nitrogen-15 shielding tensor spans nearly 500 ppm, with the most shielded component aligned with the Cu–C–N bond.

These NMR results may be compared with those obtained for solid $K_2Hg(CN)_4$ (*113*), in which the mercury atom occupies a site of pure tetrahedral symmetry. The isotropic chemical shift is 280.9 ppm in this compound, very similar to the values 282.8 and 288.5 ppm found for $K_3Cu(CN)_4$. The measured shielding anisotropies are very similar, (Ω = 477 ppm from Herzfeld-Berger analysis (*126*) of spinning sideband intensities), with the same tensor orientation. Also comparable is the two-bond *J*-coupling to the metal, which was determined to be 29 Hz to mercury-199, and 19 or 20 Hz to copper-63. The shielding results for tetrahedral cyanometallates contrast with organic nitriles, which typically exhibit spans of 400 ppm and isotropic shifts near 260 ppm (*123*). The origin of these differences appears to lie in lower shielding perpendicular to the M–C–N bond for cyanometallates than for R–C–N moieties.

Conclusions

Tripotassium tetracyanocuprate has been thoroughly examined by a variety of NMR methods, yielding fully characterized chemical shielding tensors for carbon-13, nitrogen-15 and copper-63/65, as well as electric field gradient tensors for copper-63/65. This appears to be the first example of copper-63/65 shielding anisotropy reported for a solid compound. Isotropic one- and two-bond J-couplings to the copper centre have been measured for both cyanide sites. This comprehensive investigation of NMR properties in a "simple" model compound of known crystal structure is suggestive of the powerful capacity of NMR in the characterization of supramolecular framework materials based on tetrahedral $Cu(CN)_4^{-3}$ building blocks. Where multiple copper sites exist in a given solid, triple-quantum MAS appears to be a viable method for resolving individual resonances, given its capacity to resolve splittings arising from J-coupling. These results also underscore the merits of utilizing modest levels of $^{13}C^{15}N$-enrichment to obtain high-quality C-13 and N-15 MAS NMR spectra, while simultaneously simplifying the C-13 spectral analysis by removing quadrupole-perturbed ^{13}C-^{14}N dipolar interactions (*109a*). Finally, the work described here represents a starting point for a systematic study of copper(I) cyanide complexes.

2.4.3 Other Studies

In addition to the examples presented above, other compounds were examined by MQMAS for evidence of splittings due to J-coupling. Of particular interest was the experimental demonstration of equation (64) for nuclei possessing spins 5/2 and 7/2. This has proven more difficult than originally anticipated. Below are outlined some of the obstacles encountered in these attempts.

Triphenylphosphine Oxide. A sample of Ph_3PO, enriched to approximately 37% in ^{17}O ($S = 5/2$), was kindly provided by Dr. Klaus Eichele. Upon recrystallization from dichloromethane, crystals formed in the orthorhombic space group, *Pbca* (crystal structure determination by Prof. T. S. Cameron). One unique molecule appears in the solid with nearly axial symmetry along the P-O bond ($r_{P,O} = 1.489$ Å). The oxygen-17 MAS spectrum (Figure 21) was calculated with a quadrupole coupling constant of 4.6 MHz, $\eta = 0$, and $\delta_{iso} = 45$ ppm relative to water. The indirect spin-spin coupling constant, $^1J(^{31}P,^{17}O)$, is 170 Hz, based on fitting the shoulders at the high-and low-frequency singularities. These data suggest $Ph_3P^{17}O$ as an excellent candidate for MQMAS. However, even with a high level of isotopic enrichment, the central transition lineshape under fast MAS required at least 16 scans – with a recycle delay of 20 s – to emerge from the noise. The implications of this low sensitivity for MQMAS observation are dire, and it did not prove possible to detect an echo in one-dimensional 3QMAS free-induction decays. Although optimal pulse lengths for excitation and transfer of multiple-quantum coherences have been suggested on the basis of numerical calculations (*76*), these will be influenced by the ratio, ν_Q/ν_{rf}, and by the spinning speed (*127*), thereby necessitating pulse optimization for a given sample and set of experimental conditions. In the present case, the notoriously low sensitivity of oxygen-17 conspired with inherently poor excitation and coherence transfer properties for spin-5/2 nuclei to preclude signal observation. A critical factor in this case was long relaxation times, which severely limited the number of transients that could be recorded in a reasonable amount of time. Also important for improving sensitivity and dipolar decoupling in MQMAS is

fast spinning rates. However, the gains associated with rapid sample rotation may be offset by sensitivity losses due to the small sample sizes of fast spinning probes. Finally, it must be emphasized that these attempts were made to observe triple-quantum MAS spectra, where the scaling factors in Table 3 will work to *reduce* the observed splitting relative to the true J-coupling by a factor of 0.55. Since linewidths in ^{17}O 3QMAS isotropic spectra of crystalline phosphates are reported to be about 100 Hz (*128*), this splitting may be only partially resolved. More interesting would be to perform the 5QMAS experiment, where the 170 Hz J-coupling is predicted to appear as a splitting of 390 Hz. However, unless 3QMAS signals are very strong, 5QMAS spectra will be difficult to observe (*76*).

Tripotassium Hexacyanocobaltate. Attracted by the high NMR receptivity of ^{59}Co, a sample of $K_3Co(CN)_6$ was enriched with $^{13}C^{15}N$ to facilitate the observation of $^1J(^{59}Co, ^{13}C)$ (sample kindly prepared by Mr. Richard Warren). This coupling, observed in solution by ^{13}C NMR, is 126 Hz (*129*). Moreover, solid $K_3Co(CN)_6$ possesses a single cobalt site with short relaxation times and a modest C_Q of 6.2 MHz. In stark contrast to triphenylphosphine oxide, the ^{59}Co MAS signal is strong, appearing with good signal-to-noise after 8 scans at 1 transient per second. In this case, however, the extreme sensitivity of cobalt-59 chemical shielding results in a marked temperature-dependence of both peak position and lineshape. Figure 22 depicts cobalt-59 MAS spectra of $K_3Co(CN)_6$ rotating at 5, 10 and 15 kHz. Increases in temperature due to rapid sample spinning induce a net shift of the peak maximum from -16 to -8 to +11 ppm with respect to an aqueous solution of $K_3Co(CN)_6$ at 21°C. In solution, the temperature-dependence of the $Co(CN)_6^{3-}$ anion is 1.38 ppm K^{-1} (*130*), thus implying an overall increase in sample temperature of nearly 20°. More troublesome in terms of spectral resolution is that a loss of definition is observed in the peaks. This may be attributed to thermal gradients within the rotor creating a distribution of chemical shifts and – to a lesser degree – quadrupole coupling constants. These broadening effects would not, of course, be eliminated by MQMAS.

Nonetheless, triple-quantum MAS experiments were carried out as a prelude to attempting higher-order coherence correlations, in full recognition that 3QMAS J-splittings for $S = 7/2$ are scaled by 0.23 (i.e. $^1J_{3Q}(^{59}Co,^{13}C) = 29$ Hz). Echoes arising from 3Q/1Q correlations were easily observed, as reported in reference (78). In spite of this success, no signals were detected in 5Q or 7Q MAS experiments. Disappointing as this was, it should be noted that even if weak echoes could be obtained, full resolution of the amplified J splitting may be difficult for a variety of reasons. First, cyanide exchange in this compound is very slow (131), and even at elevated temperatures, the total incorporation of $^{13}C^{15}N$ was insufficient to produce a reasonable ^{13}C MAS spectrum of the solid. The level of isotopic enrichment was high enough to detect the expected octet in a ^{13}C solution NMR spectrum – it was not observed in a solution at natural abundance – but a more quantitative assessment was not done. Second, temperature effects may contribute to substantial peak broadening in isotropic MQMAS spectra. Third, the doublet arising from coupling to ^{13}C would be superimposed on a prominent peak representing "uncoupled" cobalt-59. This in combination with a substantial isotope shift of -0.93 ppm (-88 Hz at 9.4 T) in aqueous solution may limit the possibility of observing fully resolved peaks by MQMAS, even utilizing the 5Q ($^1J_{5Q}(^{59}Co,^{13}C) = 214$ Hz) and 7Q ($^1J_{7Q}(^{59}Co,^{13}C) = 291$ Hz) coherences.
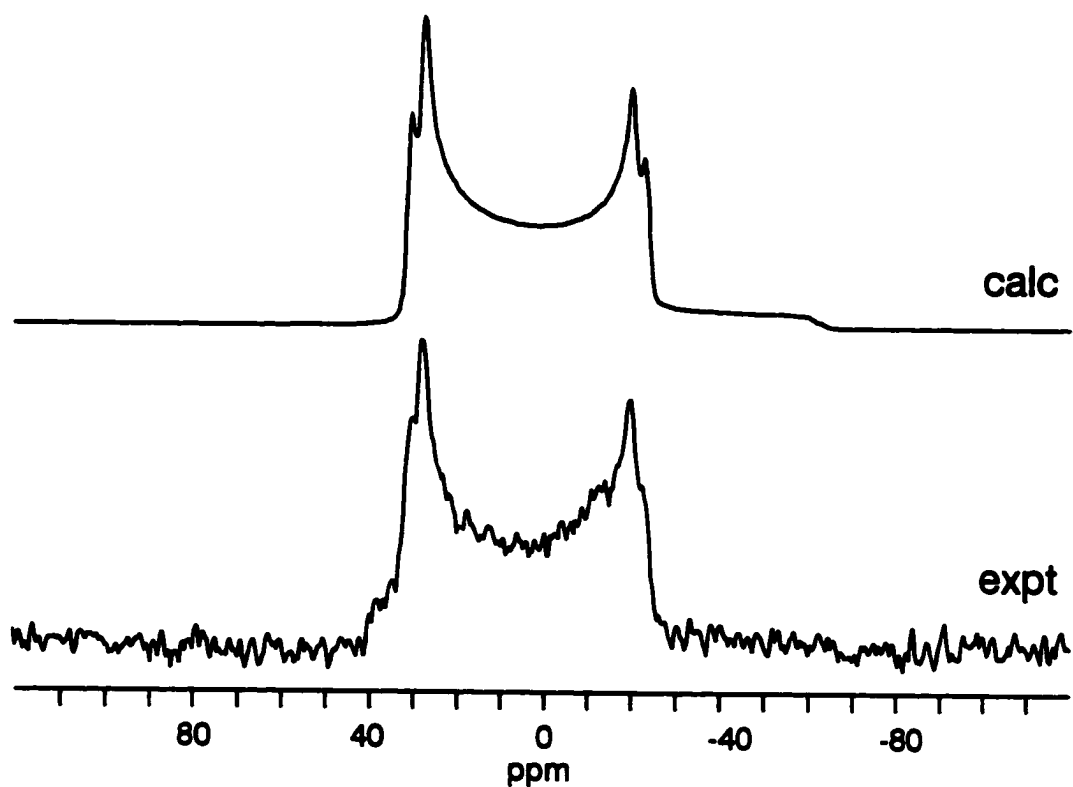
Figure 21   Oxygen-17 MAS NMR spectrum of the central transition in 37% ^{17}O-
            enriched triphenylphosphine oxide, recrystallized from
            dichloromethane. Experimental spectrum was collected at 9.4 T
            (54.248 MHz) with 2058 transients separated by a relaxation delay of
            20 s, rotating at 9.10 kHz.
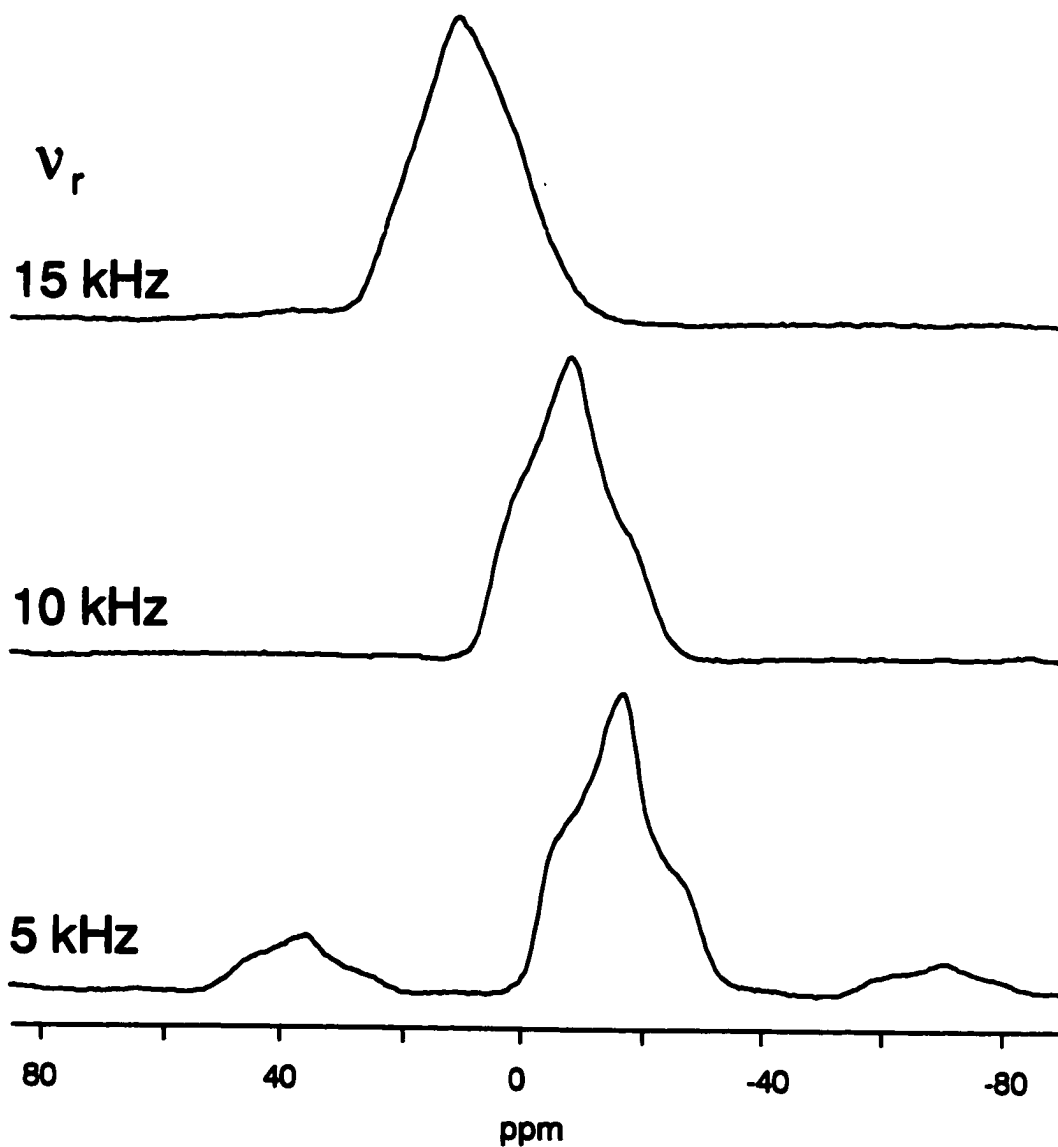
Figure 22   Cobalt-59 MAS NMR spectra of the central transition in $K_3Co(CN)_6$ acquired in a magnetic field of 9.4 T (94.94 MHz) at three spinning frequencies, ν_r. Each spectrum is the result of 128 transients separated by a 1 s relaxation delay.

2.5 Summary

Multiple-quantum magic-angle spinning holds great promise for the study of half-integer quadrupolar nuclei in solids. Still in its infancy, MQMAS has proven itself in many important applications as a versatile and robust technique. Future research will undoubtedly focus on maximizing sensitivity and quantitative utility through improvements in MQ coherence excitation and transfer. This contribution describes some subtleties associated with spin-spin coupling involving quadrupolar nuclei, and their influence on isotropic MQMAS spectra. First-order perturbation theory predicts that direct dipolar coupling to spin-1/2 nuclei will not introduce "residual dipolar couplings" into MQMAS spectra, but may affect dipolar splittings in the satellite transitions of single-crystal or powder samples. This conclusion simplifies the interpretation of splittings arising from J-coupled nuclei, which are scaled by a factor which depends on the spin angular momentum quantum number and the symmetric MQ transition involved. Enhancements of greater than two are predicted for MQMAS spectra utilizing the highest available MQ transition. By contrast, triple-quantum MAS experiments for nuclei having $S > 3/2$ will result in J-splittings much smaller than J_{iso}. These theoretical predictions have been verified experimentally for two spin-3/2 nuclei, demonstrating that it is possible to directly measure J-couplings from MQMAS spectra of half-integer quadrupolar nuclei. Attempts to perform analogous experiments on spin-5/2 and spin-7/2 nuclei failed due to poor efficiency of the MQ excitation and/or severely reduced splittings, underscoring the fact that more research must be dedicated to improving the overall sensitivity of this technique to maximize site resolution. Despite these caveats, it is anticipated that with the MQMAS technique, more J-couplings involving half-integer quadrupolar nuclei will become accessible.

3. COPPER-63/65 QUADRUPOLAR EFFECTS IN SPIN-1/2 NMR SPECTRA

In spite of the new frontiers opened up by MQMAS, many quadrupolar nuclei of interest possess large quadrupole moments and/or electric field gradients which render their direct observation by current NMR methodology difficult, if not impossible. Quadrupole moments for copper-63 and copper-65 are -0.211 and -0.195 barn respectively (*132*), comparable to common NMR-accessible nuclides such as aluminum-27 (0.140 barn) and sodium-23 (0.101 barn) (*133*). The coordination chemistry of copper(I) is diverse, however, ranging from highly symmetrical tetrahedral arrangments where the EFG is vanishingly small, to linear, two-coordinate structures, with very large EFGs, yielding C_Q in excess of 80 MHz. Even at the highest magnetic fields available for NMR, the ratio ν_L/ν_Q in the latter is still in the intermediate regime. One approach is to operate at low or no applied field, sacrificing chemical shielding to obtain quadrupole frequencies from powdered samples. "Pure" NQR of copper-63/65 is a well-developed field in its own right, driven in part by its utility in copper-based superconducting materials. The unflagging zeal of E. A. C. Lucken has also contributed to a substantial proportion of the copper quadrupole data in the literature (*134*). In principle, this technique may be performed with standard FT-NMR instrumentation; practically, however, low sensitivity and wide ranges over which the signals may be observed make it difficult to operate without additional components such as a super-regenerative oscillator (*135*).

It is also possible to take advantage of the profound effects a large quadrupole coupling constant can have on the NMR lineshapes of dipolar-coupled spin-1/2 nuclei to gain insight about the EFG. In favourable circumstances, the spin-1/2 nucleus acts as a "spy". In this chapter, the theory governing such interactions is reviewed, and examples are presented where these effects are used as a means to "recouple" the dipole-dipole coupling constant, thereby obtaining direct structural information.

3.1 The Zeeman-Quadrupolar Interaction

The following theoretical framework is based on the presentation by Menger and Veeman (*49*), and can be described qualitatively in the following way. The quadrupole-perturbed Zeeman eigenstates are expressed as linear combinations of the pure Zeeman states, the coefficients of which are obtained by diagonalization of the full S-spin Hamiltonian matrix, comprising contributions from the quadrupolar and Zeeman Hamiltonian operators. This exercise yields the coefficients for a given orientation of the magnetic field in the EFG principal axis system. The direct and indirect I,S dipolar interactions can then be calculated as frequency shifts which add to the shielding. These frequencies are based on the expectation values of the spin angular momentum operators $\hat{S}_z$ and $\hat{S}_x$, which, in turn, are functions of the S-spin coefficients and of the orientation of the magnetic field with respect to the dipolar vector. In this manner, the stationary powder spectrum can be computed by evaluating these terms for a sufficient number of orientations of the spin pair with respect to the applied magnetic field. The MAS spectrum is calculated by extension of this method, averaging the powder pattern over many orientations to simulate rapid rotation of the sample about the magic angle with respect to the applied magnetic field.

The Zeeman-quadrupolar eigenstates, $|\varphi_i'\rangle$, are expanded in terms of the pure Zeeman eigenstates, $|\varphi_k\rangle$:

$$|\varphi_i'\rangle = \sum_k a_{ik} |\varphi_k\rangle \quad . \tag{68}$$

The index, i, refers to the ith energy level, and, for $S = 3/2$, the Zeeman states, correspond to $|\varphi_1\rangle = |+3/2\rangle$, $|\varphi_2\rangle = |+1/2\rangle$, $|\varphi_3\rangle = |-1/2\rangle$, $|\varphi_4\rangle = |-3/2\rangle$, with eigenvalues, m_S. The full S-spin Hamiltonian operator is constructed from the Zeeman (equation (51)) and quadrupolar (equation (50)) Hamiltonians:

$$\mathcal{H}_S = \mathcal{H}_Z + \mathcal{H}_Q \quad . \tag{69}$$

As in section 2.3.1, this expression is valid for an axially symmetric EFG tensor, where the angle between the unique component of the EFG tensor and B_0 is θ. The Hamiltonian matrix is constructed in the usual way,

$$\langle \varphi_i \mid \mathcal{H}_S \mid \varphi_k \rangle \tag{70}$$

with the Zeeman interaction contributing only to the diagonal elements, and quadrupolar terms entering both diagonal and off-diagonal elements:

$$\begin{bmatrix} \dfrac{-3\nu_L}{2} + A & B & C & 0 \\[2ex] B & \dfrac{-\nu_L}{2} - A & 0 & C \\[2ex] C & 0 & \dfrac{+\nu_L}{2} - A & B \\[2ex] 0 & C & B & \dfrac{+3\nu_L}{2} + A \end{bmatrix} \tag{71}$$

$$A = \frac{C_Q}{8}(3\cos^2\theta - 1) \tag{72}$$

$$B = \frac{\sqrt{3}\, C_Q}{4}\sin\theta\cos\theta \tag{73}$$

$$C = \frac{\sqrt{3}\, C_Q}{8}\sin^2\theta \quad . \tag{74}$$

The eigenvalue matrix will be diagonal only for crystallite orientations with V_{33} aligned with the applied field, i.e., $\sin\theta = 0$; for all other orientations, non-zero off-diagonal components will appear. The coefficients, a_{ik}, are obtained by diagonalization, and depend on θ.

Once the S-spin coefficients have been obtained for a given orientation of the magnetic field in the EFG principal axis system, the direct and indirect I,S dipolar

interactions can be calculated. If it is assumed that the direct dipolar and indirect spin-spin tensors are coincident, then these interactions have the same orientation dependence, and the net I-spin frequency shift associated with coupling to a quadrupolar S-spin can be expressed in terms of the expectation values of $\hat{S}_z$ and $\hat{S}_x$:

$$\Delta \nu_i = (R_{DD} - \Delta J/3)[(3\cos^2\theta - 1) \langle \hat{S}_z \rangle_i + 3\sin\theta\cos\theta \langle \hat{S}_x \rangle_i] - J_{iso} \langle \hat{S}_z \rangle_i \tag{75}$$

$$\langle \hat{S}_z \rangle_i = \langle \varphi'_i | \hat{S}_z | \varphi'_i \rangle = \sum_k m_S a_{ik}^2 \tag{76}$$

$$\langle \hat{S}_x \rangle_i = \langle \varphi'_i | \hat{S}_x | \varphi'_i \rangle$$

$$= \sum_k \{[S(S + 1) - m_S(m_S + 1)]^{1/2} a_{i,k+1} a_{ik} \tag{77}$$

$$+ [S(S + 1) - m_S(m_S - 1)]^{1/2} a_{i,k-1} a_{ik}\}$$

where R_{DD} and ΔJ are defined in equations (24) and (23). Expression (75) is derived from the dipolar Hamiltonian operator in equation (56), the formal difference being that this development is restricted to the case where the dipolar vector coincides with the unique component of an axially symmetric field gradient, thus the common usage of θ to specify the orientation.

3.2 Applications

3.2.1 Copper Phosphines

Many solid copper(I) phosphine complexes have been examined by ^{31}P cross-polarization magic-angle spinning (CP/MAS) NMR spectroscopy (*45,46,49,136,137,138,139*). Common to all such spectra are peak patterns distorted with respect to the quartet expected from pure *J*-coupling to a spin-3/2 $^{63/65}$Cu nucleus. The origin of this phenomenon has been thoroughly investigated and shown to arise from spin-spin coupling to a quadrupolar nucleus possessing a quadrupolar interaction which is not negligible relative to its Zeeman interaction (*37,41,45,46,47,49,140,141*). Such spin-spin interactions are incompletely averaged under magic-angle spinning, and introduce field-dependent spectral distortions. The complete lineshape analysis in these cases can be complicated, relying on the magnitudes and relative orientation of the electric field gradient and dipolar coupling tensors. In principle, this multivariate dependence offers information on the coupled quadrupolar nucleus not normally available from NMR studies of spin-1/2 nuclei; practically, however, this complexity usually necessitates an estimate or assumption about the molecular structure or symmetry.

Although the general theory relating to this work has been discussed in section 3.1, it is important to highlight some properties of the various energy interactions pertinent to this investigation. Considering an isolated "spin pair" comprising the spin-1/2 nucleus (*I*) under NMR observation and a neighbouring quadrupolar nucleus (*S*), the total Hamiltonian operator can be written as the sum of the constituent Hamiltonians:

$$\mathcal{H} = \mathcal{H}_{Z(I)} + \mathcal{H}_{Z(S)} + \mathcal{H}_{Q(S)} + \mathcal{H}_{D(IS)} + \mathcal{H}_{J(IS)} \quad . \tag{78}$$

The first two terms, $\mathcal{H}_{Z(I)}$ and $\mathcal{H}_{Z(S)}$, represent the combined shielding-Zeeman Hamiltonian operators, accounting for the interaction of *I* and *S* with the applied magnetic field. The interaction of the quadrupolar nucleus with the electric field gradient is represented by $\mathcal{H}_{Q(S)}$. $\mathcal{H}_{D(IS)}$ and $\mathcal{H}_{J(IS)}$ are the direct dipolar and indirect

spin-spin coupling interactions. The EFG is not, in general, axially symmetric, and its orientation in the molecular frame is unknown *a priori*. Likewise, the indirect spin-spin coupling interaction is generally non-axially symmetric, and its orientation is also unknown. The direct dipole-dipole coupling interaction, on the other hand, *is* axially symmetric, and (ignoring motional effects) is known to be situated with the unique component along the internuclear vector, r_{IS}. In general, therefore, the most rigorous analysis must consider two components for the (traceless) EFG tensor, three principal components for the J tensor and a dipolar coupling constant, *as well as* two sets of Euler angles describing the relative orientations of these three interactions. Clearly, the superposition of multiple spin interactions with general orientation-dependences can generate a convoluted scenario for the spectroscopist.

Given the complexity of this situation, it is no wonder that a few basic assumptions are often invoked to render the problem tractable. It is plausible, for example, that the J tensor is axially symmetric, with its unique component directed along the internuclear vector. Under this condition, the tensors associated with $\mathcal{H}_{D(IS)}$ and $\mathcal{H}_{J(IS)}$ are coincident and can be described by three parameters: the direct dipole-dipole coupling constant, R_{DD}, and the isotropic and anisotropic contributions to the indirect spin-spin coupling tensor, J_{iso} and ΔJ. Further simplifications result from assumptions about $\mathcal{H}_{Q(S)}$: if the EFG tensor is known to be both axially symmetric and along r_{IS}, then it is characterized by the quadrupole coupling constant, C_Q, the asymmetry parameter being zero. Consequently, the original 10-variable problem reduces to a problem in four variables. Faced with a typical experimental situation, it may be tempting to blindly introduce these assumptions in order to obtain at least something of interest from the spectral analysis, but it is important to expose the assumptions to which a model is subject, and to consider whether these are, in fact, valid. Fortunately, many practical circumstances are encountered in which symmetry arguments justify some of these simplifications.

As a case in point, attempts have been made to identify anisotropy in $^1J(^{31}P,^{63/65}Cu)$ by analyses of ^{31}P NMR spectra (*45,46,47,142*). Lacking independent

knowledge of the EFG at the copper nucleus and ^{31}P,$^{63/65}$Cu dipolar coupling constants, some workers have assumed an axially symmetric EFG tensor which is coincident with the dipolar tensor. In still other cases, a *particular* value of ΔJ has been chosen and fixed, in order to obtain other parameters of interest (*46,142*). While these assumptions may indeed be justified in certain cases, it is curious that no reports of $\Delta^1 J(^{31}$P,$^{63/65}$Cu) have appeared in which the local symmetry and structure are known to support the theoretical model. This section reports ^{31}P NMR spectra of spinning and non-spinning powder samples of two bis(tribenzylphosphine)cuprate(I) salts, [(PBz$_3$)$_2$Cu][CuBr$_2$] (1) and [(PBz$_3$)$_2$Cu][PF$_6$] (2), which exhibit a two-coordinate, linear P–Cu–P geometry (*143,144*). In 1, a three-fold rotation axis coincides with the P–Cu–P bond, thereby guaranteeing axial symmetry of the interaction tensors. By contrast, this rotational axis is lost in 2 due to minor distortions of the benzyl groups, leaving only the inversion centre at the copper nucleus. In combination with zero-field $^{63/65}$Cu NQR data, lineshape calculations present a convincing demonstration of a substantial anisotropic component in the ^{31}P, $^{63/65}$Cu J tensor. Also examined are the more typical trimethoxyphenylphosphine copper(I) halides, which possess *nearly* linear P–Cu–X bonds (*145, 146*). For these systems, the abovementioned assumptions are no longer strictly valid, and it is instructive to subject them to the same treatment as a test of the sensitivity of these calculations to symmetry.

Experimental

Sample Preparation and Characterization. All tribenzylphosphine compounds were synthesized and characterized by Dr. E. W. Ainscough and Dr. A. M. Brodie at the Institute of Fundamental Sciences, Massey University in New Zealand. $[(PBz_3)_2Cu][CuBr_2]$, **1**, (Bz = benzyl) was prepared according to the literature method of Akrivos et al. (*143*). The synthesis of $[(PBz_3)_2Cu][PF_6]$, **2**, more fully described in reference *144*, involved the addition of solid tribenzylphosphine to a solution of $[Cu(CH_3CN)_4][PF_6]$ in dichloromethane/ethanol (1:1) under nitrogen atmosphere. This reaction mixture was heated under reflux for five minutes and allowed to stand at room temperature for one hour, whereupon colourless crystals of **2** were filtered, washed with ice-cold ethanol and dried *in vacuo*. The single-crystal X-ray structures of **1** (*143*) and **2** (*144*) confirm that these complexes possess discrete $[(PBz_3)_2Cu]^+$ cations with linear, two-coordinate P–Cu–P local environments for the Cu(I) atom. In both complexes, the copper atom of the cation is located on a centre of symmetry such that the P–Cu–P angle is exactly 180° and the two ligands are staggered. In **1**, the P–Cu–P axis lies on a three-fold crystallographic symmetry axis, generating C_3 symmetry for the ligands and S_6 symmetry for the cation; the entire system crystallizes in the $R\bar{3}$ space group (*143*). In **2**, the three-fold symmetry axis along P–Cu–P is perturbed, as the F(3) and F(3′) atoms of the $[PF_6]^-$ anion interact with the *ortho* hydrogens of one phenyl group on each of the PBz_3 ligands; this system crystallizes in the $C2/c$ space group (*144*). Preparation and characterization of the trimethoxyphenylphosphine (TMPP) complexes, [(TMPP)CuX] (X = Cl (**3**), Br (**4**), I (**5**)) and $[(TMPP)_2Cu][ClO_4]$, was performed by members of Professor Peter Healy's research group at the School of Science, Griffith University in Australia, and has been previously described (*145,146*).

Copper-63/65 Nuclear Quadrupole Resonance Spectroscopy. All NQR experiments were carried out by Mr. John Hanna at the CSIRO North Ryde NMR Laboratory in Australia. Quadrupole frequencies of [63]Cu and [65]Cu were obtained at ambient temperature using a Bruker CXP console pulsing into a probe arrangement

that was well-removed from the magnet (> 5 m) and shielded from extraneous magnetic and radiofrequency interference by a mumetal container. Solid-echo experiments with extended phase cycles (147) to eliminate baseline distortions and echo tails were employed in these measurements, using hard pulses of 2 μs duration and recycle delays of 0.5 s. The quadrupole frequency range scanned was determined from previous NQR studies of Cu(I) systems (134). The location of both ^{63}Cu and ^{65}Cu isotope resonances (related by the ratio $\nu_Q(^{63}Cu)/\nu_Q(^{65}Cu) = 1.081$) verified that true copper NQR frequencies were being observed. For [(PBz$_3$)$_2$Cu][CuBr$_2$], the NQR frequencies for the [CuBr$_2$]$^-$ anion were measured and proved to be well-separated from the cationic P–Cu–P core of interest. The values reported for [CuBr$_2$]$^-$ are in close agreement with previous $^{63/65}$Cu NQR studies involving this anion (148).

^{31}P Nuclear Magnetic Resonance Spectroscopy. Phosphorus-31 CP/MAS spectra were acquired at three fields using Bruker CXP-90 (North Ryde NMR Laboratory), MSL-200, MSL-400 (North Ryde NMR Laboratory) and AMX-400 spectrometers operating at 36.44, 81.03 and 161.98 MHz, respectively. Samples were packed into 4 mm or 7 mm zirconia rotors and all spectra were collected at 298 K. Chemical shifts are reported relative to 85% H$_3$PO$_4$(aq). Standard cross-polarization schemes were used, typically employing proton 90° pulses of 3.5 μs and contact times of 10 ms, with 60 s recycle delays. For MAS spectra, data tables of 2 K points were acquired and zero-filled to 4 K prior to exponential multiplication with 30 Hz Lorentzian line-broadening and Fourier transformation. Spectra of stationary samples typically involved the acquisition of 1 K points, 2× zero-filling, and exponential multiplication of 100 Hz, prior to Fourier transformation. The spectral width ranged from 50 to 80 kHz.

In order to establish meaningful comparisons between experimental and calculated MAS lineshapes, it is necessary to construct an "isotropic MAS powder spectrum" by adding the spinning sidebands (ssbs) to the centreband (113). For spectra collected at 9.4 T, this was achieved by summing the minor intensity ($< 5\%$)

located in the ± 1 order ssbs, well-separated from the centreband. At 4.7 T, however, the rotation rate was insufficient to fully separate the ssbs from the centreband, and consequently, intensity from first-order ssbs was interleaved between centreband peaks. Summation of the ± 1 and ± 2 ssbs in this case therefore, yielded peak artifacts which, though unsightly, do not interfere with the spectral analysis; these have been artificially removed for aesthetic purposes. In MAS spectra acquired at 2.1 T, spinning sidebands overlap with peaks from the centreband, and it was impossible to generate an "isotropic MAS powder spectrum". Although these constitute a small percentage of the total signal intensity ($<$ 10%), this spectral overlap is probably responsible for minor discrepencies observed between calculated and experimental spectra at this field (see Figure 23).

NMR Spectral Calculations. Calculations of the ^{31}P NMR lineshapes utilized WSolids and QUADSPIN, both C programs developed in this laboratory incorporating full-matrix diagonalization of the Zeeman-quadrupolar Hamiltonian for the dipolar-coupled quadrupolar nucleus (38c). For calculating spectra of stationary powder samples, the formal A_2X spin system was treated as an AX system, since incorporation of the small ^{31}P,^{31}P dipolar coupling constant (230 Hz) simply introduced additional broadening of the peaks. Powder averaging was performed using the POWDER algorithm (116).

Results and Discussion

The ^{31}P CP/MAS spectra of compounds 1 and 2 obtained at 2.1, 4.7 and 9.4 T are presented, along with the best-fit calculations, in Figure 23. The excellent agreement observed in these figures was achieved by employing full-matrix diagonalization of the $^{63/65}Cu$ Zeeman-quadrupolar Hamiltonian. Attempts to reproduce the experimental data using an approach based on first-order perturbation theory failed, implying that the magnitude of the quadrupole interaction is too large to be considered simply a perturbation on the Zeeman wavefunctions. Indeed, the strong field-dependence exhibited in Figure 23 reflects the importance of the relative magnitudes of the Zeeman and quadrupolar interactions in determining spectral appearance. The ratio, $\nu_Q(^{65}Cu)/\nu_L(^{65}Cu)$, for example, ranges from 0.4 to 1.8 on going from 9.4 T to 2.1 T, with the associated lineshapes becoming correspondingly more distorted from the purely "high-field" case of a quartet with equal splittings of $^1J(^{31}P,^{65}Cu)$.

Spin-1/2 lineshape calculations involving coupled quadrupolar nuclei are influenced by the magnitude of the EFG tensor and its orientation with respect to the dipolar tensor. In the most general case, this necessitates knowledge of C_Q, η, and the angles orienting the dipolar vector in the EFG principal axis system. Clearly, this information can be hard to obtain, and in many applications, assumptions are invoked to make lineshape calculations possible (*vide supra*). The attractiveness of compound 1 is that single-crystal X-ray diffraction results indicate a perfectly linear P—Cu—P centre, located on a three-fold rotation axis with an accompanying inversion centre at the copper nucleus (*143*). This symmetry arrangement requires that the copper EFG tensor be axially symmetric, with the largest component directed along the P—Cu bond. Since the dipolar vector is always understood to be collinear with the internuclear axis, the dipolar and EFG tensors are coincident. In addition, this symmetry guarantees that the J tensor is axially symmetric with the unique axis being along $r_{P,Cu}$ (*149*). As such, many of the assumptions commonly made to render lineshape calculations tractable are justified in this case.
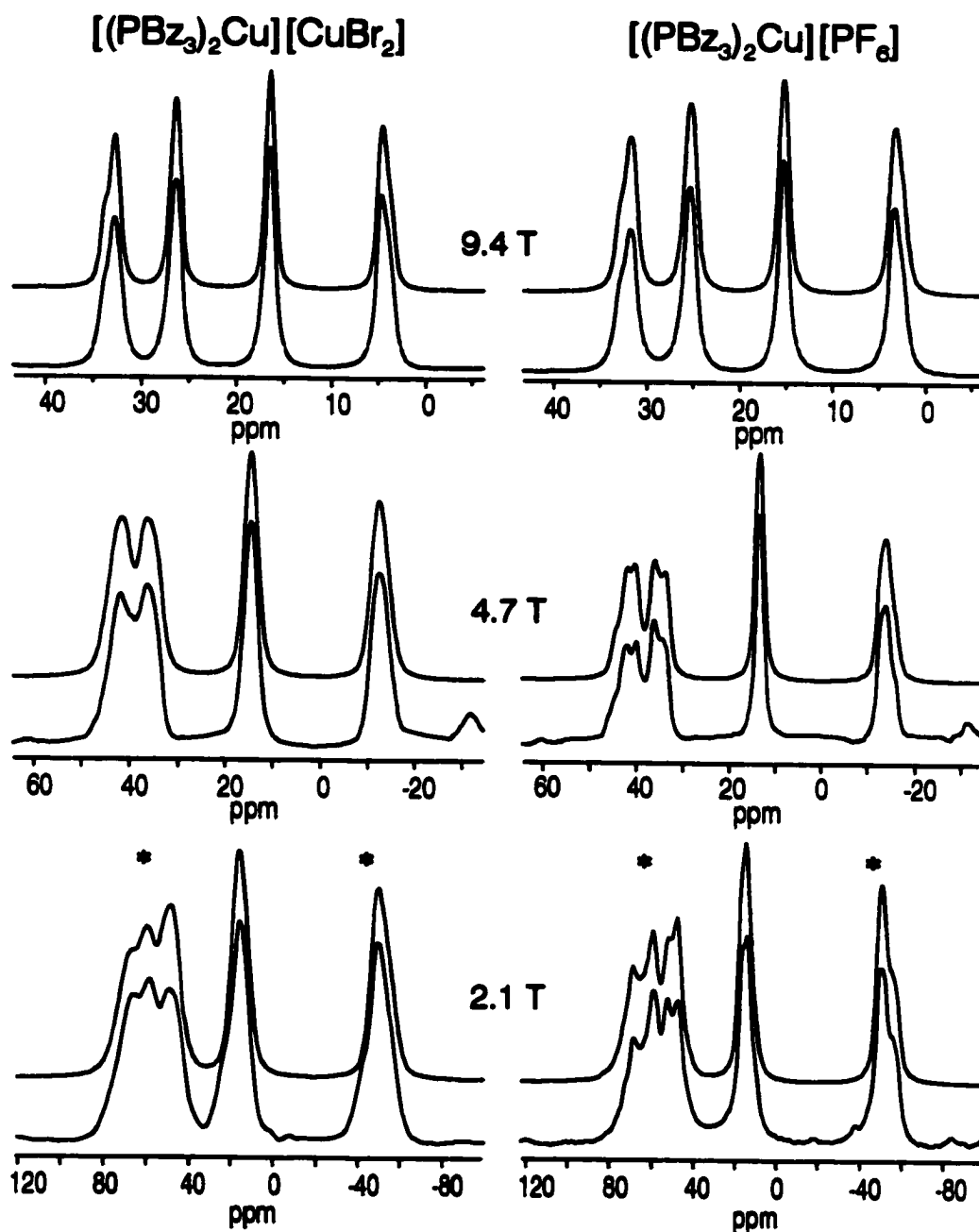
Figure 23   Phosphorus-31 CP/MAS spectra of the phosphine resonance in 1 and 2.
Top traces are calculated, bottom traces are experimental; see Table 5
for fitting parameters. Each displayed spectral region spans 8 kHz.
Rotation rates: 10,000 Hz, 3,000 Hz and 3800 Hz for 9.4, 4.7 and 2.1
T, respectively. Number of transients: 1724, 138, 1428 for
[(PBz$_3$)$_2$Cu][CuBr$_2$], and 2248, 60, 6740 for [(PBz$_3$)$_2$Cu][PF$_6$], for
9.4, 4.7 and 2.1 T, respectively. Regions containing overlapping
spinning sidebands are marked with asterisks (see Experimental
section).

Moreover, axial symmetry in the EFG tensor justifies the use of NQR spectroscopy to determine independently the quadrupole coupling constants. For a spin-3/2 nucleus subject to an axially symmetric EFG, $|C_Q|$ is simply twice the measured quadrupole frequency, ν_Q. These values, given in Table 5, are 84.6 and 78.3 MHz for the ^{63}Cu and ^{65}Cu isotopes of 1. These couplings appear to be the largest reported for copper(I) phosphine complexes (134,148), and their magnitudes are reflected in the marked field-dependence demonstrated by the ^{31}P CP/MAS spectra of Figure 23. On the basis of the X-ray diffraction and NQR data, all the relevant information regarding the $^{63/65}$Cu EFG tensors, except for the sign of C_Q, is provided at the outset, thereby eliminating the need for approximations.

Since X-ray crystallography also provides bond lengths, the P—Cu dipolar coupling constant, R_{DD}, can be calculated according to

$$R_{DD}(^{31}P,{}^{63}Cu) = \left(\frac{\mu_0}{4\pi}\right)\left(\frac{\hbar}{2\pi}\right)\gamma(^{31}P)\,\gamma(^{63}Cu)\,\langle r_{P,Cu}^{-3}\rangle \tag{79}$$

where $<r^{-3}_{P,Cu}>$ represents a time average over the internuclear distance cubed. This leaves only the isotropic ^{31}P chemical shift and the J tensor as variable parameters in the fitting procedure. Due to this orientation-dependence being identical to that of the *direct* dipolar interaction, an *effective* dipolar coupling constant is usually defined which incorporates the effects of this anisotropy (150):

$$R_{eff} = R_{DD} - \Delta J/3 \ . \tag{80}$$

In practice, it is impossible to separate these two contributions, with the consequence that the dipolar coupling constant measured in solid state NMR experiments is always R_{eff}. This can be used to advantage if one is interested in determining ΔJ, as in the present case: since R_{DD} is known independently, the difference between R_{eff} and R_{DD} yields $\Delta J/3$.

In the NMR spectral analysis of 1, the ^{31}P CP/MAS lineshapes could not be

Table 5   Nuclear magnetic and quadrupole resonance data for the bis(tribenzylphosphine)cuprate complexes, 1 and 2

	$[(PBz_3)_2Cu][CuBr_2]$	$[(PBz_3)_2Cu][PF_6]$
$\delta_\perp$ /ppm[a,b]	$+40.6 \pm 0.2$	$+38.4 \pm 0.2$
$\delta_\parallel$ /ppm[a,b]	-21.2 ± 0.2	-20.6 ± 0.2
δ_{iso} /ppm[a,c]	$+19.8 \pm 0.2$	$+18.9 \pm 0.2$
$R_{DD}(^{31}P,^{63}Cu)/Hz$[d,e]	$+1223$	$+1230$
$^1J_{iso}(^{31}P,^{63}Cu)/Hz$[d,f]	$+1535 \pm 10$	$+1550 \pm 10$
$^1J_\parallel(^{31}P,^{63}Cu)/Hz$[d,f]	$+2035 \pm 50$	$+2030 \pm 50$
$^1J_\perp(^{31}P,^{63}Cu)/Hz$[d,f]	$+1285 \pm 50$	$+1310 \pm 50$
$C_Q(^{63}Cu)/MHz$[g]	$+84.60 \pm 0.01$ 57.06 ± 0.01[h]	$+82.96 \pm 0.01$
$C_Q(^{65}Cu)/MHz$[g]	$+78.30 \pm 0.01$ 52.80 ± 0.01[h]	$+76.76 \pm 0.01$

[a] ^{31}P chemical shifts, relative to external 85% H_3PO_4(aq)

[b] obtained from ^{31}P CP NMR of stationary powder samples

[c] obtained from ^{31}P CP/MAS

[d] parameters for $^{31}P,^{65}Cu$ spin pairs were varied according to their relative magnetogyric ratios, e.g. $^1J(^{31}P,^{65}Cu)/^1J(^{31}P,^{63}Cu) = 1.071$

[e] dipolar coupling constants, calculated from known values of $r_{P,Cu}$

[f] spin-spin coupling parameters, determined from ^{31}P CP/MAS

[g] nuclear quadrupole coupling constants, magnitudes obtained from NQR

[h] nuclear quadrupole coupling constants, obtained from NQR for the linear $[Br-Cu-Br]^-$ anion

reproduced without introducing a sizeable, positive ΔJ. Figure 24 depicts simulated spectra at 4.7 T with no J anisotropy, and with positive and negative values of ΔJ. By comparison with Figure 23, it is clear that only the spectrum calculated using $\Delta^1 J(^{31}P,^{63}Cu) = +720$ Hz agrees with the experimental spectrum.[2] That the same parameters accurately fit ^{31}P CP/MAS spectra at three applied fields serves to corroborate this conclusion (see Table 5). Under the conditions of first-order perturbation theory, multiple field data may only make the phenomenon more or less apparent, but offer no *new* information since the parameters are linearly correlated with the applied field strength. On the other hand, where the quadrupole and Zeeman interactions are of comparable magnitude and the full-matrix diagonalization method is used, analyses of NMR spectra collected at different fields enhances confidence in the NMR parameters obtained therefrom.

Information regarding the anisotropic ^{31}P chemical shielding is available from cross-polarization spectra of non-spinning samples (Figure 25). Again utilizing the symmetry constraints provided by X-ray diffraction to guarantee an axially symmetric shielding tensor in 1, lineshape calculations yield the following components:

$\delta_\perp = +40.6$ ppm and $\delta_\parallel = -21.2$ ppm (Table 5). Shielding anisotropy is indicated by the span of the tensor, $\Omega = \delta_\perp - \delta_\parallel = 62$ ppm, with the largest shielding effects observed when the P–Cu–P core is aligned with the applied magnetic field. Although ^{31}P shielding anisotropies have been determined for many transition metal phosphine complexes, there are very few examples involving group 11 metals (151). In fact, this appears to be the first report of ^{31}P chemical shift tensor components in a copper(I) phosphine complex. Qualitatively, the span of the chemical shielding tensor in 1 is significantly smaller than those generally observed in phosphine complexes of transition metals from groups 6 to 10 (152), but is comparable to those of mercury phosphine complexes (153) and free phosphine ligands (154).

---

[2]All simulated spectra include coupling effects to both spin-active copper nuclei according to the ratio of their respective natural abundance, $^{63}Cu/^{65}Cu = 69.1/30.9$. Dipolar and J-couplings were varied according to their relative magnetogyric ratios, $\gamma(^{63}Cu)/\gamma(^{65}Cu) = 0.93353$.
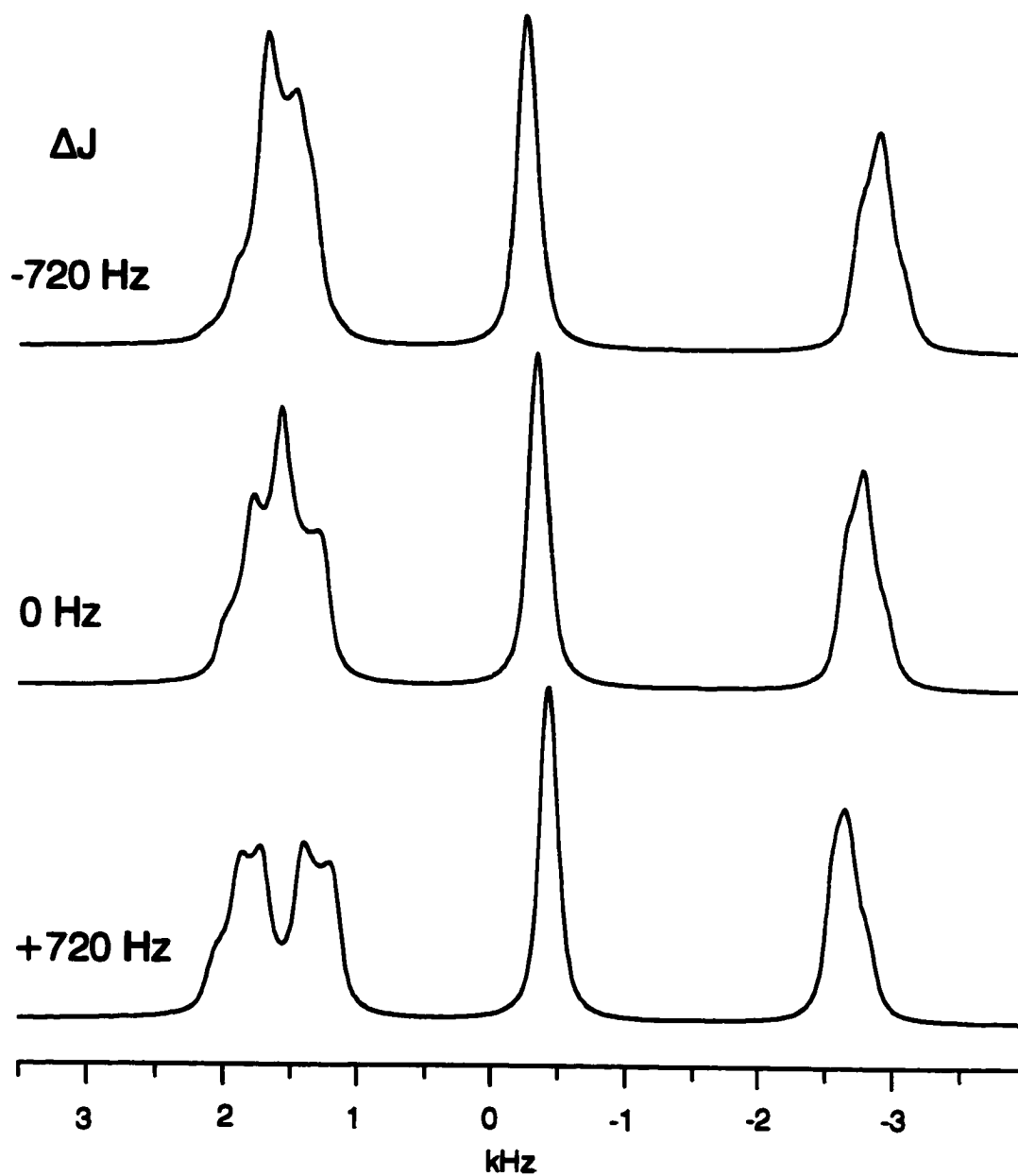
Figure 24   Sensitivity of ^{31}P MAS calculations to the sign and magnitude of $\Delta^1 J(^{31}P,^{63/65}Cu)$ for 2 at 4.7 T. Other simulation parameters can be found in Table 5.
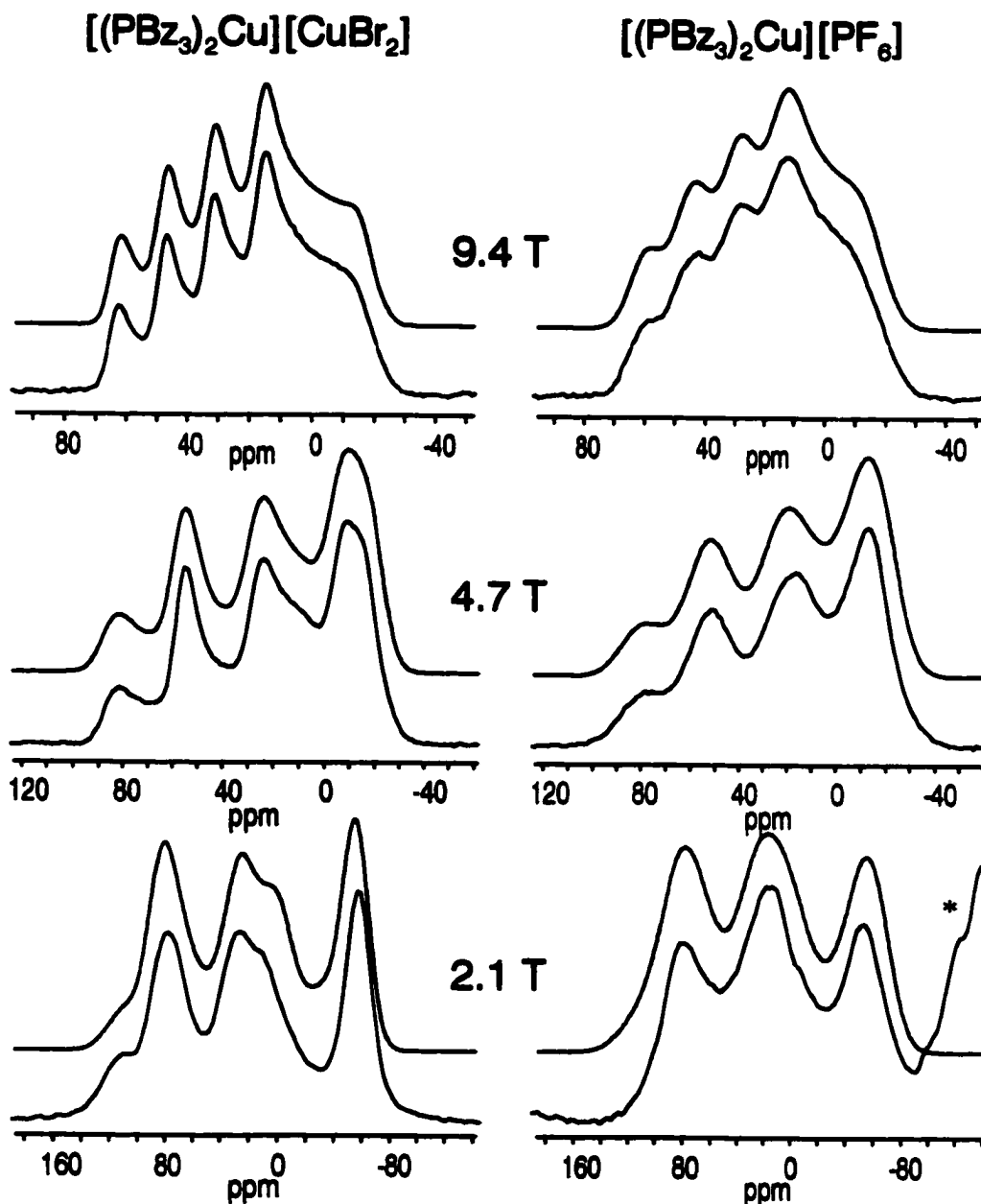
Figure 25   Phosphorus-31 CP NMR spectra of the phosphine resonance in
stationary samples of 1 and 2. Experimental spectra are the bottom
traces and calculated spectra, the top traces; see Table 5 for fitting
parameters. Spectra collected at 9.4 and 4.7 T result from between
200 and 300 transients, whereas spectra at 2.1 T are from the
coaddition of 11,400 transients. A portion of the hexafluorophosphate
resonance in the 2.1 T spectrum of [(PBz$_3$)$_2$Cu][PF$_6$] is indicated by an
asterisk.

A second bis(tribenzylphosphine)cuprate, [(PBz$_3$)$_2$Cu][PF$_6$], (2) was also investigated by these means. The crystal belongs to the space group C2/c (*144*). This symmetry guarantees that the copper in any given cation is situated on a centre of inversion, consequently ensuring that the P–Cu–P bond angle is 180°, and that the two phosphorus nuclei are magnetically equivalent. However, the crystal symmetry *does not* demand that the EFG tensor at the Cu(I) site is axially symmetric, nor does it dictate that the unique components of the direct and indirect spin-spin coupling tensors be coincident (*149*). A further implication of the lowered symmetry is that the ^{31}P NMR analysis of non-spinning samples cannot rely on the assumption that the phosphorus shielding tensors are exactly axially symmetric. The local environment about the phosphorus is distorted somewhat from the perfect three-fold rotational symmetry of 1; the Cu–P–C bond angles are 110.5°, 114.0° and 115.6° (*144*).

In spite of these qualifications, excellent simulations of the ^{31}P NMR spectra of magic-angle spinning (Figure 23) and non-spinning (Figure 25) samples of 2 could be obtained by invoking the above assumptions. Moreover, the spectral parameters are very similar to those obtained for 1 (Table 5). Nevertheless, without having carefully examined compound 1, for which symmetry-dictated tensor orientations can be relied upon, it would be impossible to have any confidence in the J(^{31}P,$^{63/65}$Cu) anisotropy obtained for 2. A clear message emerging from this work is that the reliable characterization of anisotropic J tensors in powder samples depends critically on sufficiently high crystal symmetry.

An unique feature of these spectral analyses is that relative sign information is available from the "exact" calculations. Given that one-bond reduced coupling constants (*155*) between ^{31}P and transition metals are known to be positive (*156*), only positive values of C_Q and R_{eff} reproduce the experimental spectra. A positive nuclear quadrupole coupling constant is consistent with sign predictions for linear "sp-hybridized" atoms based on symmetry and hybridization considerations (*46b,157*), as well as with microwave spectroscopic measurements in copper(I) halides (*158,159*). Since the magnetogyric ratios, $\gamma(^{31}$P) and $\gamma(^{63/65}$Cu), possess the same sign, R_{DD}

must also be positive. A positive value of R_{eff} then, demands that $\Delta J/3$ be smaller than R_{DD}, a criterion satisfied by the values listed in Table 5. In fact, two sets of parameters produce identical spectra, the second involving the corresponding *negative* quantities for C_Q, J_{iso} and R_{eff}. Were this latter solution valid, the J anisotropy would have to be +6588 Hz in 1 to yield R_{eff} = -973 Hz!

It is worth emphasizing that what emerge from this type of analysis are the *relative* signs of C_Q, J_{iso} and R_{eff} (47,37). Unless one of these is known *a priori*, it is not possible to distinguish absolutely between these two solutions. Early calculations by Menger and Veeman claiming to have determined the *absolute* sign of $^1J(^{31}P, ^{63}Cu)$ were based on purely isotropic J-coupling, (i.e. R_{eff} = R_{DD} > 0), thereby inadvertently overlooking the possibility of a *negative* effective dipolar coupling constant (49). Subsequent workers have elected instead to assume the sign of C_Q in order to determine the sign of J_{iso} (47). An alternate approach, as employed here, is to accept the positive sign of the reduced coupling constant, $^1K(P,Cu)$ (155), as a reference for the other signs. Although the end result is the same in this case, it is important to have a clear understanding of what is actually *known* in order to avoid circular reasoning.

If internuclear distances were not known independently, one might be tempted to use the effective dipolar coupling constant in the calculation of $r_{P,Cu}$, *i.e.*, assuming purely isotropic J-coupling. In the present cases, this would result in an overestimation of the bond length. Specifically, the actual phosphorus–copper bond length in $[(PBz_3)_2Cu][CuBr_2]$ is 2.1955(14) Å, yielding $R_{DD}(^{31}P, ^{63}Cu)$ = +1223 Hz (143). Accounting for $\Delta^1J(^{31}P, ^{63}Cu)$ = +750(50) Hz, the effective dipolar coupling constant is 972 Hz, leading to an *apparent* $r_{P,Cu}$ of 2.37 Å. Similarly for $[(PBz_3)_2Cu][PF_6]$, $r_{P,Cu}$ = 2.1909(14) Å from crystallography (144), whereas the NMR result neglecting the contribution of ΔJ is 2.36 Å. In each case, a naive interpretation of the solid state NMR spectra would indicate bond lengths 8% *longer* than those determined from X-ray crystallography. Clearly, this observation underscores the importance of considering whether anisotropic J-coupling may be

operative in the analysis and subsequent interpretation of solid-state NMR spectra (*39*).

It is necessary to point out that the comparison of bond lengths obtained from solid state NMR and diffraction techniques is subject to some qualifications. In particular, the measurement of dipolar couplings depends on the vibrationally averaged value $<r^{-3}>$, so that the internuclear distances derived therefrom are actually $(<r^{-3}>)^{-1/3}$. Diffraction techniques, by contrast, measure the time average $<r>$. It is well-known, therefore, that molecular libration decreases the observed dipole coupling constant, thereby *increasing* the apparent bond length (*160*). Could motional averaging masquerade as indirect spin-spin coupling anisotropy? Recent research utilizing theoretical calculations and molecular dynamics simulations to assess vibrational effects on internuclear distances obtained from solid state NMR concluded that for directly bonded nonproton nuclei in glycine, molecular librations are responsible for a 2 – 3% increase in bond lengths with respect to those obtained from single crystal diffraction techniques (*160c*). The same study suggests that intramolecular vibrations induce negligible changes between nonproton nuclei. On the basis of these results, it is highly unlikely that motional effects are fully responsible for the observed 8% increase in the P–Cu bond length; ΔJ must be operative.

The existence of anisotropic *J*-coupling in metal phosphines has been thoroughly discussed in the literature (*37,153,161,162*), and is understood to imply that mechanisms other than the orientation-*independent* Fermi contact term play a significant role in indirect spin-spin coupling. In view of this, it is not surprising that schemes correlating $^1J(^{31}P,^{63}Cu)$ with the number of bound phosphine ligands (*163*) fail in the present case, as they are implicitly based on the dominance of the Fermi contact mechanism. Whereas this assumption appears to be valid for first-row elements such as ^{13}C and ^1H, its extension to heavier elements is dubious given the results contained herein.

In light of these conclusions, it is interesting to examine by ^{31}P CP/MAS a series of related copper phosphines which lack the symmetry characteristics required

to justify the assumptions outlined above. In the [(TMPP)CuX] solids
(X = Cl, Br, I), X-ray diffraction indicates that the P–Cu–X bond angles approach
linearity – 172.97(6)°, 172.00(9)°, 171.0(1)° (*145,146*) – and obviously have no
rotation axis along the P–Cu bond. NQR yields values of $\nu_Q(^{63}Cu)$ of 32.95, 31.64
and 30.58 MHz; lacking axial symmetry, the asymmetry parameter is unknown *a
priori*. If a rather generous value of $\eta < 0.5$ is assumed, the quadrupole coupling
constant can be estimated to within 8%. However, the other simplifications cited
above are also not strictly valid: i.e., $J \parallel R \parallel V_{33}$. What happens to the lineshape
calculations in these cases if they are treated as axially symmetric?

Phosphorus-31 CP/MAS spectra were collected at 36.4 and 161.97 MHz for
three trimethoxyphenylphosphine cuprate(I) halides containing approximately linear
P–Cu–X centers (Figure 26, Figure 27, Figure 28). The isotropic regions of these
spectra were analyzed using full-matrix diagonalization under the assumption that the
$^{63/65}Cu$ EFGs are axially symmetric, with the largest component directed along the
Cu–P internuclear vector. Zero-field NQR measurements of the copper-63/65
quadrupole frequencies were interpreted under the assumption of axiality to yield
quadrupole coupling constants as twice ν_Q. Each calculation takes account of both
spin-active copper isotopes according to their respective natural abundance, and the
parameters J_{iso} and ΔJ were varied in compliance with their magnetogyric ratios,
$\gamma(^{65}Cu)/\gamma(^{63}Cu) = 1.071$. Held fixed in each simulation were experimentally
determined values of C_Q, and the dipolar coupling constants calculated from known
P–Cu internuclear separations. The parameters obtained from this exercise are
presented in Table 6.

Qualitatively, all simulations are in reasonable agreement with the
experimentally observed spectra. However, only the 9.4 T spectrum of
[(TMPP)CuBr] is an "exact" match, comparable to the bis(tribenzylphosphine)
cuprates. It did not prove possible to fit the 9.4 T spectra of the chloride or iodide
salts with the excellent agreement of the bromide or, for that matter, of the
bis(tribenzylphosphine)cuprates. In particular, a slight frequency mismatch in the
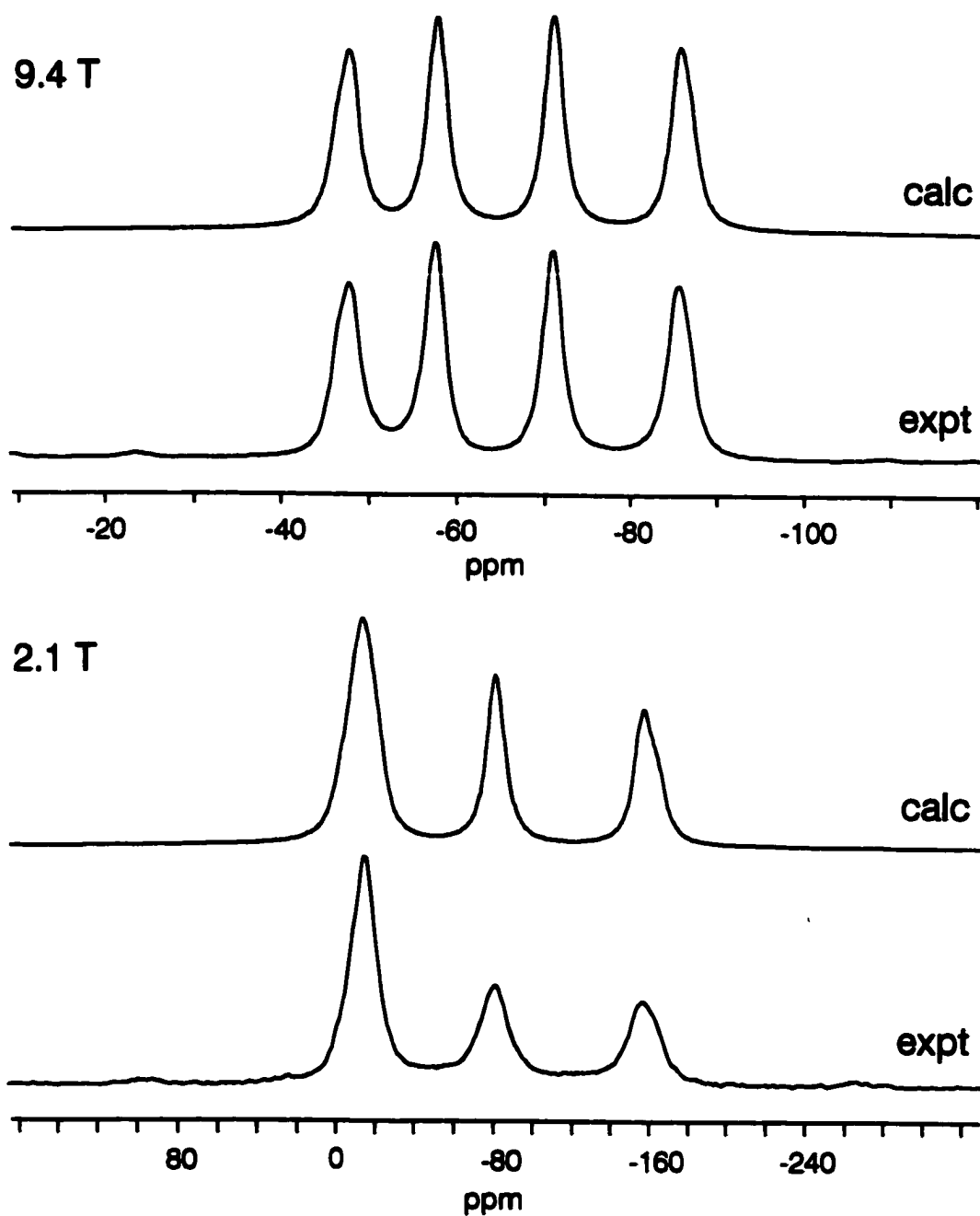
Figure 26   Phosphorus-31 CP/MAS spectra of [(TMPP)CuCl] at 2.1 and 9.4 T.
Experimental spectra result from 4544 transients with a sample rotation
rate of 4.0 kHz at 2.1 T, and 1154 transients at ν_r = 10.0 kHz at
9.4 T.
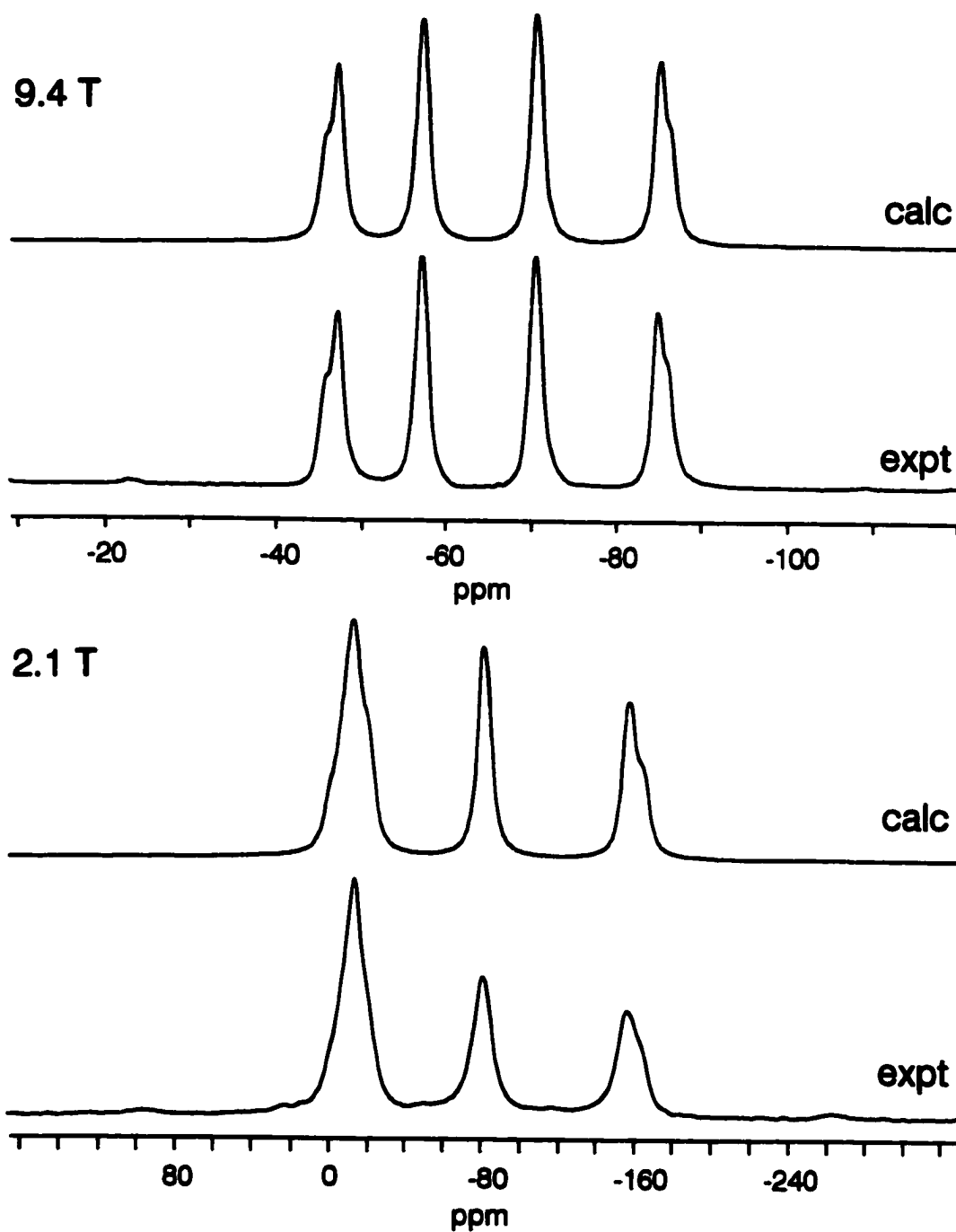
Figure 27   Phosphorus-31 CP/MAS spectra of [(TMPP)CuBr] at 2.1 and 9.4 T.
            Experimental spectra result from 7000 transients with a sample rotation
            rate of 4.0 kHz at 2.1 T, and 1574 transients at ν_r = 10.0 kHz at
            9.4 T.

9.4 T

calc

expt

-20   -40   -60   -80   -100

ppm

2.1 T

calc

expt

80   0   -80   -160   -240

ppm
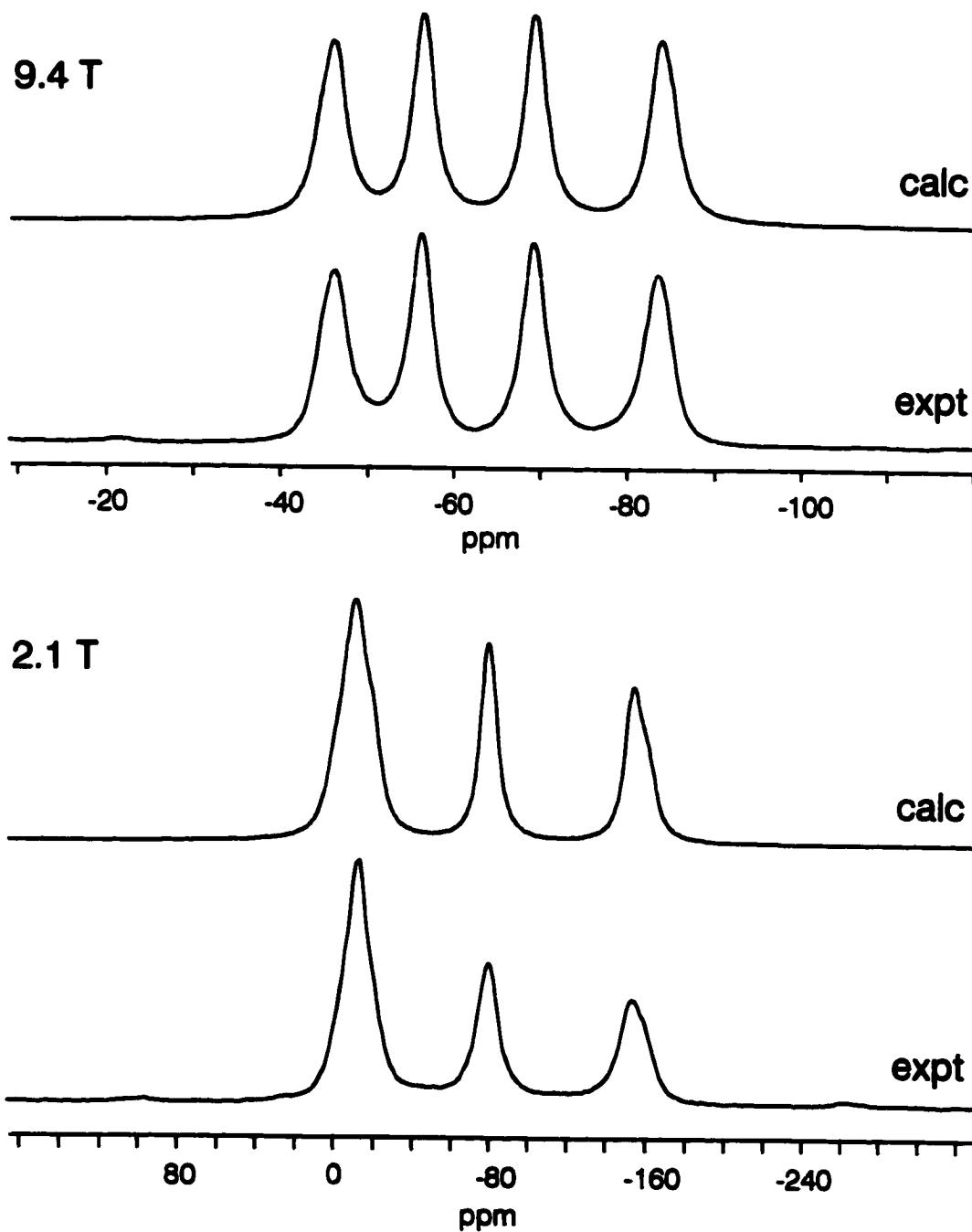
Figure 28   Phosphorus-31 CP/MAS spectra of [(TMPP)CuI] at 2.1 T and 9.4 T.
Experimental spectra result from 7056 transients with a sample rotation
rate of 4.0 kHz at 2.1 T, and 1742 transients at ν_r = 10.0 kHz at
9.4 T.

Table 6   Phosphorus-31 NMR parameters and related data for
trimethoxyphenylphosphine cuprate complexes

	3	4	5	6
$\delta_{iso}{}^a$	-66	-66	-64	-82
$R_{DD}(^{31}P,^{63}Cu)^{b,c}$	+1254	+1220	+1235	$(+1235)^f$
$^1J(^{31}P,^{63}Cu)^{c,d}$	+2060 ± 30	+2070 ± 20	+2030 ± 30	+1840 ± 40
$^1\Delta J(^{31}P,^{63}Cu)^{c,d}$	+700 ± 300	+600 ± 300	+700 ± 300	$(+900)^f$
$C_Q(^{63}Cu)^e$	+65.90	+63.28	+61.16	+69.54
$C_Q(^{65}Cu)^e$	+60.98	+58.56	+56.60	+64.36

a ^{31}P chemical shifts, in ppm, relative to external 85% H_3PO_4(aq); uncertainties estimated to be ± 1 ppm

b dipolar coupling constants, in Hz, calculated from known values of $r_{P,Cu}$ (except 6)

c parameters for $^{31}P,^{65}Cu$ spin pairs were varied according to their relative magnetogyric ratios, e.g. $^1J(^{31}P,^{65}Cu)/^1J(^{31}P,^{63}Cu)$ = 1.071

d spin-spin coupling parameters, in Hz, determined from ^{31}P CP/MAS

e nuclear quadrupole coupling constants, in MHz, magnitudes obtained by doubling quadrupole frequencies from NQR measurements (i.e. η = 0); signs from spectral calculations of ^{31}P MAS NMR; uncertainty estimated to be ± 0.01 MHz

f R_{eff} obtained from ^{31}P MAS lineshape calculations separated into approximate contributions from R_{DD} and ΔJ

outer peaks could not be reconciled. More vexing is the disagreement observed for the 2.11 T spectra of all three samples. In each case, a marginal improvement was realized by decreasing the isotropic J-coupling by a few percent, but even then, it was not possible to reproduce the relative intensities and broadenings of the peaks. While some of this discrepency might be reasonably attributed to spinning sidebands buried within the isotropic region, it is unlikely that this would account fully for the problem. Another unknown factor is the influence of copper-63/65 quadrupolar relaxation on the ^{31}P MAS peaks. Although relaxation in solids is not well understood, interesting effects attributed to ^{59}Co relaxation have been noted in ^{31}P MAS spectra of cobaloximes (*38d*). However, these effects are expected to modify only the widths and intensities of the peaks, and not their *positions*.

The observation that the theoretical fits deteriorate at lower fields suggests that the quadrupolar interaction is, at least partially responsible for the inconsistencies. With decreasing $\nu_L(^{63/65}$Cu$)$, the quadupolar interaction becomes more prominent in dictating the spin states and, consequently, the transition energies. The assumption of axial symmetry in the EFG tensor affects the magnitudes of all principal components – V_{11}, V_{22} and V_{33} – as well as their orientation with respect to **J**, **R** and **B$_0$**. The net effect of a slight deviation from axial symmetry may be significant and would manifest more clearly in the lower field ^{31}P NMR spectra.

Table 6 reports the NMR parameters and uncertainties derived from ^{31}P MAS spectra at 9.4 T. In spite of imperfect fits, the cited values of $^1J(^{63}$Cu,^{31}P$)$ are thought to be accurate and still quite precise ($< 2\%$). The errors associated with ΔJs, on the other hand, are quite large, a consequence of the difficulty encountered in obtaining good fits. In fact, the $\sim 50\%$ uncertainty in $\Delta^1J(^{63}$Cu,^{31}P$)$ may also contain reinforcement from errors in assuming $C_Q = 2\nu_Q$, since these factors contribute to the same frequency term in equation (75). (It is interesting to note that values of $C_Q(^{63}$Cu$)$ were estimated by Olivieri for the chloride and bromide salt to be $+69.8$ and $+62.4$ MHz, respectively (*46*). Even with rather severe assumptions – first-order perturbation theory, axial symmetry, arbitrarily chosen values of $\Delta J = +600$ Hz –

his estimates differ by only +6% and -1.4% from the NQR values!) In general, however, it is necessary to conclude that although isotropic Js may be reliably obtained for these compounds, precise values of ΔJ are not available from this analysis. By analogy with 1 and 2, it may be reasonably hypothesized that J tensors in 3 - 5 are anisotropic, but their full characterization remains tentative.

Finally, the perchlorate salt of bis(trimethoxyphenylphosphine)cuprate(I), 6, was examined by ^{31}P CP/MAS NMR and by NQR (Figure 29). In this case, however, the crystal structure has not yet been determined. On the basis of vibrational spectroscopy and the $^{63/65}$Cu quadrupole frequencies, a linear P–Cu–P core has been postulated (146). Accordingly, these spectra were analysed as above, under the assumption of axial symmetry. Lacking $r_{P,Cu}$, no information on ΔJ is available from the measured value of R_{eff}. (In Table 6, R_{eff} has been artificially separated into R_{DD} and ΔJ for convenience.) Qualitative agreement could be achieved between calculated and experimental spectra, with many of the same comments as for compounds 3 - 5. The inability to obtain spectral fits comparable to 1 and 2 suggests that the assumption of axial symmetry is invalid, and the P–Cu–P bond angle deviates from 180°.
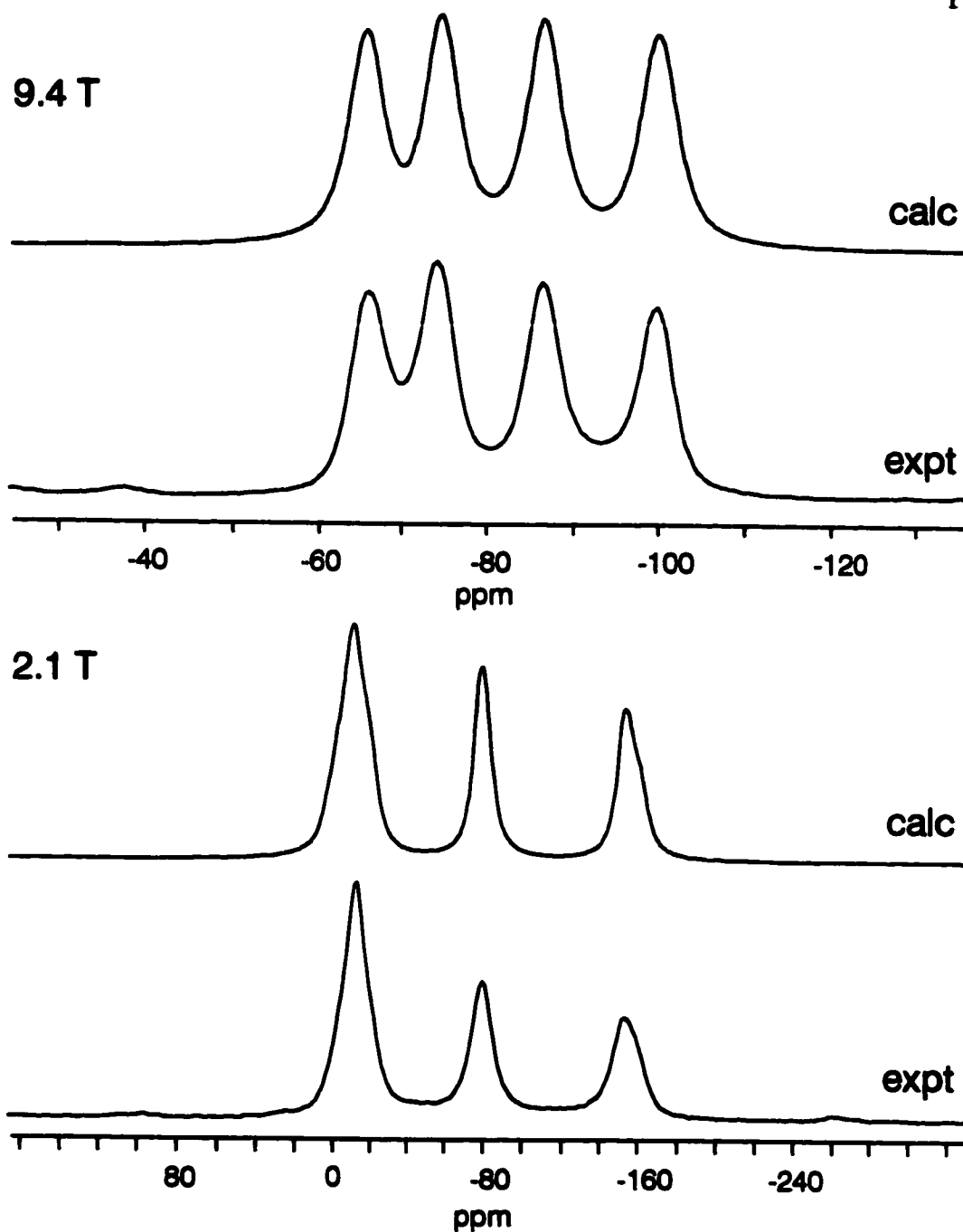
Figure 29   Phosphorus-31 CP/MAS spectra of [(TMPP)$_2$Cu][ClO$_4$] at 2.1 and
9.4 T. Experimental spectra result from 20132 transients with a
sample rotation rate of 4.0 kHz at 2.1 T, and 2032 transients at ν_r =
10.0 kHz at 9.4 T.

Conclusions

The analysis of ^{31}P NMR spectra of compound 1 is simplified by the space group symmetry which, when combined with single-crystal X-ray diffraction and powder NQR data, permits an unambiguous measurement of $\Delta^1 J(^{31}P,^{63/65}Cu)$. The corresponding analysis of 2, subject to the same assumptions, yields NMR parameters that are very close to those of 1, in spite of the loss of strict threefold symmetry. The spectral calculation of 2 can be considered successful only because it is accompanied by the parallel success of 1, for which the interaction tensors are completely determined by crystal symmetry. Though sometimes ignored, the contribution of ΔJ to the effective dipolar coupling constant can be substantial, and its neglect may yield misleading structural information. These results are in qualitative agreement with conclusions from previous studies which were based on questionable assumptions (*46*). Clearly it is of paramount importance to establish simple methods for understanding NMR spectra in terms of molecular structure, but it is difficult to overemphasize the need to maintain scientific rigour in the presentation of such schemes. The analysis of almost-linear copper phosphines, 3 – 6, demonstrates that although *qualitative* information may be derived by these methods, the deviation from sufficiently high symmetry may produce a significant mismatch between experiment and theory, preventing reliable characterizations of the full anisotropic *J* tensor. The potential utility of solid state NMR in structural characterization is not ultimately aided by "quick-and-dirty" spectral analyses which account insufficiently for the tensorial complexity of nuclear coupling interactions, but will be furthered only by detailed investigations of well-characterized molecular systems.

3.2.2 Copper Cyanide

Transition metal cyanides have a long and distinguished history in the chemical sciences. Prussian blue, $[Fe_4\{Fe(CN)_6\}_3] \cdot xH_2O$, for example, was the first reported coordination compound as early as 1704 (*164*), and the original Hofmann clathrate in 1897 (*165*), $Ni(NH_3)Ni(CN)_4 \cdot 2C_6H_6$, sparked a great deal of interest in inclusion compounds that endures even today (*166*). The obvious utility of cyanide as a bridging ligand has inspired a recent resurgence of interest in metal cyanides (*167*) for applications ranging from organometallic "zeolites" (*103,168*) to high-T_c molecular-based magnets (*169*). In addition to their usefulness in materials science, transition metal cyanides occupy a crucial place on the synthetic chemist's workbench due to diverse reactivity and wide-ranging catalytic properties (*170*).

Copper(I) cyanide, in particular, has enjoyed popularity amongst organic chemists due to its unique role in structural elaboration *via* cyano-Gilman chemistry (*171*). It has also shown promise in the construction of self-assembling zeolitic frameworks (*168a,b,172*) and as a precursor in the synthesis of $YBa_2Cu_3O_{7-x}$ superconductors (*173*). However, the structural characterization of CuCN-derived compounds tends to present interesting challenges. In the original report of $[N(CH_3)_4][CuZn(CN)_4]$, for instance, the authors were forced to concede defeat regarding the orientation of cyanide groups linking Cu and Zn centres based on X-ray diffraction data (*168a*). And in the case of some cyano-Gilman reagents, the identity of the active species remains the subject of hot debate (*174*).

Curiously, the molecular structure of the archetypal copper(I) cyanide itself has never been definitively settled. Attempts to obtain single crystals adequate for diffraction studies have been confounded by its insolubility in most solvents, and its formation of crystalline adducts in others (e.g., $CuCN \cdot NH_3$ (*175*), $CuCN \cdot N_2H_4$ (*176*), $Cu_3(CN)_3 \cdot H_2O$ (*177*)). Moreover, even when sufficiently large crystals can be grown, the similar electron densities of carbon and nitrogen atoms present fundamental problems for X-ray diffraction techniques. The common practice of distinguishing carbon from nitrogen atoms on the basis of their distance from the

copper centres is of dubious merit, since ranges of $r_{Cu,C}$ and $r_{Cu,N}$ in known complexes overlap significantly (*178*).

The first structural report of CuCN involved red (monoclinic) and green (orthorhombic) forms for which unit cell parameters were estimated (*179*). However, mean molar ratios, (Cu/CN), for these forms were 0.94 and 0.91, respectively, and no subsequent work has corroborated the results. In 1957, a third, colourless form (Cu/CN = 0.993) was studied by X-ray diffraction in Cromer's group (*180*), reporting an orthorhombic space group with unit cell parameters: $a = 12.79$ Å, $b = 18.14$ Å, $c = 7.82$ Å, and 36 formula units per cell. More recently, a neutron diffraction study of the coinage metal monocyanides (*181*) found "very broad bands indicative of poor crystallinity" in the diffraction pattern of CuCN powder, concluding that it "was not possible to determine the crystal structure of this compound."

Many other techniques have been employed to understand its structure. On the basis of CN stretching frequencies, it has long been assumed that the cyanide acts as a bridging ligand between copper atoms (*181,182*). Furthermore, the tendency of Cu(I) to form polymeric chains has been invoked to posit the presence of Cu–C–N–Cu linkages. The most persuasive data in support of this conclusion, however, arise from extended X-ray absorption fine structure (EXAFS) results published only a few years ago (*183*). The Fourier-transformed spectra exhibit a series of three peaks which can be modelled using a linear Cu–C–N–Cu fragment. Unfortunately, EXAFS is unable to differentiate between Cu–C and Cu–N, and thus is subject to some of the same limitations as X-ray diffraction.

Further clues to the structure of CuCN have been gleaned from studies of oligomers in solution and in the gas phase. Copper(I) cyanide, solubilized in THF by addition of 2 equivalents LiCl, appears to retain significant oligomerization; its EXAFS spectrum is remarkably similar to that of solid CuCN (*183*). Moreover, its CN stretching frequency is near that of the solid, in the region usually attributed to bridging cyanides (*182*). Evidence has also been presented by mass spectrometric detection of laser-ablated solid CuCN that anionic $[Cu_n(CN)_{n+1}]^-$ and cationic

$[Cu_n(CN)_{n-1}]^+$ species ($n \leq 5$) have linear structures with alternating copper and cyanide groups (*184*). This conclusion is based, in part, on density functional theory calculations in which a variety of cyano ligation modes were explored for anionic, neutral and cationic $Cu_x(CN)_y$ clusters, the relative energies of which consistently favoured linear, bridging modes (*184*).

Another approach to the structural characterization of solids is NMR spectroscopy. Its isotope-specificity eliminates ambiguities associated with cyanide orientations, making it complementary to X-ray diffraction techniques. In the case of CuCN, each of the atoms has at least one nuclear spin-active isotope. Moreover, NMR is ideally suited for investigations of local structure and symmetry in cases where only powders or microcrystalline samples are available, as it does not rely on large single crystals. A wealth of information is potentially available from NMR parameters. For example, the orientation-dependence of nuclear shielding offers insight into the local symmetry, indirect spin-spin coupling constants establish connectivities and direct dipolar coupling constants provide internuclear distances. Indeed, NMR has already been used to study a wide variety of transition metal cyanide complexes in the solid state (*40,48,109,113,124,168b,185,186,187,188*). Notable examples include the incorporation of doubly labelled cyanide to resolve C/N orientational ambiguity in the $[N(CH_3)_4][CuZn(CN)_4]$ system (*109*), an extensive investigation of organotin coordination polymers (*186*), and promising results regarding structure and dynamics of adsorbed cyanide molecules on catalytic metal surfaces in electrochemical environments (*189*).

Presented here is a multinuclear magnetic and quadrupole resonance study of solid copper(I) cyanide. Results from ^{13}C and ^{15}N NMR spectra of stationary and magic-angle-spinning samples are combined with [63/65]Cu NQR data to support a linear, polymeric chain structure with "head-tail" disorder of the cyano groups. Most importantly, however, this demonstration highlights the applicability of solid state NMR to the structural elucidation of compounds for which standard diffraction techniques are of limited utility.

Experimental

Sample Preparation. Isotopically enriched samples of copper(I) cyanide were prepared by a modification of the method of Barber (*190*). An aqueous solution of $NaHSO_3$ (0.503 g in 3 mL) was added to a copper(II) sulfate solution (1.801 g in 10 mL H_2O) and acidified with HCl. Isotopically enriched potassium cyanide (6.8 mmol $KC^{15}N$ or $K^{13}C^{15}N$ (Isotec, Inc.), as appropriate), dissolved in water (3 mL), was added slowly, with stirring. The mixture was filtered and washed with boiling water and ethanol, and air-dried under suction for 2.5 hours. The resulting white solid was dried in a dessicator overnight and then by heating in an oil bath at 100°C under high vacuum for a day. This method typically produced a 70% yield of copper(I) cyanide.

Samples prepared in this way were characterized by Raman spectroscopy, with the observation of a single ν(CN) peak for each isotopic variant present in the powder: $Cu^{12}C^{14}N$ (2169 cm^{-1}), $Cu^{12}C^{15}N$ (2135 cm^{-1}), $Cu^{13}C^{14}N$ (2123 cm^{-1}), $Cu^{13}C^{15}N$ (2087 cm^{-1}) (*191*). No discolouration of the sample due to the presence of copper(II) impurity was observed, and no peaks attributable to excess KCN appeared in the Raman or NMR spectra.

NQR experiments were carried out on a natural abundance sample obtained from Aldrich Chemical Company. Some NMR measurements were also performed on a commercial sample of 99% ^{13}C-enriched CuCN (Isotec, Inc.).

Copper-63/65 Nuclear Quadrupole Resonance Spectroscopy. All NQR experiments were performed by Mr. John Hanna at CSIRO North Ryde NMR Laboratory in New South Wales, Australia. Quadrupole frequencies for ^{63}Cu and ^{65}Cu were obtained at ambient temperature using a Bruker CXP console pulsing into a probe arrangement that was well-removed from the magnet (> 5 m) and shielded from extraneous magnetic and radiofrequency interference by a mumetal container. The quadrupole frequency range scanned was determined from previous NQR studies of Cu(I) systems (*134,148,192*). The location of both ^{63}Cu and ^{65}Cu isotope resonances (related by the ratio $\nu_Q(^{63}Cu)/\nu_Q(^{65}Cu) = 1.081$) verified that true copper NQR frequencies were being observed. Due to the broad CuCN quadrupole resonances observed over the 34 – 45 MHz frequency range, the complete spectrum

was acquired in a point-by-point fashion, stepping the spectrometer frequency in 100 kHz increments through the entire region. The probe was retuned at each frequency, and a solid (Hahn) echo sequence, $90° - \tau - 180° - \tau - acquire$, with extended phase cycling (*147*) was employed to obtain undistorted echoes. The recycle delay was 0.5 s, and the bandwidth of the "soft" $90°$ and $180°$ pulses ($< 15\ \mu s$) excited only the fraction of the total linewidth about each resonance position, effectively defining the relative amplitudes at these frequency points. The resultant $^{63/65}Cu$ NQR spectrum is simply the Fourier-transformed spin-echo amplitude, plotted as a function of these designated frequencies.

Nuclear Magnetic Resonance Spectroscopy. Carbon-13 NMR spectra were collected in three applied magnetic fields, corresponding to the following ^{13}C Larmor frequencies: 50.33 MHz (Bruker MSL-200; $B_0 = 4.7$ T), 100.63 MHz (Bruker AMX-400; $B_0 = 9.4$ T), 201.22 MHz (Varian INOVA; $B_0 = 18.8$ T). Spectra acquired at 18.8 T were collected by Dr. Anil Mehta at Yale University. Magic-angle spinning spectra were acquired at room temperature by single pulse excitation, typically employing 3.5 μs $90°$ pulses separated by a 60 s recycle delay. Spectra of a non-spinning sample were excited by short pulses corresponding to small ($\sim 30°$) flip angles, and with relaxation delays of up to 15 minutes. Chemical shifts are reported with respect to TMS, using the methine carbons ($\delta_{iso} = +29.50$ ppm) in solid adamantane as a secondary reference. The time-domain data were treated with 100 Hz exponential multiplication prior to Fourier transformation.

Nitrogen-15 NMR spectra were acquired at 20.29 and 40.55 MHz using Bruker MSL-200 and AMX-400 spectrometers. A pulse duration of 6.0 μs corresponded to $90°$ excitation, and one-minute recycle delays were used for MAS experiments. For spectra of non-spinning samples, longer recycle delays (3 minutes) were used, as well as shorter excitation pulses ($\sim 30°$). Chemical shifts were referenced using solid $^{15}NH_4NO_3$, the isotropic chemical shift of which resonates at +23.80 ppm with respect to liquid ammonia at 20°C. Magic-angle spinning free induction decays were processed with 50 Hz Lorentzian line-broadening, whereas

stationary spectra received 250 Hz line-broadening.

In order to establish meaningful comparisons between experimental and calculated MAS lineshapes, it is necessary to construct an "isotropic MAS powder spectrum" by adding spectral intensity located in spinning sidebands to the centreband (*113*). This was done for all ^{13}C and ^{15}N MAS spectra prior to attempting lineshape calculations.

NMR Spectral Calculations. Calculations of the NMR lineshapes utilized WSolids and QUADSPIN, both C programs developed in this laboratory incorporating either first-order perturbation theory or full-matrix diagonalization of the Zeeman-quadrupolar Hamiltonian for the dipolar-coupled quadrupolar nucleus (*38c*).

Ab initio Calculations. Chemical shielding and electric field gradient calculations were performed using Gaussian 94 (*193*) at the Hartree-Fock level of theory, with nuclear shieldings evaluated by GIAO (gauge-included atomic orbitals) (*194*). Carbon and nitrogen atoms were represented by a 6-311+G(d) basis set, copper atoms by 3-21G(d). A variety of atomic arrangements were designed to explore the shielding and EFG characteristics of neutral $(CuCN)_n$-type chains (n = 1-4). The conclusions in this work are based on linear chain fragments of $Cu_2(CN)_2$; the addition of extra atoms in the chain or in adjacent chains had only a minor influence on the properties of interest. For example, CN-*Cu*-CN-Cu and NC-*Cu*-*N*C-Cu were taken to mimic "ordered" chains with properties derived from the atoms in italics. "Disordered" analogues assumed the form NC-*Cu*-CN-Cu and CN-*Cu*-*N*C-Cu. Bond lengths were chosen according to estimates based on NMR data: $r_{Cu,C}$ = 1.88 Å, $r_{Cu,N}$ = 1.92 Å, $r_{C,N}$ = 1.18 Å.

Carbon-13 and nitrogen-15 nuclear shieldings computed with respect to the "bare nuclei" were converted to chemical shift scales by the absolute shieldings of their respective reference compounds. The absolute shielding of carbon-13 nuclei in tetramethylsilane at 300 K is 184.1 ppm (*195*) and the absolute shielding of the nitrogen-15 nucleus in liquid ammonia at 300 K is 244.6 ppm (*196*).

Results and Discussion

Carbon-13 and nitrogen-15 NMR spectra of stationary and spinning solid samples of isotopically enriched CuCN were acquired at 4.7 and 9.4 T (Figure 30, Figure 31, Figure 32). The excellent agreement between calculated and experimental spectra is based on a single spin-1/2 ^{13}C or ^{15}N site coupled to a quadrupolar copper nucleus, taking into consideration Zeeman, direct and indirect spin-spin coupling interactions (Table 7). Because the $^{63/65}$Cu nuclear quadrupole resonance frequencies in CuCN are on the same order of magnitude as their respective Larmor frequencies (Table 8), quadrupolar effects must be considered to correctly simulate observed ^{13}C and ^{15}N NMR spectra. The results of these NMR spectral analyses — summarized in Table 7 — provide overwhelming evidence for the presence of linear chains of Cu–N–C–Cu units. Spin-spin coupling data provide unequivocal evidence that each carbon is bonded to one copper, and each nitrogen is also bonded to one copper. That these chains are linked in a linear fashion emerges from the observation of axially symmetric nitrogen and carbon shielding tensors. The $^{63/65}$Cu NQR spectrum (Figure 33) indicates that cyanide ligands within a chain are disordered in a "head-tail" fashion, based on the multiplicity and breadth of observed peaks. The following paragraphs offer a more detailed analysis of the spectral observations and their structural implications.

Immediately obvious from Figure 30 and Figure 31 is the dependence of the lineshape on the applied magnetic field. Moreover, the lineshape bears little resemblance to the equally spaced quartet anticipated for coupling to a spin 3/2 nucleus in the high-field limit. This field-dependent distortion originates in dipolar coupling to copper-63/65 nuclei possessing quadrupole coupling constants which are not negligible with respect to their Larmor frequency (41,49,37,197).

As with the copper phosphines, to properly account for the tensorial nature of these interactions, a rigorous lineshape calculation demands information about the *magnitudes* of the EFG, indirect spin-spin and dipolar coupling tensors, as well as their relative *orientations*. In the most general case, this presents a hopeless tangle of variables. However, the structural linearity encountered in the present case greatly
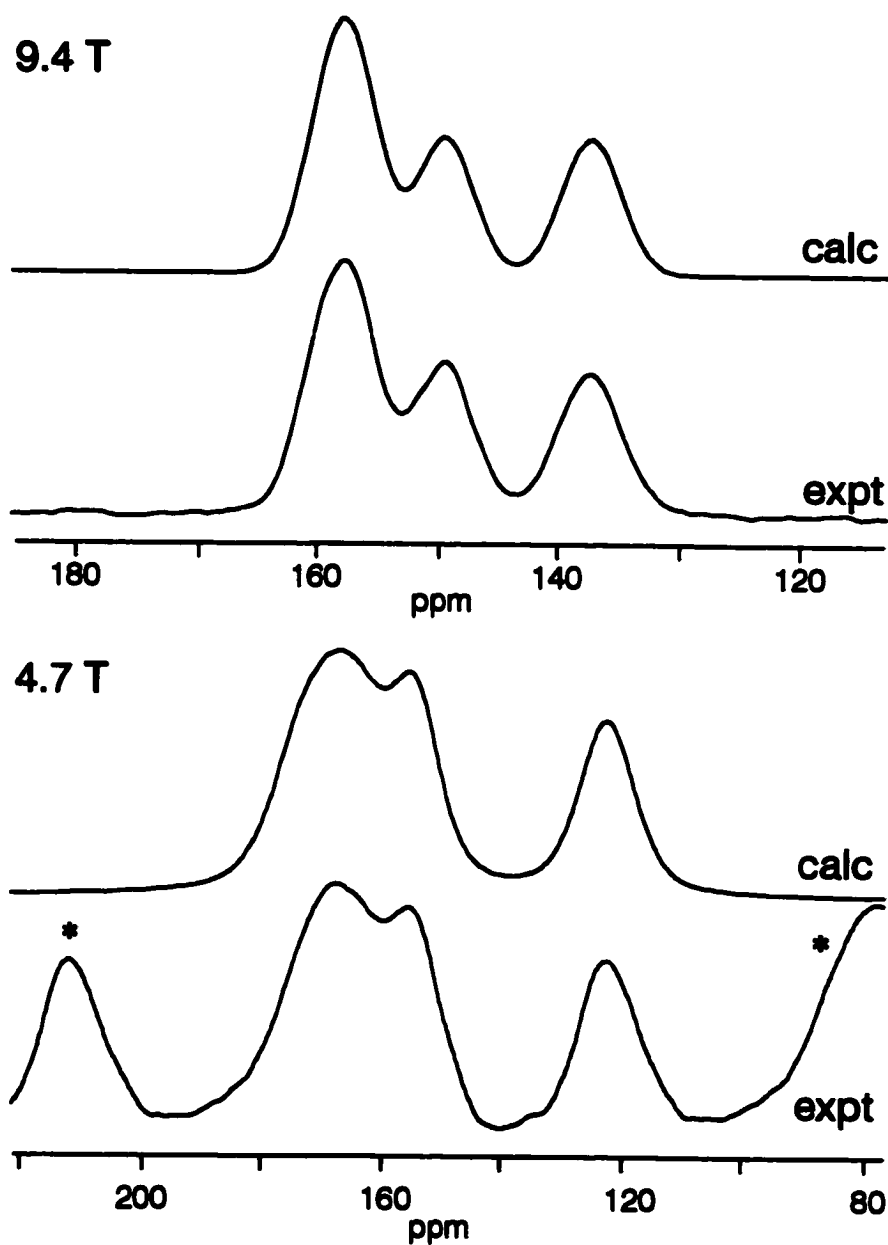
Figure 30   Experimental and calculated ^{13}C MAS NMR spectra of 30% ^{13}C^{15}N-enriched copper(I) cyanide; see Table 7 for fitting parameters. Each displayed spectral region spans 7.25 kHz. For 4.7 and 9.4 T spectra, rotation rates were 4.5 and 8.0 kHz, respectively, and the numbers of transients were 286 and 232. Calculated spectra were convolved with a 50:50 gaussian/lorentzian line-broadening function of 500 Hz. Intensity from spinning sidebands has been summed to construct an isotropic powder MAS NMR spectrum; spectral artifacts arising from this procedure are marked with asterisks.
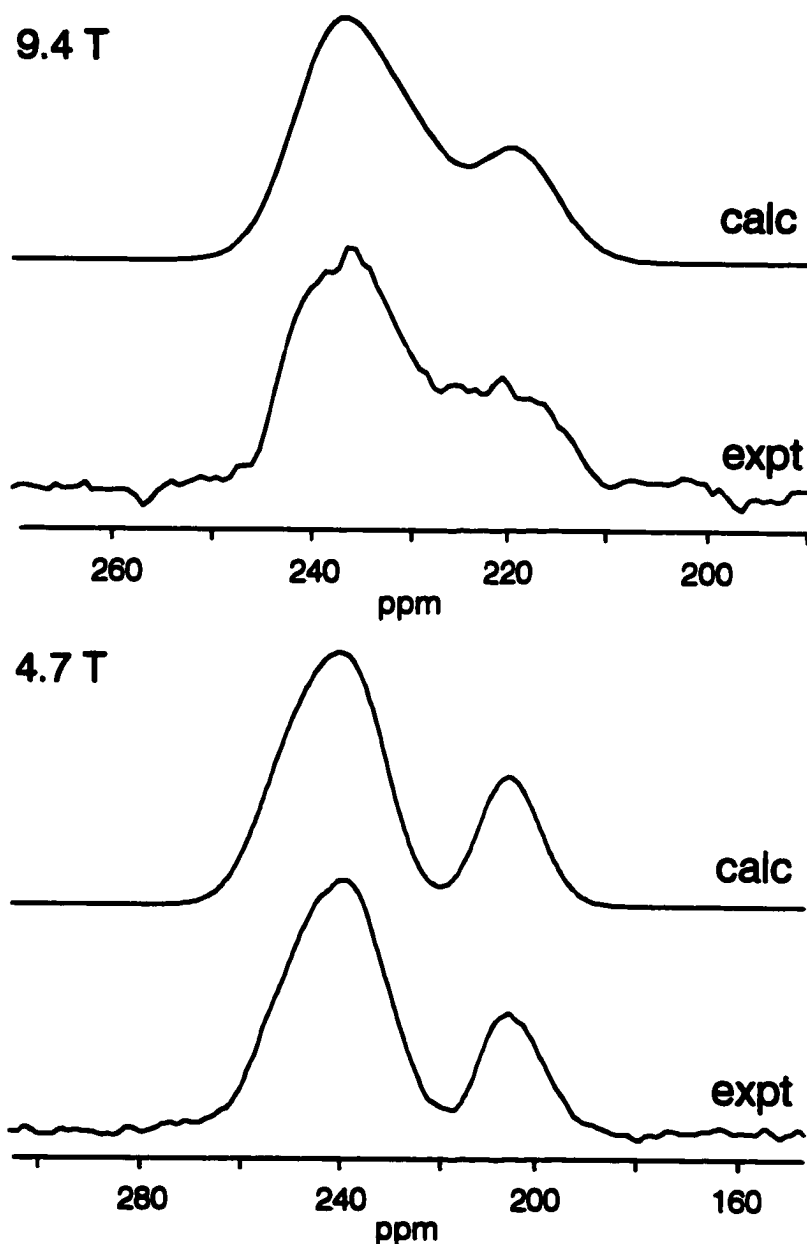
Figure 31   Experimental and calculated ^{15}N MAS NMR spectra of 70% ^{15}N-enriched copper(I) cyanide; see Table 7 for fitting parameters. Each displayed spectral region spans 3.2 kHz. For 4.7 and 9.4 T spectra, rotation rates were 3.0 and 10.0 kHz, respectively, and the numbers of transients was 175 and 442. Calculated spectra were convolved with gaussian line-broadening function of 300 Hz (4.7 T) and 400 Hz (9.4 T). Intensity from spinning sidebands has been summed to construct an isotropic powder MAS spectrum.
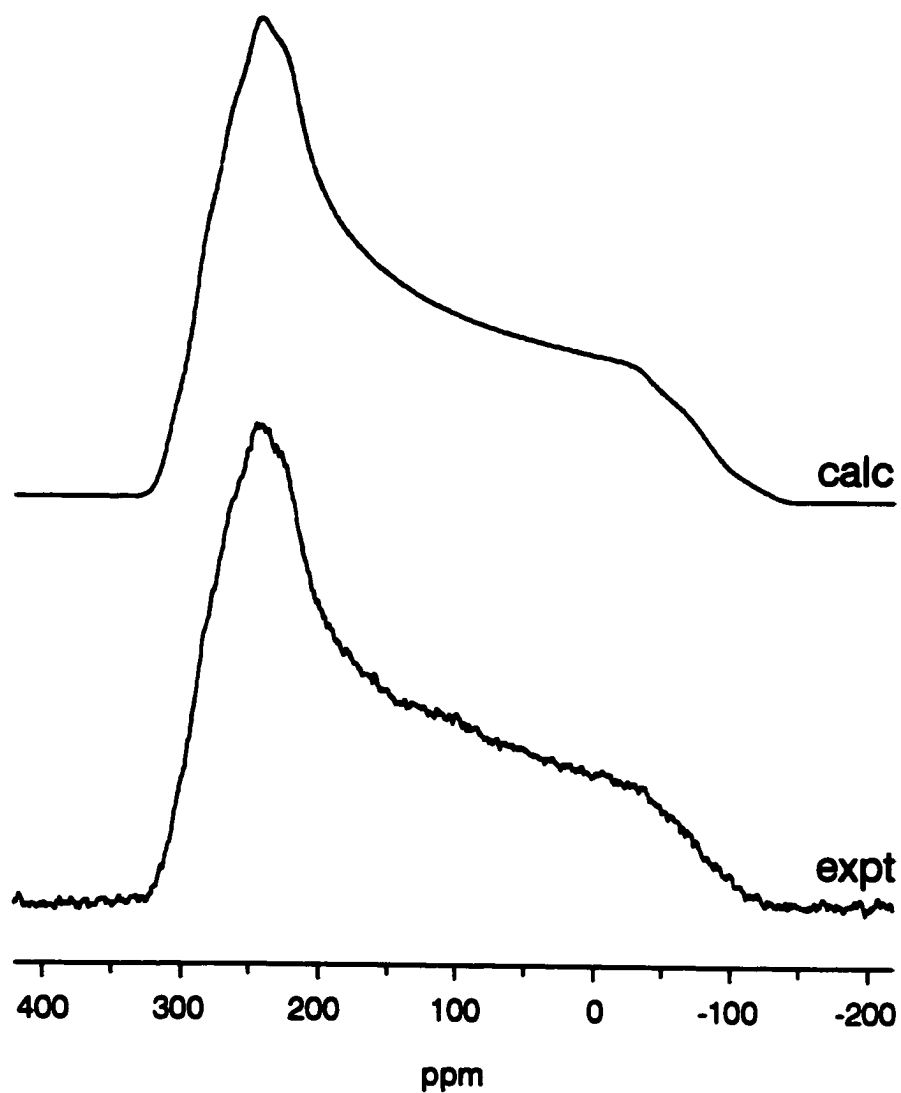
Figure 32 Experimental and calculated ^{13}C NMR spectra of stationary 99%
$^{13}C^{15}N$-enriched copper(I) cyanide; see Table 7 for fitting parameters.
The calculated spectrum was convolved with a 2 kHz lorentzian line-
broadening function. The experimental spectrum is the result of 64
transients.
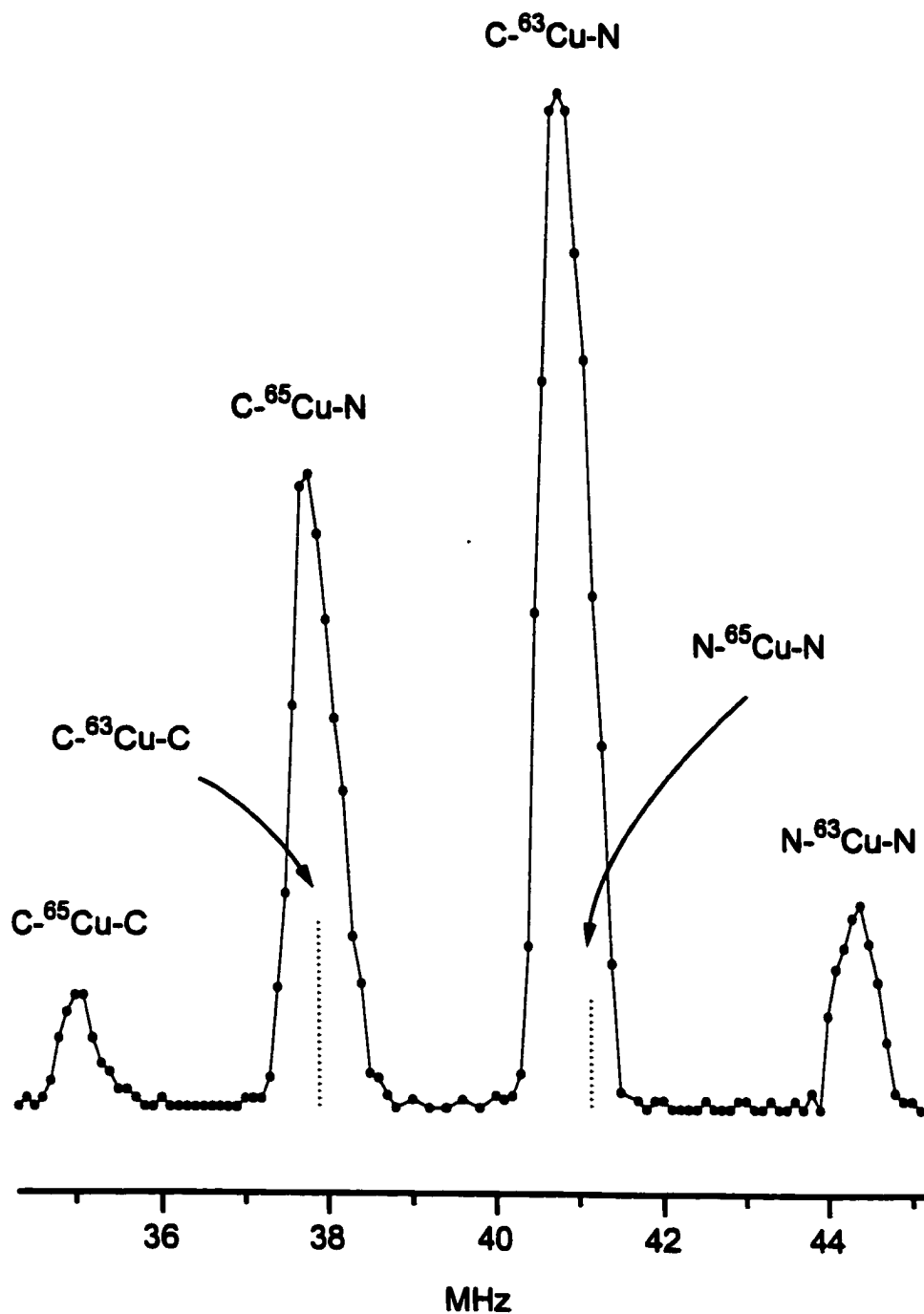
Figure 33   NQR spectrum depicting $^{63/65}$Cu resonances of natural abundance
copper(I) cyanide. Labels represent assignments based on *ab initio*
EFG calculations.

Table 7   Carbon-13 and nitrogen-15 NMR data for copper(I) cyanide

	^{13}C	^{15}N
$\delta_{iso}{}^{a,b}$ /ppm	$+151\pm1$	$+232\pm2$
$\delta_{\perp}{}^{a,c}$ /ppm	$+267\pm10$	$+385\pm10$
$\delta_{\parallel}{}^{a,c}$ /ppm	-84 ± 10	-70 ± 10
$^1J(^{63}Cu,X)^{b,d}$ /Hz	$+725\pm20$	-250 ± 15
$R_{eff}(^{63}Cu,X)^{b,d}$ /Hz	$+1200\pm50$	-460 ± 50

a ^{13}C chemical shifts relative to TMS, using solid adamantane as a secondary reference; ^{15}N chemical shifts referenced using solid $^{15}NH_4NO_3$, which resonates at $+23.80$ ppm with respect to liquid ammonia at 20°C

b obtained from NMR spectra of samples spinning at the magic angle, analyzed using a "one-site model"

c obtained from NMR spectra of stationary powder samples, analyzed using a "one-site model"

d parameters for spin pairs involving ^{65}Cu were varied according to the relative magnetogyric ratios of the two copper isotopes: e.g., $^1J(^{65}Cu,^{13}C)/^1J(^{63}Cu,^{13}C) = 1.071$

Table 8   Nuclear quadrupole resonance data for copper(I) cyanide

	$\nu_Q(^{63}Cu)/MHz^a$	$\nu_Q(^{65}Cu)/MHz^a$
"CN–Cu–NC"	44.4	$(41.1)^b$
"CN–Cu–CN"	40.8	37.8
"NC–Cu–CN"	$(37.9)^b$	35.0

a cited frequencies represent peak maxima, with an estimated precision better than ± 100 kHz; the distribution of ν_Q stemming from long-range disorder, however, extends the uncertainty to approximately ± 500 kHz

b values in parentheses represent peak positions anticipated based on the ratio of copper quadrupole moments, but obscured by overlapping resonances

simplifies this problem (see below). Under such circumstances, the indirect spin-spin coupling (J) tensor and the $^{63/65}Cu$ EFG tensors are axially symmetric and coincident with the direct dipole-dipole (R) tensor, all of which are aligned with their unique components along the internuclear axis (150). When all orientational relationships are known, the lineshape calculation involves only three variables.

In copper(I) cyanide, evidence for linearity is found in the NMR spectra of stationary samples. Carbon-13 NMR spectra collected at 4.7, 9.4 and 18.8 T and nitrogen-15 NMR spectra at 4.7 and 9.4 T are characteristic of axially symmetric chemical shielding tensors with spans typical of linear M-C-N fragments (see, for example, Figure 32) (40,113). Indeed, full lineshape calculations incorporating the effects of coupling to both spin-active copper isotopes (and neighbouring spin-1/2 nuclei where appropriate) were successful only for axially symmetric shielding tensors with greatest nuclear shielding when the unique component is parallel to the applied magnetic field (Table 7).

The high sensitivity of chemical shielding tensors to short-range local symmetry is well-known. A pertinent example is found in the cyano ^{13}C and ^{15}N shielding tensors of ten solid para-substituted benzonitriles where small, but significant, deviations from axial symmetry are observed, in spite of a high degree of local symmetry (198). By contrast, strictly axial symmetry is observed for ^{13}C shielding tensors in $K_2M(CN)_4$ (M = Zn, Cd, Hg), where linearity is dictated by crystal symmetry (40). The observation of axial symmetry in the ^{15}N and ^{13}C shielding tensors of copper(I) cyanide serves as a strong witness to its linear molecular structure.

Additional support for linearity comes from the experimental values of the most shielded component of the chemical shift tensors, $\delta_{\parallel}$. Ramsey's well-known theory of nuclear shielding (199,200) partitions the total shielding into diamagnetic and paramagnetic contributions, σ^d and σ^p, respectively. The latter generally represents a deshielding effect, and its computation constitutes a formidable challenge to theoreticians due to a critical dependence on excited electronic states. For a linear

molecule, however, the paramagnetic contribution to $\sigma_\parallel$ vanishes in the non-relativistic limit, and the total shielding is simply described by the diamagnetic shielding. The calculation of this term from first principles is straightforward, as it relies only on ground-state wavefunctions. Therefore, the extent to which the observed $\sigma_\parallel$ deviates from the calculated value provides an indication of molecular non-linearity in the present case. The theoretical carbon-13 shielding component along the chain for a linear arrangement of CN-Cu-^{13}CN-Cu is computed by *ab initio* methods to be $\sigma_\parallel{}^d = +286.5$ ppm, corresponding to a chemical shift, $\delta_\parallel{}^d = -102.3$ ppm (*195*). Experimentally, $\delta_\parallel$ is found to be -84 ± 10 ppm. For nitrogen-15, $\sigma_\parallel{}^d$ is calculated to be +352.7 ppm, which can be converted to the chemical shift scale, yielding $\delta_\parallel{}^d = -108.1$ ppm (*196*). The experimental value is -70 ± 10 ppm. Considering the extreme sensitivity of $\sigma_\parallel{}^p$ to off-axis atoms, (e.g., the central carbon-13 in allene possesses $\sigma_\parallel{}^p = -250$ ppm), and presumably minor contributions from intermolecular effects, this level of agreement can be considered further evidence for the existence of linear chains in CuCN.

The magnitudes of the copper-63/65 quadrupolar interactions were independently assessed using zero-field nuclear quadrupole resonance spectroscopy. For an axially symmetric EFG tensor of spin 3/2, the measured quadrupole frequency is simply half the nuclear quadrupole coupling constant, C_Q (*8*). For natural abundance CuCN, four unusually broad resonances were observed over the range 34 - 45 MHz (Figure 33), thus necessitating a "point-by-point" acquisition. Based on their relative quadrupole moments and natural abundances, it is evident that, in fact, *three* copper sites are present, with fortuitous overlap between different isotopes of neighbouring peaks. Resonance positions are listed in Table 8, the numbers in parentheses representing peaks calculated on the basis of $Q(^{65}Cu)/Q(^{63}Cu)$. The proposed assignment of these spectral features is based on *ab initio* calculations of the electric field gradient for extended chain fragments with various orientations of the cyanide groups, intended to mimic "ordered" and "disordered" copper sites (see Experimental section). As such, copper nuclei directly bonded to two cyano carbons

are predicted to possess a smaller EFG than copper nuclei flanked by two cyano nitrogens. Naturally, intermediate values are expected for copper nuclei in fully ordered CuCN chains. The calculated magnitudes, while not in quantitative agreement with experiment, adequately reproduce the relative magnitudes of C_Q.

While a variety of experimental idiosyncracies preclude direct quantification of these sites from spectral intensities, it can be estimated that 20 – 40% of the copper nuclei are located at "disordered" sites, i.e., C–Cu–C or N–Cu–N. By implication, the formation of copper cyanide chains is not random, but expresses a marginal preference for ordering. This conclusion is also supported by *ab initio* calculations, for which the energies of chain fragments with different cyano orientations are not identical. The orientational disorder present in CuCN(s) is not *dynamic* disorder as in the case of alkali metal cyanides at room temperature (*201*), for this would involve bond-breaking and the consequent decoupling of copper nuclei from ^{15}N and ^{13}C; it is *static* disorder, wherein the motion is slow with respect to $^1J(^{63/65}Cu, ^{13}C)^{-1}$.

The insight provided by these NQR data influences the detailed interpretation of ^{13}C and ^{15}N MAS NMR spectra. Each of these lineshapes must be understood in terms of *two* independent sites coupled to copper-63/65 nuclei having different values of C_Q. More vexing, perhaps, is that chemical shifts, *J*-couplings and dipolar couplings may, in principle, differ as well. These individual sites are unresolved, their overlap resulting in the broad MAS NMR peaks observed. Consequently, two approaches are used in understanding the MAS lineshapes. As a first approximation, it is assumed that both sites (e.g., ^{13}C–Cu–C and ^{13}C–Cu–N) possess identical chemical shifts and coupling parameters, peak broadening of several hundred hertz being introduced empirically after a full-matrix diagonalization evaluation of the frequencies ("one-site model"). In the second approach, an attempt is made to reproduce the lineshapes by including all interactions within the framework of first-order perturbation theory ("multiple-site model"). The former method provides estimates of the coupling constants, while the latter is used to investigate the origins of the peak broadness.

From ^{13}C MAS NMR spectra, the "one-site model" yields a $^1J(^{63}$Cu,^{13}C) of +725 Hz (202). This relatively large value is indicative of one-bond coupling to a spin-3/2 nucleus and confirms that the carbons are directly bonded to copper nuclei. In fact, its magnitude may even be understood to confer additional evidence for linearity. For the nearly tetrahedral cuprate anions in K$_3$Cu(CN)$_4$ (section 2.3.2) and [N(CH$_3$)$_4$][CuZn(CN)$_4$] (109), $^1J(^{63}$Cu,^{13}C) is +300 Hz, whereas in the trigonally coordinated cuprate KCu(CN)$_2$, $^1J(^{63}$Cu,^{13}C) $\approx$ +500 Hz (203). Assuming, as a first approximation, that the Fermi contact mechanism plays a prominent role in the coupling (156), the magnitude of $^1J(^{63}$Cu,^{13}C) in a dicoordinate, linear structure is expected to be larger still. In related mercury(II) cyanide complexes, for example, $^1J(^{199}$Hg,^{13}C) = 1540 Hz in tetrahedral K$_2$Hg(CN)$_4$ (113), whereas it is 3158 Hz in linear Hg(CN)$_2$ (204). The experimental value of +725 Hz for $^1J(^{63}$Cu,^{13}C) is consistent with this model.

The dipolar coupling constant, $R_{eff}(^{63}$Cu,^{13}C), determined likewise from ^{13}C MAS NMR spectra is +1200 Hz, from which is calculated a bond length of 1.88 Å (equation (24)). This conclusion, of course, is subject to the same considerations as the copper phosphines. What is actually measured in an NMR experiment is the *effective* dipolar coupling constant, comprising contributions from the direct dipolar coupling constant and from anisotropy in the J tensor (150). For a ^{63}Cu,^{13}C spin pair, this involves

$$R_{DD}(^{63}\text{Cu},^{13}\text{C}) = \left(\frac{\mu_0}{4\pi}\right)\left(\frac{\hbar}{2\pi}\right)\gamma(^{63}\text{Cu})\,\gamma(^{13}\text{C})\,\langle r_{\text{Cu,C}}^{-3}\rangle \quad . \tag{81}$$

If the bond length is known, this relationship can be used to determine the anisotropic character of J. Conversely, one can obtain an estimate of the bond length based on equation (24). Here, it is usually necessary to make an assumption about the contribution of ΔJ to R_{eff}. For coupling between many of the lighter elements, (e.g. H, C, N), a small range of isotropic J-couplings is understood to imply negligible values of ΔJ; i.e., $R_{eff} \approx R_{DD}$. For heavier nuclei, (e.g. P, Cu, Hg), it is known that indirect spin-spin coupling may depend significantly on orientation, although

well-characterized **J** tensors are scarce (*33,197,205*). Since no information on the anisotropy of $J(^{63/65}Cu,^{13}C)$ appears to have been reported in the literature, one may choose to ignore the effects of ΔJ, or try to incorporate its effect in some qualitative way, recognizing that either approach introduces indeterminate uncertainty in the bond length calculated from R_{eff}. For positive values of J_{iso} (see below), it is generally assumed that $J_{\parallel}$ is larger than $J_{\perp}$. Thus, ΔJ is a positive quantity, and serves to *decrease* R_{eff} relative to R_{DD}, thereby *lengthening* the apparent internuclear distance with respect to the actual value.

Another phenomenon which modulates R_{eff} is motional averaging (*160*). Here again, the effect is to diminish the measured dipolar coupling constant, yielding an apparent bond length which is longer than the "true" separation. These effects have been thoroughly studied for C–H spin pairs (*160a,b*), and more recently, for the heavier nuclei (^{13}C, ^{15}N, ^{17}O) in glycine (*160c*). The influence is thought to be small for bonded nuclei other than protons, generally amounting to less than 3%. In any case, the internuclear distance, $r_{Cu,C}$, determined from R_{eff} must be understood to represent an upper limit, since the combined effect of both motional averaging and ΔJ would accumulate, rather than cancel. For a linear system such as this, one might anticipate substantial directionality in *J*-coupling. As an example, if it is arbitrarily assumed that ΔJ does not exceed $J_{iso}/2$, $R_{eff}(^{63}Cu,^{13}C)$ ranges from +1200 to +1340 Hz, corresponding to $r_{Cu,C} = 1.85 \pm 0.04$ Å.

From ^{15}N MAS NMR spectra, the magnitude of the effective dipolar coupling, $R_{eff}(^{63}Cu,^{15}N)$ is found to be 460 Hz from the one-site model, corresponding to an internuclear separation of 1.92 Å. Emphasizing again that this represents an upper bound due to potential contributions from **J** anisotropy and motional averaging, it can at least be understood as indicating a nitrogen-bound cyano-copper linkage. Further evidence for this comes from the isotropic *J*-coupling, $^{1}J(^{63}Cu,^{15}N) = -250$ Hz. Although no values of $^{1}J(^{63}Cu,^{15}N)$ appear to be available in the literature, a comparison with non-bonded $^{2}J(^{63}Cu,^{15}N) \approx -20$ Hz in $K_3Cu(CN)_4$ (section 2.4.2) clearly establishes the connectivity.

These results are consistent with conventional wisdom based on crystallographically characterized cyanocuprates, with all the usual caveats regarding C/N identification. For Cu–CN bonds, $r_{Cu,C}$ is found to range from 1.80 to 1.86 Å in nearly linear dicoordinate systems (206), increasing to 1.92 ± 0.03 Å in three-coordinate complexes (207), and marginally further to 1.94 ± 0.06 Å for four-coordinate cyanocuprates (178c). The NMR-derived bond length of 1.88 Å being an upper bound, this falls comfortably within the range anticipated for linear, dicoordinate copper. This value also agrees with EXAFS data for solid CuCN, which could be fit with a distance of 1.85 or 1.86 Å between the copper and its nearest neighbour, either carbon or nitrogen (183). Density functional theory appears to overestimate $r_{Cu,C}$ in a number of linear permutations of copper and cyanide units, converging around 1.90 Å (184), whereas multireference second-order perturbation calculations on the simple monomeric unit, CuCN, yield even longer bonds:

$$r_{Cu,C} = 1.94 \text{ Å } (208).$$

Given the large uncertainty associated with the NMR-derived bond length for Cu–NC, comments about its agreement with other $r_{Cu,N}$ offer little insight. That notwithstanding, an example of a nearly linear CN–Cu–NC has been reported in an adduct of CuCN and biquinoline (209), containing a copper–nitrogen bond of 1.82 Å. More generally, crystallographically characterized cyanocuprates tend to exhibit Cu–NC bonds longer than Cu–CN bonds in the same compounds, with values of the former ranging from 1.99 to 2.05 Å (178c). Calculations based on both density functional theory (184) and a multireference second-order perturbation approach (208) have these orderings reversed, with Cu–NC separations exceeding Cu–CN bond lengths by 0.03 Å and 0.05 Å, respectively.

The emergent picture of solid copper(I) cyanide as comprising linear, polymeric chains is remarkably similar to the structures of the analogous silver(I) and gold(I) cyanide complexes (191). Although early X-ray diffraction studies of these compounds suffered from ambiguity regarding the identity of carbon and nitrogen atoms, the results were interpreted to indicate infinite linear chains in each case,

though the structures of AgCN and AuCN were not thought to be strictly isomorphous (*191*). Recent powder neutron diffraction results have confirmed this assertion (*181*).

An interesting feature of the ^{13}C and ^{15}N MAS NMR spectra is the observed linewidths: ^{13}C peaks exceed 500 Hz at 4.7 and 9.4 T, and ^{15}N peaks at 4.7 T are greater than 300 Hz. The source of this broadening lies partly in the cyanide disorder indicated by NQR. In particular, the local environment about a given ^{13}C or ^{15}N nucleus will be subtly influenced by the orientation of the *next* cyanide in the chain. Assuming that these effects become negligible beyond two bonds, this implies that *two* distinct ^{13}C and ^{15}N environments are present within a chain, each possessing its own chemical shift and coupling constants. The superposition of these sites results in spectral broadening.

A second contribution to the linewidths comes from residual dipolar coupling to quadrupolar copper nuclei other than those directly bonded. For example, within a given chain, a carbon-13 nucleus is situated not only 1.88 Å from a neighbouring copper-63/65, but also two bonds away from another spin-active copper nucleus. This internuclear distance is approximately 3 Å, corresponding to a dipolar coupling constant of almost 300 Hz. It is likely that a small $^2J(^{63/65}Cu,^{13}C)$ is also involved, the net result of which is a splitting (or broadening) amounting to several hundred Hz. If interactions with adjacent *chains* are also considered, it is easy to account for the *ca.* 500 Hz peakwidths observed in ^{13}C MAS NMR spectra. A similar rationale may be applied to ^{15}N NMR spectra.

To test the plausibility of this argument, ^{13}C and ^{15}N MAS NMR lineshapes were evaluated using first-order perturbation theory. This approach enables the inclusion of multiple sites ("ordered": C–Cu–N and "disordered": N–Cu–N, C–Cu–C) with couplings to multiple nuclei (^1J and ^2J). For the ^{13}C MAS NMR data at 4.7 and 9.4 T, a chemical shift difference between the two sites of 2 ppm could be introduced before the simulation deviated noticeably from the experimental spectrum. Likewise, reasonable agreement between the two-site simulation and the experimental lineshape was obtained for differences in $^1J(^{63}Cu,^{13}C)$ for the two sites as large as 50 Hz (i.e.,

$^1J(^{63}Cu, ^{13}C)$ = 700 and 750 Hz). Similar results were found for the ^{15}N MAS NMR spectral simulations: the largest difference in $\delta_{iso}(^{15}N)$ that reproduced the experimental data obtained at 4.7 and 9.4 T was 4 ppm, and $^1J(^{63}Cu, ^{15}N)$ could vary by no more than 20 Hz. ($^2J(^{63/65}Cu, ^{13}C)$ and $^2J(^{63/65}Cu, ^{15}N)$ in these calculations were chosen somewhat arbitrarily to be ~ 1/5 of the one-bond J-coupling; however, they could be much smaller without drastically altering the appearance of the calculated spectrum.) It is interesting to note that *ab initio* shielding calculations predict that the isotropic ^{13}C shielding in a disordered CuCN chain is 2.7 ppm more shielded than in an ordered chain; a disordered ^{15}N site is calculated to be 3.7 ppm more shielded than the ordered analogue.

Additional clues to the spectral effects of multiple sites come from the ^{13}C MAS NMR spectrum recorded at 18.8 T (ν_L = 201.2 MHz) (Figure 34). The experimental isotropic bandshape cannot be reproduced by a single ^{13}C site. Furthermore, the intensity distribution demands not only a chemical shift difference, but also a difference in values of $^1J(^{63}Cu, ^{13}C)$. Although it would be pointless to attempt a *rigorous* simulation of the lineshape, (considering explicitly *only* ^1J and ^2J, there are 16 sites, and 17 independent parameters!), a two-site model offers a reasonable fit (202) with the "ordered" site possessing δ_{iso} = 152 ppm, $^1J(^{63}Cu, ^{13}C)$ = 690 Hz, $|^2J(^{63}Cu, ^{13}C)|$ = 210 Hz, and the "disordered" site having δ_{iso} = 150 ppm, $^1J(^{63}Cu, ^{13}C)$ = 740 Hz, $|^2J(^{63}Cu, ^{13}C)|$ = 150 Hz. This result underscores an advantage of high-field NMR: residual dipolar couplings are reduced, and the chemical shift difference (in Hz) is amplified, leading to an improved determination of NMR parameters for distinct sites.

The breadth of the NQR peaks is also anomalously large, ranging from 500 kHz to over one MHz. Although $^{63}Cu-^{63}Cu$, $^{65}Cu-^{63}Cu$ and $^{65}Cu-^{65}Cu$ dipolar interactions are present in the solid, their contribution to the linewidth is undoubtedly minor compared to that arising from a distribution of quadrupole frequencies. The main peaks observed are due to nearest neighbour effects, but the sensitivity of EFGs to long-range effects demands that more distant (CuCN) units, as well as adjacent
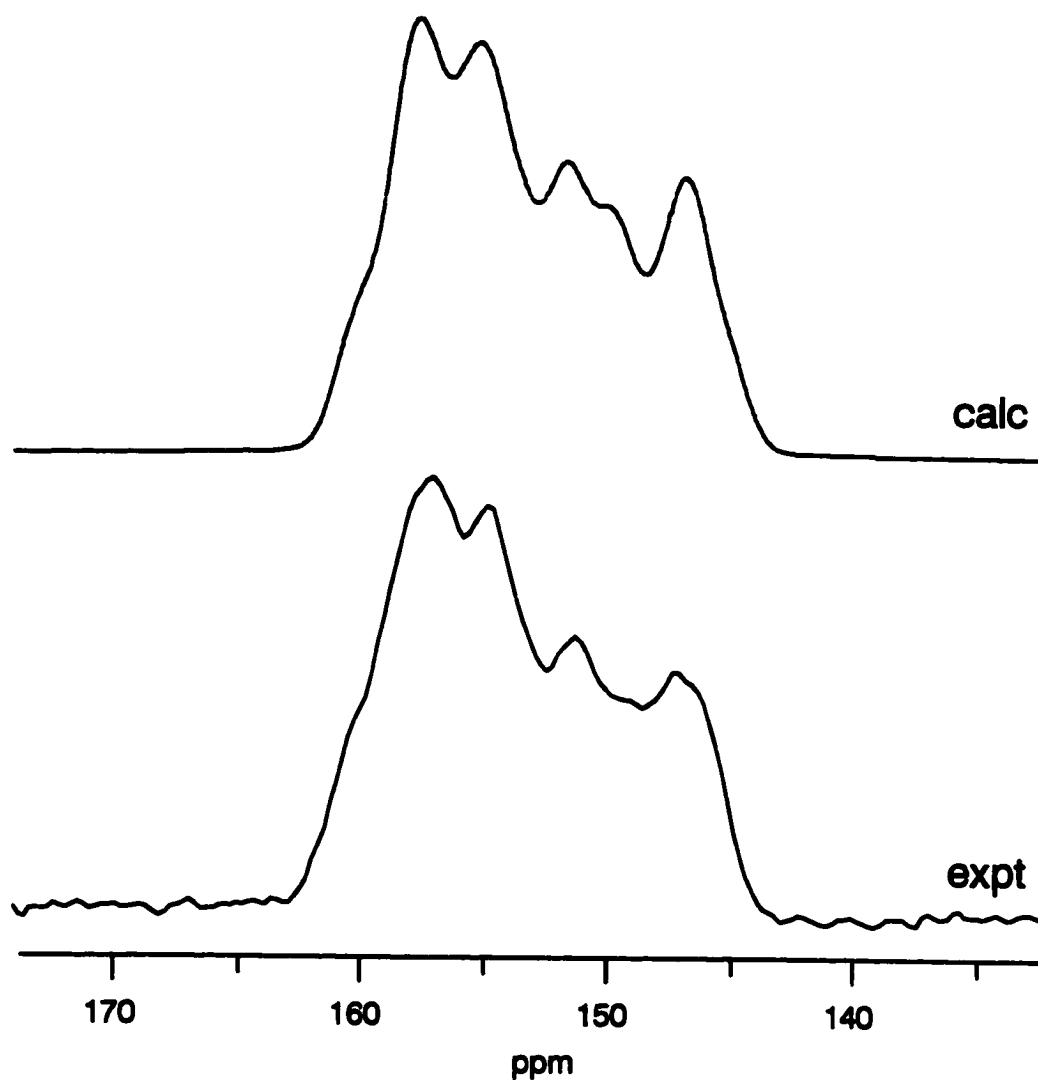
Figure 34   Experimental and calculated ^{13}C MAS NMR spectra of 30% $^{13}C^{15}N$-enriched copper(I) cyanide, acquired in a magnetic field of 18.8 T (ν_L = 201.224 MHz); see text for details of the calculation. The sample rotation rate was 20.6 kHz, and 222 transients were collected. Calculated spectrum was convolved with a 75:25 gaussian/lorentzian line-broadening function of 370 Hz. Intensity from spinning sidebands has been summed to construct an isotropic powder MAS spectrum.

chains, be considered as well. Again, the *ab initio* calculations offer support for this assertion, as EFGs at the three non-terminal copper nuclei in an ordered, linear $(CuCN)_4$ chain vary by 5%. Allowing for "head-tail" cyanide disorder as well as the possibility of translational displacement of the chains with respect to each other, it is easy to account qualitatively for the observed NQR peak widths.

Finally, information regarding the signs of the coupling constants is available from the MAS NMR spectral calculations. Because the magnitude of $C_Q(^{63}Cu)$ is comparable to $\nu_L(^{63}Cu)$ – especially at 4.7 T, where C_Q exceeds ν_L – the copper spin states are not accurately described as simple perturbations to the Zeeman states, and lineshape calculations must invoke full-matrix diagonalization of the combined Zeeman-quadrupolar Hamiltonian operator (*197*). Under such circumstances, spectra become sensitive to the relative signs of the quantities C_Q, R_{eff} and J_{iso} (*197*). For carbon-13 MAS NMR spectra acquired at 4.7 T, agreement between calculations based on the one-site model and experimental spectra is possible only if all three signs are the same; the only physically plausible solution for these quantities is that their signs are positive. Since R_{DD} is positive by virtue of the like signs of $\gamma(^{13}C)$ and $\gamma(^{63}Cu)$ (see eq. (24)), ΔJ would have to exceed +7 kHz to yield a negative R_{eff}! This result is also consistent with the signs of $C_Q(^{63}Cu)$ in linear bis(tribenzylphosphine)cuprate salts from NMR measurements (*197*) and in diatomic copper halides from microwave spectroscopy (*158,159*). Finally, a positive J-coupling agrees with the sign of one-bond *reduced* coupling constants (*155*) involving group 14 elements and transition metals (*156*).

For ^{15}N MAS NMR, spectra acquired at 4.7 T required full diagonalization, with significant lineshape changes observed upon altering the sign of $^1J(^{63}Cu,^{15}N)$. This confirms that the signs of J_{iso} and R_{eff} are negative, as anticipated, based on the negative sign of $\gamma(^{15}N)$. Employing reduced coupling constants (*155*), one can compare $^1K(Cu,N)$ with $^1K(Cu,P)$ for the linear systems, copper(I) cyanide and the bis(tribenzylphosphine)cuprate cation (*197*), to obtain values of $+7.72\times10^{21}$ and $+11.98\times10^{21}$ $NA^{-2}m^{-3}$, respectively. The like signs and relative magnitudes conform

to predictions within a given group of the periodic table (*156*).

Conclusions

Drawing on these NMR and NQR data, a consistent picture of the structure of solid copper(I) cyanide emerges. Both ^{13}C and ^{15}N MAS NMR spectra exhibit large J-couplings to copper nuclei, indicating that all cyanides act as bridging ligands. The internuclear distances can be estimated from dipolar coupling constants, yielding $r_{Cu,C} \approx 1.88$ Å and $r_{Cu,N} \approx 1.92$ Å. While the uncertainties in these numbers are large, they establish unequivocally the connectivities. Carbon-13 and nitrogen-15 NMR spectra of non-spinning samples are characteristic of axially symmetric chemical shielding tensors, thus providing strong evidence for a linear molecular arrangement. Finally, the multiplicity of resonances detected in copper-63/65 NQR spectra suggest that there exist three types of copper environments: C–Cu–N, N–Cu–N and C–Cu–C. The only structure that satisfies all of these requirements involves linear polymeric chains of the form:

$$+Cu-C-N+_n ,$$
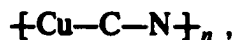
where cyanide groups are disordered in a "head-tail" fashion.

More generally, this study serves to demonstrate the type of information that is available from routine, one-dimensional NMR experiments of solids. The success of magic-angle spinning NMR in determining the structure of solid CuCN highlights its particular utility in probing local molecular environments and providing information about connectivities and bond lengths. Anisotropic nuclear shielding can also be useful in establishing local symmetry, based on the appearance of NMR powder patterns collected from non-spinning samples. Invaluable information from NQR includes quadrupole frequencies, on the basis of which different copper chemical environments are easily distinguished. With the growing importance of solid materials for which large single crystals are not available, it is expected that nuclear resonance techniques will play an increasingly prominent role in structural elucidation.

3.3 Summary

Large quadrupole interactions which cannot be accurately described as simple perturbations to the Zeeman interaction must be understood in terms of a combined Zeeman-quadrupolar Hamiltonian operator, the eigenstates of which depend on the orientation of the EFG tensor with respect to the Zeeman field. Naturally, this deviation from the pure Zeeman spin states also influences the transition frequencies of dipolar-coupled nuclei, manifesting in their MAS spectra as distortions from symmetrical, J-coupled multiplets. These "distortions", however, depend on the dipolar coupling constant, and therefore effectively *recouple* the dipolar interaction. Usually averaged to zero by magic-angle spinning, the dipolar interaction provides the internuclear separation of the coupled spins. Hence, in favourable circumstances, the lineshapes of spin-1/2 MAS spectra may be analysed to gain valuable structural information. The foregoing applications of this approach rely on sufficiently high crystal symmetry to define the tensor orientations, as well as measurements of the copper-63/65 quadrupole frequency by zero-field nuclear quadrupole resonance. In the case of copper(I) cyanide, analyses of ^{15}N and ^{13}C MAS NMR spectra yields values of R_{eff} corresponding to Cu–C and Cu–N bonds, thus identifying the structure to consist of "infinite" polymeric chains. For linear tribenzylphosphine cuprate salts, the NMR measurement of R_{eff} is used in conjunction with the direct dipolar coupling constant calculated from the crystal structure to enable a full characterization of the anisotropic $^{1}J(^{63/65}Cu,^{31}P)$ tensor. The results of analogous spectral analyses of trimethoxyphenylphosphine cuprate halides known to deviate from linearity by a few degrees caution against the invocation of axial tensorial symmetry where not warranted by the appropriate symmetry elements. Also available from MAS spectral analyses requiring full-matrix diagonalization of the Zeeman-quadrupolar Hamiltonian are the relative signs of R_{eff}, J_{iso} and C_Q, a characteristic not normally accessible within the limits of first-order perturbation theory. Finally, zero-field NQR has proven to be an essential tool for precise measurements of R_{eff} originating in large quadrupole interactions.

4. CONCLUDING REMARKS AND FUTURE RESEARCH SUGGESTIONS

The results presented in this thesis suggest a number of directions for further study. An obvious next step proceeding from Chapter 2 is the analysis by NMR of a single crystal exhibiting the predicted asymmetric dipolar splittings in the satellite transitions of the quadrupolar nucleus. The ideal system for such an observation would involve an isolated spin pair consisting of a quadrupolar nucleus and a spin-1/2 nucleus. The magnitude of ν_Q must be sufficiently large with respect to ν_L to produce observable effects, but not so large that NMR signals are difficult to locate upon crystal reorientation in the magnetic field. Potential candidates might include four-coordinate copper(I) complexes, hydroxyl groups or cobaloximes enriched in a given spin-1/2 ligand.

Another natural supplement to this work – already discussed in section 2.4.3 – is the observation of more examples where MQMAS is used to detect isotropic J-couplings. Of particular interest would be higher-order MQ/SQ correlations to exploit the increased resolution predicted by theory. In addition to the suggestions in section 2.4.3, it would be gratifying if MQMAS could be used to resolve J-couplings involving two quadrupolar nuclei, $J(S,S')$. Identifying an appropriate compound for such an investigation may be a challenge, however, given the difficulties encountered in locating examples of $J(S,I)$.

Many important applications of $^{63/65}Cu$ MQMAS may be envisioned. Closely related to the work on $K_3Cu(CN)_4$, 3QMAS of copper-63/65 could be profitably performed on framework compounds based on tetracyanocuprate tetrahedra (*103*), or novel copper(I) 1,2,4,5-tetracyanobenzene coordination polymers involving $Cu(NCCH_3)_4^{+1}$ precursors (*210*). Multiple sites, cyanide ordering and the influence of guest molecules on C_Q and δ_{iso} could be directly probed by $^{63/65}Cu$ 3QMAS, similar to the studies attempted by Ratcliffe and co-workers without the aid of multiple-quantum MAS (*109*). Moreover, nearly tetrahedral copper(I) compounds in a calix[6]arene host have recently been advocated as supramolecular models for

metalloenzyme active sites (211). My preliminary $^{63/65}$Cu NMR results on the basic [Cu(NCCH$_3$)$_4$][PF$_6$] unit suggest a very small C_Q and favourable sensitivity for 3QMAS studies. It would be of interest to examine the NMR properties of copper in such a guest/host environment, thus providing a direct means of probing molecular geometry at the metal centre of interest.

Chapter 3 represents a starting point for the study of copper-63/65 nuclei possessing large quadrupole interactions. With the increasing prevalence of such systems, zero-field NQR is combination with NMR of neighbouring spin-1/2 nuclei may prove to be invaluable for offering structural insight. Having thoroughly examined the "extremes", as it were, of copper(I) geometry – four-coordinate in K$_3$Cu(CN)$_4$ and two-coordinate in CuCN – the missing link is three-coordinate copper in KCu(CN)$_2$. Its crystal structure has long been known to consist of spiral polymer chains, the "backbone" being defined by [Cu–CN]$_\infty$ subunits with cyanide ligands "dangling" from each copper atom (99). Particularly appealing about KCu(CN)$_2$ is that the electric field gradient at the copper nucleus has been fully characterized by Zeeman-perturbed NQR of a single crystal (112). Isotopically enriched samples of KCu(CN)$_2$ have, in fact, been prepared, and their ^{13}C and ^{15}N NMR spectra recorded; however, a satisfactory analysis has not yet been achieved. A primary obstacle is that the high symmetry on which the success of the abovementioned analyses hinged, is absent, demanding assumptions about the relative tensor orientations in this compound. Relatedly, the EFG tensor is not axially symmetric (η = 0.78) and its magnitude (C_Q = 60.9 MHz) renders inadequate a first-order perturbation treatment (112). The full-matrix diagonalization, however, has been fully developed and computer-coded only for axially symmetric EFG tensors. This compound may provide an impetus for elaboration of the theory to greater generality and wider applicability.

Essential to the successful determination of copper(I) cyanide structure by NMR is the presence of linear chains, inferred from ^{13}C and ^{15}N shielding tensors. It would, therefore, be of interest to examine the shielding in a hydrazine adduct of

copper(I) cyanide where infinite zig-zag chains of $(Cu-C-N)_{\infty}$ lie in a mirror plane, with bond angles Cu–C–N = 175.2° and Cu–N–C = 179.3° (*176*). Nominally four-coordinate due to interaction with hydrazine, the copper(I) geometry bears a remarkable resemblance to that in copper(I) cyanide, making it an ideal model for evaluating the sensitivity of shielding tensors to deviations from linearity. This compound may also provide spin-spin coupling data, isotropic chemical shifts and nuclear quadrupole coupling constants to add to the growing corpus of NMR parameters in complexes of copper(I) and cyanide, eventuating in a more complete picture of the relationship between bonding and NMR observables. Another excellent test of linearity and cyanide shielding might involve expanding the field of view to include analogous silver and gold cyanides. The 1:1 complexes are known to be linear from powder neutron diffraction (*181*), and may shed additional light on shielding tensors in linear polymeric metal cyanides.

Finally, as a natural extension of this work, substantial effort has been invested in the structural characterization of some *organo*cyanocuprates. In particular, I am interested in compounds derived from organolithium and copper cyanide. Initial reports of these "cyano-Gilman reagents" (*212*) identified exceptional reactivity and versatility in the 2:1 species, dubbing them "higher-order" cyanocuprates to reflect the postulate that their unusual properties stem from a three-coordinate R_2CuCN moiety. This assertion was subsequently challenged (*174c*), sparking a lively debate that rages still today (see, for example, reference *174b*). Contributing to the ambiguity accompanying solution NMR results are problems associated with exchanging ligands and rapid relaxation of the copper nucleus, both of which decoupled the metal, effectively rendering it invisible by NMR. In solids, however, neither of these phenomena are active, and NMR may prove a powerful means to gain structural insight in such cases. Dipolar coupling constants can be estimated from quadrupole-perturbed ^{13}C or ^{15}N MAS spectra, provided the quadrupolar interaction at the coupled nucleus is sufficiently large (i.e., copper-63/65). Conversely, lithium–carbon/nitrogen internuclear distances may be determined by REDOR.

Irrespective of the bonding arrangement, NMR techniques exist to obtain the desired information for solid compounds. Indeed, examples of the 1:1 (*206c*) and 2:1 (*213*) lithium organocyanocuprates have been recently observed in the solid state. Given the exciting new results on silyl derivatives of cyanocuprates (*171a*) and novel cyanide-containing organozincates (*214*), structural information on organocyanometallates is becoming of critical importance in the development of this field.

....

Perhaps it is a truism in scientific research that every answer is accompanied by new questions. No less true, however, is that understanding is rarely advanced by a simple application of "The Scientific Method"; it follows its own course, resembling more an inquisitive *process* than a discreet question/answer *event*. Also true is that now, more than ever, the scientific enterprise is being pressed to validate itself in terms understandable to the broader political and social community, thus raising new criteria for evaluating which questions are worth pursuing. Viewed by some scientists as threatening, these changes may also be perceived as providing an impetus to consider carefully which research directions will be of long-term benefit, and to present their aspirations creatively and without pretence. I hope that the work presented in this thesis and in the foregoing proposals stand witness to the possibility of intertwining utilitarian and fundamental research interests.

References and Notes

1. (a) Stern, O. *Z. Physik* **1921**, *7*, 249. (b) Stern, O.; Gerlach, W. *Z. Physik* **1921**, *8*, 110.

2. Purcell, E. M.; Torrey, H. C.; Pound, R. V. *Phys. Rev.* **1946**, *69*, 37.

3. Bloch, F.; Hansen, W. W.; Packard, M. *Phys. Rev.* **1946**, *69*, 127.

4. Proctor, W. G.; Yu, F. C. *Phys. Rev.* **1950**, *77*, 717.

5. Zeeman, P. *Philos. Mag.* **1897**, *43*, 226.

6. Larmor, J. *Philos. Mag.* **1897**, *44*, 503.

7. Mason, J. *Solid State NMR*, **1992**, *2*, 285.

8. Das, T. P.; Hahn, E. L. *Solid State Physics – Advances in Research and Applications*; Seitz, F.; Turnbull, D., Eds.; Academic Press, Inc.: New York, 1958; Supplement 1.

9. Cohen, M. H.; Reif, F. *Solid State Physics – Advances in Research and Applications*; Seitz, F.; Turnbull, D., Eds.; Academic Press, Inc.: New York 1957; Volume 5; pp. 321-438.

10. (a) Liao, M.-Y.; Chew, B. G. M.; Zax, D. B. *Chem. Phys. Lett.* **1995**, *242*, 89. (b) Liao, M.-Y.; Zax, D. B. *J. Phys. Chem.* **1996**, *100*, 1483. (c) Yang, D. K.; Zax, D. B. *J. Magn. Reson.* **1998**, *135*, 267.

11. Dumazy, Y.; Amoureux, J. P.; Fernandez, C. *Mol. Phys.* **1997**, *90*, 959.

12. Kentgens, A. P. M. *J. Magn. Reson.* **1991**, *95*, 619.

13. Medek, A.; Frydman, V.; Frydman, L. *Proc. Natl. Acad. Sci. USA*, **1997**, *94*, 14237.

14. Poplett, I. J. F.; Smith, M. E. *Solid State NMR* **1998**, *11*, 211.

15. Kundla, E.; Samoson, A.; Lippmaa, E. *Chem. Phys. Lett.* **1981**, *83*, 229.

16. Behrens, H.-J.; Schnabel, B. *Physica B* **1982**, *114*, 185.

17. Samoson, A. *Chem. Phys. Lett.* **1985**, *119*, 29.

18. (a) Skibsted, J.; Nielsen, N. C.; Bildsøe, H.; Jakobsen, H. J. *Chem. Phys. Lett.* **1992**, *188*, 405. (b) Skibsted, J.; Nielsen, N. C.; Bildsøe, H.; Jakobsen, H. J. *J. Magn. Reson. A*, **1991**, *95*, 88.

19. C. Jäger, *NMR, Basic Principles and Progress*; Springer-Verlag: New York, 1994; Volume 31, pp.135-170.

20. Ganapathy, S.; Schramm, S.; Oldfield, E. *J. Chem. Phys.* **1982**, *77*, 4360.

21. (a) Lefebvre, F.; Amoureux, J. P.; Fernandez, C.; Derouane, E. G. *J. Chem. Phys.* **1987**, *86*, 6070. (b) Amoureux, J. P.; Fernandez, C.; Lefebvre, F. *Magn. Reson. Chem.* **1990**, *28*, 5.

22. Llor, L.; Virlet, J. *Chem. Phys. Lett.* **1988**, *152*, 248.

23. Mueller, K. T.; Sun, B.Q.; Chingas, G.C.; Zwanziger, J.W.; Terao, T.; Pines, A. *J. Magn Reson.* **1990**, *86*, 470.

24. Samoson, A.; Lippmaa, E.; Pines, A. *Mol. Phys.* **1988**, *65*, 1013.

25. Frydman, L.; Chingas, G. C.; Lee, Y. L.; Grandinetti, P. J.; Eastman, M. A.; Barrall, G. A.; Pines, A. *J. Chem. Phys.* **1992**, *97*, 4800.

26. Amoureux, J. P. *Solid State NMR*, **1995**, *4*, 229.

27. Medek, A.; Sachleben, J. R.; Beverwyk, P.; Frydman, L. *J. Chem. Phys.* **1996**, *104*, 5374.

28. Shore, J. S.; Wang, S. H.; Taylor, R. E.; Bell, A. T.; Pines, A. *J. Chem. Phys.* **1996**, *105*, 9412.

29. (a) Frydman, L; Harwood, J. S. *J. Am. Chem. Soc.* **1995**, *117*, 5367. (b) Medek, A.; Harwood, J. S.; Frydman, L. *J. Am. Chem. Soc.* **1995**, *117*, 12779.

30. G. Wu, S. Kroeker, R.E. Wasylishen and R.G. Griffin. *J. Magn. Reson.* **1997**, *124*, 237.

31. (a) Kowalewski, J. *Prog. NMR Spectrosc.* **1977**, *11*, 1. (b) Kowalewski, J. *Annu. Rep. NMR Spectrosc.* **1982**, *12*, 81.

32. Contreras, R.; Facelli, J. C. *Annu. Rep. NMR Spectrosc.* **1993**, *27*, 255.

33. Eberstadt, M.; Gemmecker, G.; Mierke, D. F.; Kessler, H. *Angew. Chem. Int. Ed. Engl.* **1995**, *34*, 1671.

34. Pople, J. A. *Mol. Phys.* **1958**, *1*, 168.

35. Abragam, A. *Principles of Nuclear Magnetism*; Oxford University Press: New York, 1961; pp. 305-316; 331-332.

36. Sanders, J. C. P.; Schrobilgen, G. J. *Multinuclear Magnetic Resonance in Liquids and Solids - Chemical Applications*; Granger, P.; Harris, R. K., Eds.; NATO ASI Series - Series C: Mathematical and Physical Sciences, Kluwer Academic Publishers: Dordrecht, The Netherlands, 1990; Vol. 322; pp. 157-186.

37. (a) Harris, R. K.; Olivieri, A. C. *Prog. NMR Spectrosc.* 1992, *24*, 435. (b) Gobetto, R.; Harris, R. K.; Apperley, D. C. *J. Magn. Reson.* 1992, *96*, 119.

38. (a) Eichele, K.; Wasylishen, R. E.; Corrigan, J. F.; Doherty, S.; Sun, Y.; Carty, A. J. *Inorg. Chem.* 1993, *32*, 121. (b) Wasylishen, R. E.; Wright, K. C.; Eichele, K.; Cameron, T. S. *Inorg. Chem.* 1994, *33*, 407. (c) Eichele, K.; Wasylishen, R. E.; Grossert, J. S.; Olivieri, A. C. *J. Phys. Chem.* 1995, *99*, 10110. (d) Schurko, R. S.; Wasylishen, R. E.; Nelson, J. H. *J. Phys. Chem.* 1996, *100*, 8057.

39. Chu, P.-J.; Lunsford, J. H.; Zalewski, D. J. *J. Magn. Reson.* 1990, *87*, 68.

40. Wu, G.; Kroeker, S.; Wasylishen, R. E. *Inorg. Chem.* 1995, *34*, 1595.

41. Casabella, P. A. *J. Chem. Phys.* 1964, *41*, 3793.

42. (a) Opella, S. J.; Frey, M. H.; Cross, T. A. *J. Am. Chem. Soc.* 1979, *101*, 5856. (b) Hexem, J. G.; Frey, M. H.; Opella, S. J. *J. Chem. Phys.* 1982, *77*, 3847.

43. Olivieri, A. C.; Frydman, L.; Diaz, L. E. *J. Magn. Reson.* 1987, *75*, 50.

44. Olivieri, A. C.; Frydman, L.; Grasselli, M.; Diaz, L. *Magn. Reson. Chem.* 1988, *26*, 615.

45. Olivieri, A. C. *J. Magn. Reson.* 1989, *81*, 201.

46. Olivieri, A. C. *J. Am. Chem. Soc.* 1992, *114*, 5758.

47. Alarcón, S. H.; Olivieri, A. C.; Harris, R. K. *Solid State NMR* 1993, *2*, 325.

48. Stoll, M. E.; Vaughan, R. W.; Saillant, R. B.; Cole, T. *J. Chem. Phys.* 1974, *61*, 2896.

49. Menger, E. M.; Veeman, W. S. *J. Magn. Reson.* 1982, *46*, 257.

50. McNamara, R.; Wu, C. H.; Chirlian, L. E.; Opella, S. J. *J. Am. Chem. Soc.* 1995, *117*, 7805.

51. Wu, G.; Wasylishen, R. E. *Mol. Phys.* 1998, in press.

52.   Drachman, S. R; Roch, G. E.; Smith, M. E. *Solid State NMR* **1997**, *9*, 257.

53.   Faucon, P.; Charpentier, T.; Bertrandie, D.; Nonat, A.; Virlet, J.; Petit, J. C. *Inorg. Chem.* **1998**, *37*, 3726.

54.   Stebbins, J. F.; Xu, Z. *Nature* **1997**, *390*, 60.

55.   (a) Amoureux, J.-P.; Bauer, F.; Ernst, H.; Fernandez, C.; Freude, D.; Michel, D.; Pingel, U.-T. *Chem. Phys. Lett.* **1998**, *285*, 10. (b) Pingel, U.-T.; Amoureux, J.-P.; Anupold, T.; Bauer, F.; Ernst, H.; Fernandez, C.; Freude, D.; Samoson, A. *Chem. Phys. Lett.* **1998**, *294*, 345.

56.   Hu, K.-N.; Hwang, L.-P. *Solid State NMR* **1998**, *12*, 211.

57.   Rocha, J.; Esculcas, A. P.; Fernandez, C.; Amoureux, J. P. *J. Phys. Chem.* **1996**, *100*, 17889.

58.   Fernandez, C.; Amoureux, J. P. *Chem. Phys. Lett.* **1995**, *242*, 449.

59.   Baltisberger, J. H.; Xu, Z.; Stebbins, J. F.; Wang, S. H; Pines, A. *J. Am. Chem. Soc.* **1996**, *118*, 7209.

60.   Hanna, J. V.; Smith, M. E.; Whitfield, H. J. *J. Am. Chem. Soc.* **1996**, *118*, 5772.

61.   Kraus, H.; Prins, R.; Kentgens, A. P. M. *J. Phys.Chem.* **1996**, *100*, 16336.

62.   Samoson, A. *J. Magn. Reson. A* **1996**, *121*, 209.

63.   Wang, S. H.; Xu, Z.; Baltisberger, J. H.; Bull, L. M.; Stebbins, J. F.; Pines, A. *Solid State NMR* **1997**, *8*, 1.

64.   Wang, S. H.; DePaul, S. M.; Bull, L. M. *J. Magn. Reson.* **1997**, *125*, 364.

65.   Steuernagel, S. *Solid State NMR* **1998**, *11*, 197.

66.   (a) Pruski, M.; Lang, D. P.; Fernandez, C.; Amoureux, J.-P. *Solid State NMR.* **1997**, *7*, 327. (b) Fernandez, C.; Delevoye, L.; Amoureux, J.-P.; Lang, D. P.; Pruski, M. *J. Am. Chem. Soc.* **1997**, *119*, 6858.

67.   Fernandez, C.; Lang, D. P.; Amoureux, J.-P.; Pruski, M. *J. Am. Chem. Soc.* **1998**, *120*, 2672.

68.   U. Haeberlen. *Advances in Magnetic Resonance. Supp. 1* Academic Press: New York, 1976.

69.   Samoson, A.; Lippmaa, E. *Phys. Rev. B*, **1983**, *28*, 6567.

70. Man, P. P. *in* "Encyclopedia of Nuclear Magnetic Resonance" (D. M. Grant and R. K. Harris, Eds.) pp. 3838-3847, John Wiley & Sons, Chichester, U.K. (1996).

71. Amoureux, J.-P. *Solid State NMR* **1993**, *2*, 83.

72. Massiot, D.; Touzo, B.; Trumeau, D.; Coutures, J. P.; Virlet, J.; Florian, P.; Grandinetti, P. J. *Solid State NMR* **1996**, *6*, 73.

73. Man, P. P. *Phys. Rev. B* **1998**, *58*, 2764.

74. Wu, G.; Rovnyak, D.; Sun, B.; Griffin, R. G. *Chem. Phys. Lett.* **1996**, *249*, 210.

75. Fernandez, C.; Amoureux, J.-P. *Solid State NMR* **1996**, *5*, 315.

76. Fernandez, C.; Amoureux, J.-P.; Frydman, L. *Chem. Phys. Lett.* **1996**, *259*, 347.

77. (a) Ding, S.; McDowell, C. A. *Chem. Phys. Lett.* **1997**, *270*, 81. (b) Ding, S.; McDowell, C. A. *J. Magn. Reson.* **1998**, *135*, 61.

78. Marinelli, L.; Medek, A.; Frydman, L. *J. Magn. Reson.* **1998**, *132*, 88.

79. Fernandez, C.; Amoureux, J.-P.; Chezeau, J. M.; Delmotte, L.; Kessler, H. *Microporous Materials* **1996**, *6*, 331.

80. Wu, G.; Rovnyak, D.; Griffin, R. G. *J. Am. Chem. Soc.* **1996**, *118*, 9326.

81. Marinelli, L.; Frydman, L. *Chem. Phys. Lett.* **1997**, *275*, 188.

82. Massiot, D. *J. Magn. Reson. A* **1996**, *122*, 240.

83. Fyfe, C. A.; Skibsted, J.; Grondey, H.; Meyer zu Altenschildesche, H. *Chem. Phys. Lett.* **1997**, *281*, 44.

84. Ernst, R.; Bodenhausen, G.; Wokaun, A. *Principles of NMR in One and Two Dimensions;* Oxford University Press: New York, 1987.

85. Brown, S. P.; Heyes, S. J.; Wimperis, S. *J. Magn. Reson. A* **1996**, *119*, 280.

86. Amoureux, J.-P.; Fernandez, C.; Steuernagel, S. *J. Magn. Reson. A* **1996**, *123*, 116.

87. Amoureux, J.-P.; Fernandez, C. *Solid State NMR* **1998**, *10*, 211.

88. Fernandez, C.; Amoureux, J.-P.; Delmotte, L.; Kessler, H. *Microporous Materials* **1996**, *6*, 125.

89. (a) McDowell, C. A. *Encyclopedia of Nuclear Magnetic Resonance*; Grant, D. M.; Harris, R. K., Eds; John Wiley & Sons: Chichester, U.K., 1996; pp. 2901-2908. (b) Harris, R. K. *Encyclopedia of Nuclear Magnetic Resonance*; Grant, D. M.; Harris, R. K., Eds; John Wiley & Sons: Chichester, U.K., 1996; pp. 2909-2914.

90. Stark, R. E.; Haberkorn, R. A.; Griffin, R. G. *J. Chem. Phys.* **1978**, *68*, 1996.

91. Goc, R.; Ponnusamy, E.; Tritt-Goc, J.; Fiat, D. *Int. J. Peptide Protein Research*, **1988**, *31*, 130.

92. Sarv, P.; Fernandez, C.; Amoureux, J.-P.; Keskinen, K. *J. Phys. Chem.* **1996**, *100*, 19223.

93. Charpeutier, T.; Virlet, J. *Solid State NMR* **1998**, *12*, 227.

94. Steuernagel, S. private communication

95. Verkade, J. G.; King, R. W.; Heitsch, C. W. *Inorg. Chem.* **1964**, *3*, 884.

96. Bailey, W. C. *J. Mol. Spectrosc.* **1997**, *185*, 403.

97. Power, W. P. *J. Am. Chem. Soc.* **1995**, *117*, 1800.

98. Cowley, A. H.; Damasco, M. C. *J. Am. Chem. Soc.* **1971**, *93*, 6815.

99. Cromer, D. T. *J. Phys. Chem.* **1957**, *61*, 1388.

100. Cromer, D. T.; Larson, A. C. *Acta Cryst.* **1962**, *15*, 397.

101. Roof, R. B. Jr.; Larson, A. C.; Cromer, D. T. *Acta Cryst.* **1968**, *B24*, 269.

102. Batten, S. R.; Robson, R. *Angew. Chem. Int. Ed.* **1998**, *37*, 1461.

103. Ibrahim, A. M. A. *J. Organomet. Chem.* **1998**, *556*, 1.

104. Ibrahim, A. M. A.; Siebel E.; Fischer, R. D. *Inorg. Chem.* **1998**, *37*, 3521.

105. Chesnut, D. J.; Zubieta, J. *Chem. Commun.* **1998**, 1707.

106. Goodfellow, R. J. *Multinuclear NMR*; Mason, J., Ed.; Plenum Press: New York, 1987; p 564.

107. Andrew, E. R.; Carolan, J. L.; Randall, P. J. *Chem. Phys. Lett.* **1971**, *11*, 298.

108. for example: (a) Pennington, C. H.; Durand, D. J.; Slichter, C. P.; Rice, J. P.; Bukowski, E. D.; Ginsberg, D. M. *Phys. Rev. B* **1989**, *39*, 274. (b) Pennington, C. H.; Durand, D. J.; Slichter, C. P.; Rice, J. P.; Bukowski, E. D.; Ginsberg, D. M.

Phys. Rev. B **1989**, *39*, 2902. (c) Barrett, S. E.; Durand, D. J.; Pennington, C. H.; Slichter, C. P.; Friedmann, T. A.; Rice, J. P.; Ginsberg, D. M. *Phys. Rev. B* **1990**, *41*, 6283.

109. (a) Curtis, R. D.; Ratcliffe, C. I.; Ripmeester, J. A. *Chem. Commun.* **1992**, 1800. (b) Nishikiori, S.; Ratcliffe, C. I. *Disorder in Materials*, **1995**, *10*, 9.

110. Reisfeld, M. J.; Jones, L. H. *J. Mol. Spectrosc.* **1965**, *18*, 222.

111. Krüger, H.; Meyer-Berkhout, U. *Z. Physik* **1952**, *132*, 171.

112. McKown, G. L.; Graybeal, J. D. *J. Chem. Phys.* **1966**, *44*, 610.

113. Wu, G.; Wasylishen, R. E. *J. Phys. Chem.* **1993**, *97*, 7863.

114. Yamamoto, T.; Haraguchi, H.; Fujiwara, S. *J. Phys. Chem.* **1970**, *74*, 4369.

115. Endo, K.; Yamamoto, K.; Deguchi, K.; Matsushita, K. *Bull. Chem. Soc. Jpn.* **1987**, *60*, 2803.

116. Alderman, D. W.; Solum, M. S.; Grant, D. M. *J. Chem. Phys.* **1986**, *84*, 3717.

117. Staritzky, E.; Ellinger, F. H. *Anal. Chem.* **1956**, *28*, 422.

118. Cox, E. G.; Wardlaw, W.; Webster, K. C. *J. Chem. Soc.* **1936**, 775.

119. Becker, G. *Z. Physik* **1951**, *130*, 415.

120. Schurko, R. W.; Wasylishen, R. E.; Phillips, A. D. *J. Magn. Reson.* **1998**, *133*, 388.

121. Jakobsen, H. J.; Skibsted, J.; Bildsøe, H.; Nielsen, N. C. *J. Magn. Reson.*, **1989**, *85*, 173.

122. Pesek, J. J.; Mason, W. R. *Inorg. Chem.* **1979**, *18*, 924.

123. Duncan, T. M. *Principal Components of Chemical Shift Tensors: A Compilation*; 2nd Ed. The Farragut Press, Chicago, 1994.

124. Kim, A. J.; Butler, L. G. *Inorg. Chem.* **1993**, *32*, 178.

125. Wasylishen, R. E. *Can. J. Chem.* **1982**, *60*, 2194.

126. Herzfeld, J.; Berger, A. E. *J. Chem. Phys.* **1980**, *73*, 6021.

127. Amoureux, J.-P.; Pruski, M.; Lang, D. P.; Fernandez C. *J. Magn. Reson.* **1998**, *131*, 170.

128. Wu, G.; Rovnyak, D.; Huang, P. C.; Griffin, R. G. *Chem. Phys. Lett.* **1997**, *277*, 79.

129. Kofod, P. *J. Magn. Reson. A* **1996**, *119*, 219.

130. Freeman, R.; Murray, G. R.; Richards, R. E. *Proc. R. Soc. London, Ser. A* **1957**, *242*, 455.

131. MacDiarmid, A. G.; Norris, F. H. *J. Am. Chem. Soc.* **1954**, *76*, 4222.

132. Raghavan, P. *Atom. Data Nucl. Data Tab.* **1989**, *42*, 189.

133. Pyykkö, P. *Z. Naturforsch.* **1992**, *47a*, 189.

134. (a) Lucken, E. A. C. *Z. Naturforsch.* **1994**, *49a*, 155. (b) Ramaprabhu, S.; Amstutz, N.; Lucken, E. A. C. *Z. Naturforsch.* **1994**, *49a*, 199.

135. Smith, J. A. S. *J. Chem. Educ.* **1971**, *48*, A77.

136. Diesfeld, J. W.; Menger, E. M.; Edzes, H. T.; Veeman, W. S. *J. Am. Chem. Soc.* **1980**, *102*, 7935.

137. Mohr, B.; Brooks, E. E.; Rath, N.; Deutsch, E. *Inorg. Chem.* **1991**, *30*, 4541.

138. Wu, G.; Wasylishen, R. E. *Inorg. Chem.* **1996**, *35*, 3113.

139. See, for example: (a) Hanna, J. V.; Smith, M. E.; Stuart, S. N.; Healy P. C. *J. Phys Chem.* **1992**, *96*, 7560. (b) Bowmaker, G. A.; Hanna, J. V.; Hart, R. D.; Healy, P. C.; White, A. H. *J. Chem. Soc., Dalton Trans.* **1994**, 2621. (c) Bowmaker, G. A.; Cotton, J. D.; Healy, P. C.; Kildea, J. D.; bin Silong, S.; Skelton, B. W.; White, A. H. *Inorg. Chem.* **1989**, *28*, 1462.

140. VanderHart, D. L.; Gutowsky, H. S.; Farrar, T. C. *J. Am. Chem. Soc.* **1967**, *89*, 5056.

141. Ding, S.; MacDowell, C. A. *J. Chem. Phys.* **1997**, *107*, 7762.

142. Asaro, F.; Camus, A.; Gobetto, R.; Olivieri, A. C.; Pellizer, G. *Solid State NMR* **1997**, *8*, 81.

143. Akrivos, P. D.; Karagiannidis, P. P.; Raptopoulou, C. P.; Terzis, A.; Stoyanov, S. *Inorg. Chem.* **1996**, *35*, 4082.

144. Ainscough, E. W.; Brodie, A. M.; Burrell, A. K.; Hanna, J. V.; Healy, P. C.; Waters, J. M. *Inorg. Chem.* accepted.

145. Bowmaker, G. A.; Cotton, J. D.; Healy, P. C.; Kildea, J. D.; Silong, S. B.; Skelton, B. W.; White, A. H. *Inorg. Chem.* **1989**, *28*, 1462.

146. Baker, L. J.; Bowmaker, G. A.; Hart, R. D.; Harvey, P. J.; Healy, P. C.; White, A. H. *Inorg. Chem.* **1994**, *33*, 3925.

147. Kunwar, A. C.; Turner, G. L.; Oldfield, E. *J. Magn. Reson.* **1986**, *69*, 124.

148. Bowmaker, G. A.; Brockliss, L. D.; Earp, C. D.; Whiting, R. *Aust. J. Chem.* **1973**, *26*, 29.

149. (a) Robert, J. B.; Wiesenfeld, L. *Phys. Rep.* **1982**, *86*, 363. (b) Buckingham, A. D.; Pyykkö, P.; Robert, J. B.; Wiesenfeld, L. *Mol. Phys.* **1982**, *46*, 177.

150. Wasylishen, R. E. *Encyclopedia of Nuclear Magnetic Resonance*; Grant, D. M.; Harris, R. K., Eds; John Wiley & Sons: Chichester, U.K., 1996; pp. 1685-1695.

151. (a) Wu, G.; Wasylishen, R. E.; Pan, H.; Liu, C. W.; Fackler, Jr., J. P.; Shang, M. *Magn. Reson. Chem.* **1995**, *33*, 734. (b) Liu, C. W.; Pan, H.; Fackler, Jr., J. P.; Wu, G.; Wasylishen, R. E.; Shang, M. *J. Chem. Soc., Dalton Trans.* **1995**, 3691.

152. See, for example: Eichele, K.; Wasylishen, R. E.; Kessler, J. M.; Solujić, L.; Nelson, J. H. *Inorg. Chem.* **1996**, *35*, 3904, and references therein.

153. Power, W. P.; Lumsden, M. D.; Wasylishen, R. E. *J. Am. Chem. Soc.* **1991**, *113*, 8257.

154. Penner, G. H.; Wasylishen, R. E. *Can. J. Chem.* **1989**, *67*, 1909.

155. The *reduced coupling constant*, K(N,N'), is useful for comparing signs and magnitudes of couplings between various nuclei, as it incorporates the respective magnetogyric ratios: K(N,N') = $4\pi^2 J$(N,N')/$h\gamma_N\gamma_{N'}$.

156. Jameson, C. J. *Multinuclear NMR*; Mason, J. Ed.; Plenum Press: New York, 1987; pp 89-131.

157. Vega, S. *J. Chem. Phys.* **1974**, *60*, 3884.

158. Hoeft, J.; Nair, K. P. R. *Z. Naturforsch.* **1979**, *34a*, 1290.

159. Hensel, K. D.; Styger, C.; Jäger, W.; Merer, A. J.; Gerry, M. C. L. *J. Chem. Phys.* **1993**, *99*, 3320.

160. (a) Henry, E. R.; Szabo, A. *J. Chem. Phys.* **1985**, *82*, 4753. (b) Nakai, T.; Ashida, J.; Terao, T. *Mol. Phys.* **1989**, *67*, 839. (c) Ishii, Y.; Terao, T.; Hayashi, S. *J. Chem. Phys.* **1997**, *107*, 2760.

161. (a) Penner, G. H.; Power, W. P.; Wasylishen, R. E. *Can. J. Chem.* **1988**, *66*, 1821. (b) Power, W. P.; Lumsden, M. D.; Wasylishen, R. E. *Inorg. Chem.* **1991**, *30*, 2997. (c) Power, W. P.; Wasylishen, R. E. *Inorg. Chem.* **1992**, *31*, 2176. (d) Lumsden, M. D.; Eichele, K. E.; Wasylishen, R. E.; Cameron, T. S.; Britten, J. F. *J. Am. Chem. Soc.* **1994**, *116*, 11129. (e) Wasylishen, R. E.; Wright, K. C.; Eichele, K. E.; Cameron, T. S. *Inorg. Chem.* **1994**, *33*, 407. (f) Lumsden, M. D.; Wasylishen, R. E.; Britten, J. F. *J. Phys. Chem.* **1995**, *99*, 16602.

162. Christendat, D.; Markwell, R. D.; Gilson, D. F. R.; Butler, I. S.; Cotton, J. D. *Inorg. Chem.* **1997**, *36*, 230.

163. Bowmaker, G. A.; Camus, A.; Healy, P. C.; Skelton, B. W.; White, A. H. *Inorg. Chem.* **1989**, *28*, 3883.

164. (a) Woodward, J. *Philos. Trans. Royal Soc. London* **1724**, *33*, 15. (b) Brown, J. *Philos. Trans. Royal Soc. London* **1724**, *33*, 17.

165. Hofmann, K. A.; Küspert, F. A. *Z. Anorg. Allg. Chem.* **1897**, *15*, 204.

166. Iwamoto, T. *J. Incl. Phenom.* **1996**, *24*, 61.

167. (a) Dunbar, K. R.; Heintz, R. A. *Prog. Inorg. Chem.* **1997**, *45*, 283. (b) Vahrenkamp, H.; Geiß, A.; Richardson, G. N. *J. Chem. Soc., Dalton Trans.* **1997**, 3643.

168. (a) Hoskins, B. F.; Robson, R. *J. Am. Chem. Soc.* **1990**, *112*, 1546. (b) Brimah, A. K.; Siebel, E.; Fischer, R. D.; Davies, N. A.; Apperley, D. C.; Harris, R. K. *J. Organomet. Chem.* **1994**, *475*, 85. (c) Janiak, C. *Angew. Chem. Int. Ed. Engl.* **1997**, *36*, 1431.

169. (a) Ferlay, S.; Mallah, T.; Ouahès, R.; Veillet, P.; Verdaguer, M. *Nature*, **1995**, *378*, 701. (b) Mallah, T.; Thiébaut, S.; Verdaguer, M.; Veillet, P. *Science*, **1993**, *262*, 1554.

170. (a) Fehlhammer, W. P.; Fritz, M. *Chem. Rev.* **1993**, *93*, 1243. (b) Clark, J. H.; Duke, C. V. A.; Miller, J. M.; Brown. S. J. *Chem. Commun.* **1986**, 877.

171. (a) Lipshutz, B. H.; Sclafani, J. A.; Takanami, T. *J. Am. Chem. Soc.* **1998**, *120*, 4021. (b) Krause, N.; Gerold, A. *Angew. Chem. Int. Engl. Ed.* **1997**, *36*, 186. (c) Lipshutz, B. H. *Synthesis* **1987**, 325.

172. (a) Yuge, H.; Iwamoto, T. *J. Incl. Phenom.* **1996**, *26*, 119. (b) Brousseau, L. C.; Williams, D.; Kouvetakis, J.; O'Keefe, M. *J. Am. Chem. Soc.* **1997**, *119*, 6292.

173. (a) Khan, N. A.; Mazhar, M.; Baber, N.; Iqbal, M. Z. *J. Mater. Sci. Lett.* **1991**, *10*, 1182. (b) Khan, N. A.; Baber, N.; Iqbal, M. Z.; Mazhar, M. *Chem. Mater.* **1993**, *5*, 1283.

174. see, for example: (a) Mobley, T. A.; Müller, F.; Berger, S. *J. Am. Chem. Soc.* **1998**, *120*, 1333. (b) Bertz, S. H.; Nilsson, K.; Davidsson, O.; Snyder, J. P. *Angew. Chem. Int. Ed.* **1998**, *37*, 314. (c) Bertz, S. H. *J. Am. Chem. Soc.* **1990**, *112*, 4031. (d) Lipshutz, B. H.; Sharma, S.; Ellsworth, E. L. *J. Am. Chem. Soc.* **1990**, *112*, 4032.

175. Cromer, D. T.; Larson, A. C.; Roof, R. B., Jr. *Acta Cryst.* **1965**, *19*, 192.

176. Cromer, D. T.; Larson, A. C.; Roof, R. B., Jr. *Acta Cryst.* **1966**, *20*, 279.

177. Kildea, J. D.; Skelton, B. W.; White, A. H. *Aust J. Chem.* **1985**, *38*, 1329.

178. see for example: (a) Stocker, F. B.; Troester, M. A.; Britton, D. *Inorg. Chem.* **1996**, *35*, 3145. (b) Olmstead, M. M.; Speier, G.; Szabó, *Acta Cryst.* **1993**, *C49*, 370. (c) Stocker, F. B. *Inorg. Chem.* **1991**, *30*, 1472 and references therein.

179. Norberg, B.; Jacobson, B. *Acta Chem. Scand.* **1949**, *3*, 174.

180. Cromer, D. T.; Douglass, R. M.; Staritzky, E. *Anal. Chem.* **1957**, *29*, 316.

181. Bowmaker, G. A.; Kennedy, B. J.; Reid, J. C. *Inorg. Chem.* **1998**, *37*, 3968.

182. (a) Penneman, R. A.; Jones, L. H. *J. Chem. Phys.* **1956**, *24*, 293. (b) Huang, H.; Alvarez, K.; Lui, Q.; Barnhart, T. M.; Snyder, J. P.; Penner-Hahn, J. E. *J. Am. Chem. Soc.* **1996**, *118*, 8808.

183. Stemmler, T. L.; Barnhart, T. M.; Penner-Hahn, J. E.; Tucker, C. E.; Knochel, P. Böhme, M.; Frenking, G. *J. Am. Chem. Soc.* **1995**, *117*, 12489.

184. Dance, I. G.; Dean, P. A. W.; Fisher, K. J. *Inorg. Chem.* **1994**, *33*, 6261.

185. (a) Nishikiori, S.; Ratcliffe, C. I.; Ripmeester, J. A. *Can. J. Chem.* **1990**, *68*, 2270. (b) Nishikiori, S.; Ratcliffe, C. I.; Ripmeester, J. A. *Chem. Commun.* **1991**, 735.

186. (a) Schütze, J.-U.; Eckhardt, R.; Fischer, R. D.; Apperley, D. C.; Davies, N. A.; Harris, R. K. *J. Organomet. Chem.* **1997**, *534*, 187. (b) Davies, N. A.; Harris, R. K.; Olivieri, A. C. *Mol. Phys.* **1996**, *87*, 669. (c) Eller, S.; Schwarz, P.; Brimah, A. K.; Fischer, R. D.; Apperley, D. C.; Davies, N. A.; Harris, R. K. *Organomet.* **1993**, *12*, 3232, and references therein.

187. (a) Eichele, K.; Kroeker, S.; Wu, G.; Wasylishen, R. E. *Solid State NMR* **1995**, *4*, 295. (b) Wu, G.; Wasylishen, R. E. *Magn. Reson. Chem.* **1993**, *31*, 537.

188. Ding, S.; Jones, N. D.; MacDowell, C. A. *Solid State NMR* **1998**, *10*, 205.

189. (a) Wu, J.; Day, J. B.; Franaszczuk, K.; Montez, B.; Oldfield, E.; Wieckowski, A.; Vuissoz, P.-A.; Ansermet, J.-P. *J. Chem. Soc., Faraday Trans.* **1997**, *93*, 1017. (b) Wu, J.; Coretsopoulos, C.; Wieckowski, A. *Electrochem. Soc. Proc.* **1997**, *97-17*, 426.

190. Barber, H. J. *J. Chem. Soc.* **1943**, 79.

191. Sharpe, A. G. *The Chemistry of Cyano Complexes of the Transition Metals*; Academic Press: New York, 1976; pp. 265-285.

192. Bowmaker, G. A. *Advances in Spectroscopy* **1987**, *14*, 1.

193. Gaussian 94, Revision B.2: Frisch, M.J.; Trucks, G.W.; Schlegel, H.B.; Gill, P.M.W.; Johnson, B.G.; Robb, M.A.; Cheeseman, J.R.; Keith, T.; Petersson, G.A.; Montgomery, J.A.; Raghavachari, K.; Al-Laham, M.A.; Zakrewski, V.G.; Ortiz, J.V.; Foresman, J.B.; Cioslowski, J.; Stefanov, B.B.; Nanayakkara, A.; Challacombe, M.; Peng, C.Y.; Ayala, P.Y.; Chen, W.; Wong, M.W.; Andres, J.L.; Replogle, E.S.; Gomperts, R.; Martin, R.L.; Fox, D.J.; Binkley, J.S.; Defrees, D.J.; Baker, J.; Stewart, J.P.; Head-Gordon, M.; Gonzalez, C.; Pople, J.A., Gaussian, Inc., Pittsburgh PA, 1995.

194. (a) Wolinski, K.; Hinton, J. F.; Pulay, P. *J. Am. Chem. Soc.* **1990**, *112*, 8251. (b) Ditchfield, R. *Mol. Phys.* **1974**, *27*, 789.

195. Jameson, A. K.; Jameson, C. J. *Chem. Phys. Lett.* **1987**, *134*, 461.

196. Jameson, C. J.; Jameson, A. K.; Oppusunggu, D.; Wille, S.; Burrell, P. M.; Mason, J. *J. Chem. Phys.* **1981**, *74*, 81.

197. Kroeker, S.; Hanna, J. V.; Wasylishen, R. E.; Ainscough, E. W.; Brodie, A. M. *J. Magn. Reson.* **1998**, *135*, 208.

198. Sardashti, M.; Maciel, G. E. *J. Phys. Chem.* **1988**, *92*, 4620.

199. Ramsey, N. F. *Phys. Rev.* **1950**, *78*, 699.

200. Jameson, C. J. *Encyclopedia of Nuclear Magnetic Resonance*; Grant, D. M.; Harris, R. K. Eds.; John Wiley & Sons: Chichester, U.K., 1996; pp. 1273-1281.

201. (a) Wasylishen, R. E.; Jeffrey, K. R. *J. Chem. Phys.* **1983**, *78*, 1000. (b) Wasylishen, R. E.; Pettitt, B. A.; Jeffrey, K. R. *J. Chem. Phys.* **1981**, *74*, 6022.

202. As the coupling tensors J and R for ^{63}Cu and ^{65}Cu are related by the ratio of their magnetogyric ratios - e.g., $^1J(^{65}Cu,^{13}C)/^1J(^{63}Cu,^{13}C) = 1.071$ - only couplings to

the copper-63 isotope are discussed in the text.

203. Kroeker, S.; Wasylishen, R. E. unpublished.

204. Wasylishen, R. E.; Lenkinski, R. E.; Rodger, C. *Can. J. Chem.* **1982**, *60*, 2113.

205. *Nuclear Magnetic Resonance – A Specialist Periodical Report*; Webb, G. A., Ed.; Royal Society of Chemistry: Cambridge, 1998; Vol. 27 and previous volumes in this series.

206. (a) Kappenstein, C.; Schubert, U. *Chem. Commun.* **1980**, 1116. (b) Peng, S.-M.; Liaw, D.-S. *Inorg. Chim. Acta* **1986**, *113*, L11. (c) Hwang, C.-S.; Power, P. P. *J. Am. Chem. Soc.* **1998**, *120*, 6409.

207. see note 61 in reference 183.

208. Bouslama, L.; Daoudi, A.; Mestdagh, H.; Rolando, C.; Suard, M. *J. Mol. Struct. (Theochem)* **1995**, *330*, 187.

209. Dessy, G.; Fares, V.; Imperatori, P.; Morpurgo, G. O. *J. Chem. Soc. Dalton Trans.* **1985**, 1285.

210. Munakata, M.; Ning, G. L.; Kuroda-Sowa, T.; Maekawa, M.; Suenaga, Y.; Horino, T. *Inorg. Chem.* **1998**, *37*, 5651.

211. Blanchard, S.; Clainche, L. L.; Rager, M.-N.; Chansou, B.; Tuchagues, J.-P.; Duprat, A. F.; Le Mest, Y.; Reinaud, O. *Angew. Chem. Int. Ed.* **1998**, *37*, 2732.

212. Lipshutz, B. H.; Wilhelm, R. S.; Floyd, D. M. *J. Am. Chem. Soc.* **1981**, *103*, 7672.

213. Kronenburg, C. M. P.; Jastrzebski, J. T. B. H.; Spek, A. L.; van Koten, G. *J. Am. Chem. Soc.* **1998**, *120*, 9688.

214. Uchiyama, M.; Kameda, M.; Mishima, O.; Yokoyama, N.; Koike, M.; Kondo, Y.; Sakamoto, T. *J. Am. Chem. Soc.* **1998**, *120*, 4934.